Timing Determination of the ATLAS Pixel Detector Using Offline Data

Masterarbeit

zur Erlangung des akademischen Grades

Master of Science

(M.Sc.)

dem Fachbereich Physik der

Universität Siegen

vorgelegt von

B.Sc. Hendrik Czirr

März 2009

Contents

1 Introduction

The ATLAS (A Large Toroidal LHC Aparatus) detector is part of the largest particle physics experiment ever constructed. It is being commissioned at the LHC (Large Hadron Collider), which is a particle accelerator build underneath the border between Switzerland and France at CERN (Conseil Européen pour la Recherche Nucléaire) near Geneva. Due to a large Helium leak of two sectors of the LHC tunnel the start date of taking physics data has been changed from September 2008 to the second half of 2009. The main purpose of this machine is to investigate the cause for the electroweak symmetry breaking, for which the Higgs mechanism is presumed to be responsible. In addition the consistency of the Standard Model (SM) can be tested at an energy scale of TeV.

The LHC accelerates proton bunches in two beams up to an energy of 7 TeV per beam with a luminosity of 10^{34} cm^{-2} s^{-1}. Once the LHC is fully commissioned, each bunch contains up to 10^{11} protons, counter-circulating in the accelerator ring of 26.7 km circumference [LHC08]. The beams collide in four designated points, where the main detectors are placed. Each interaction of two bunches sets a vast amount of energy free, which is transformed into numerous different particles, according to the law, that energy equals mass times the square of the speed of light. These particles are detected by the four main experiments ATLAS, CMS (Compact Muon Solenoid), ALICE (A Large Ion Collider Experiment) and LHCb (Large Hadron Collider Beauty Experiment). These detectors will collect data, which will provide insight into the core-structure of matter and the forces holding it together.
The beams will interact with a frequency of 40 MHz, once the LHC is fully operational [LHC08]. Because memory capacity is limited and due to the high event rate, only a fraction of the produced data can be stored. The question, if an event contains 'interesting' information, is answered by the trigger system. The trigger system manages the readout of recorded data for a certain event and is structured differently for each of the detectors. In the following, this thesis only refers to the ATLAS trigger system.

It is crucial, that each data set is assigned to the right interaction (bunch crossing). For each of the subdetectors this is achieved by assigning a Bunch Crossing Identifier (BCID) to each hit. Hits can be assigned to the wrong bunch crossing, which would have negative influence on the analysis performed on this data. The wrong assignemt of the BCID is caused by differences in cable lengths between the detector elements, and timewalk effect, which is described in detail in Section 5.1. Different Times of Flight (ToF) also infuence the BCID assignment negatively. ToF differences are caused by the fact, that the distances between the detector surfaces and the interaction point are not equal throughout the detector. Therefore an adjustment of the signal delay has to be performed to ensure, that all signals of one interaction are assigned to the same BCID. The topic of this thesis is to determine the timing of one of ATLAS's subdetectors, the pixel detector, by analysing event data simulated with the Athena Software Framework.

2 Physics at the Large Hadron Collider

The high luminosity and centre of mass energy of $\sqrt{s} = 14$ TeV, of the LHC, offer the chance for the investigation of a wide range of elementary particle physics, including validation of predicted theories (e.g. the Higgs Mechanism, super symmetrical particles, search for extra dimensions), as well as high precision measurements of known properties like the the W-boson- or top-quark mass and gauge couplings. The Standard Model of elementary particle physics (SM) will be described in the following section 2.1 [ATL99b].

2.1 The Standard Model of Elementary Particle Physics

The Standard Model is an extremely successful theoretical construct, that describes the interaction of the elementary particles, of which the world around us is composed [Per90]. The principles can be found in various literature and are only outlined very briefly in this section. The term 'elementary' means that the SM describes these particles as undividable and fundamental at a mass scale of up to 200 GeV. As quantum mechanical field theory, the SM defines pointlike fermions of spin 1/2, interacting by three fundamental forces, which are mediated by gauge bosons of spin 1. The fermions can be divided into two groups arranged in three generations, leptons, carrying an electrical charge of 0 or -e, and quarks with a charge of $-1/3$ e or $+2/3$ e. Stable matter is composed of particles from the first generation, the second and third generation particles decay after numerous intermediate steps into first generation types. The masses of the different fermions are listed in Tables 2.1 and 2.2.

Fermions	First Gen.	Second Gen.	Third Gen.	Charge in e
Leptons	electron $m_e = 0.511$ MeV	muon $m_\mu = 105.7$ MeV	tau $m_\tau = 1777.3$ MeV (upper limit)	-1
	ν_e $m_{\nu_e} < 2$ eV	ν_μ $m_{\nu_\mu} < 2$ eV	ν_τ $m_{\nu_\tau} < 2$ eV	± 0

Table 2.1: The convention $\hbar = c = 1$ is used [WY06].

Each lepton generation comprises a massive charged particle (e, μ, τ) and a massless neutrino with charge 0 ($\nu_{e,\,\mu,\,\tau}$), forming a mathematical doublet. To every doublet an antimatter counterpart with opposite charge, but same mass and spin, exists. Unlike leptons, quarks have not been observed in unbound states. Quarks form hadrons, which are divided in baryons, consisting of three quarks, and mesons, composed of two quarks.

Fermions	First Gen.	Second Gen.	Third Gen.	Charge in e
Quarks	up $m_u = 1.5 - 3.3$ MeV	charm $m_c = 1.27^{+0.07}_{-0.11}$ GeV	top $m_t = 171.2 \pm 2.1$ GeV direct observation	$+\frac{2}{3}$
	down $m_d = 3.5 - 6.0$ MeV	strange $m_s = 104^{+26}_{-34}$ MeV	bottom $m_b = 4.20^{+0.17}_{-0.07}$ GeV	$-\frac{1}{3}$

Table 2.2: u-, d- and s-quark masses are current quark masses in the $\overline{MS}$-scheme; b- and c-quark masses are running masses in the $\overline{MS}$-scheme, the convention $\hbar = c = 1$ is used [CA08].

The forces between the elementary particles are mediated by different gauge bosons.

- *Electromagnetic Force*: The electromagnetic (EM) interaction is described by quantum electrodynamics (QED). The mediating gauge boson is the massless photon (γ), which couples to the electric charge.

- *Strong Force*: The strong force is described by quantum chromodynamics (QCD), its gauge bosons are the eight massless, spin 1 carrying, gluons (g). The gluons couple to the colour (quark) or anticolour (antiquark) charge of an elementary particle. The gluons themselves also carry a pair of colour/anticolour charges and can interact with each other. The sum of all colour charges in a hadronic particle has to be neutral. The strong interaction is formulated using the mathematical SU(3) gauge group.

- *Weak Force*: This interaction is described by three mediating massive gauge bosons, $W^{\pm}$ ($m_{W^{\pm}} = 80.403$ GeV), and Z^0 ($m_{Z^0} = 91.19$ GeV), which can couple to any elementary particle. In comparison to the electromagnetic interaction the weak force is 10^5 times weaker and can only be measured if strong or EM interactions are suppressed or forbidden (such as flavour-changing interactions)[WY06].

The gravitational force can be neglected on the scale of elementary particle physics and is not included in the SM. Theoretical expansions describing the gravitational force feature e.g. a massless spin 2 graviton as a gauge boson. These theories have not been experimentally proven. The electromagnetic and the weak interactions have been unified by Glashow, Salam and Weinberg (1967/68) to the electroweak interaction [Per90].

2.2 Higgs Boson Search

Though the SM describes particle physics at the experimentally reachable scales very well, the mass differences of the three lepton and quark generations are not explained in the unextended SM. By adding a scalar field, the theory leads to the massless γ, the massive $W^{\pm}$, Z^0 and the massive scalar Higgs boson [H66]. One purpose of the ATLAS (and the CMS) experiment is to find this boson. Its coupling is directly proportional to the fermion

masses and to the squared boson masses ($W^{\pm}$, Z^0). Perturbative calculations (constrained to finite and positive Higgs couplings) lead to an upper limit for the Higgs mass, which is about 1.2 TeV [Per90]. The existing lower mass limit of 114 GeV was provided by measurements at LEP2 [CC08]. Due to the coupling to the mass, the Higgs boson decays preferably to the heaviest particle that is kinematically allowed. The LHC will offer excellent conditions to discover the Higgs boson, if it exists.
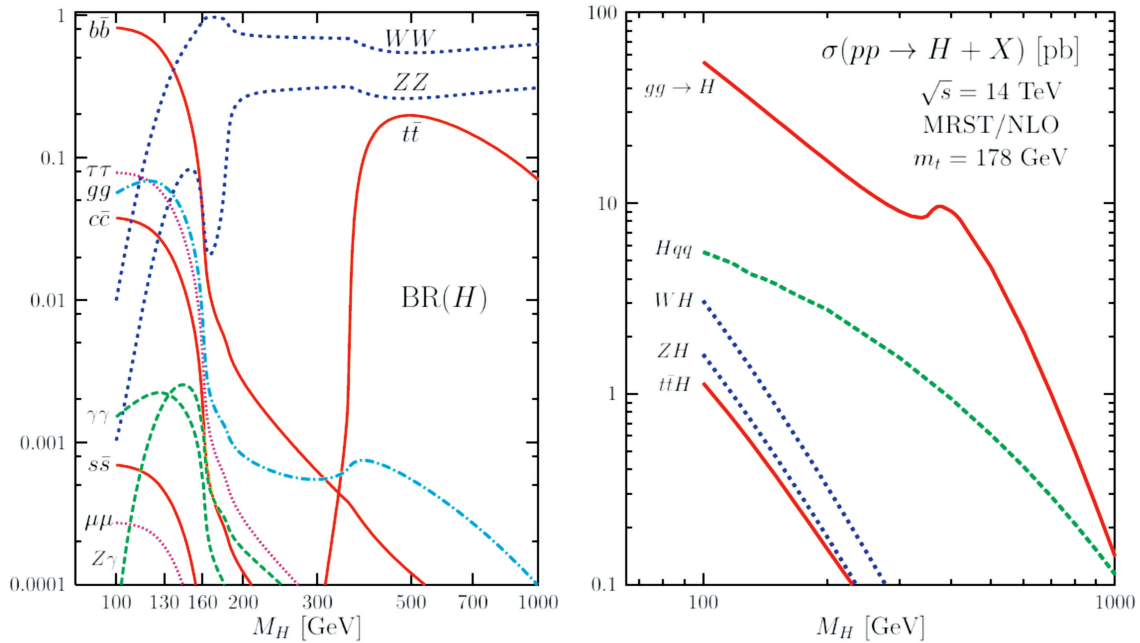
Figure 2.1: Decay branching ratios of the SM Higgs boson and it's production cross sections in the main channels at the LHC [Dj05].
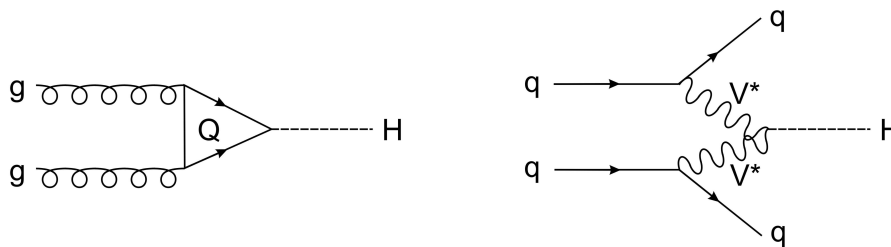
Figure 2.2: LHC Main production channels for the Higgs boson, gluon-gluon fusion (left) and vector boson fusion (right).

The main production processes considered are the guon-gluon fusion mode ($gg \rightarrow H$) via a top quark loop and the vector boson fusion (see Figure 2.1 channel H_{qq}) [CC08].
A detector, constructed for the Higgs boson search, has to be able to identify a large variety of physical signatures, because the mass of the Higgs boson and hence its decay channels are not exactly known. Consequently, the ATLAS detector features different subdetectors, which as a whole form not only a tool to find the Higgs boson, but also, a powerful general purpose detector. The ATLAS detector is described in detail in Chapter 4.

2.3 B-Physics and New Physics

The high B-meson production rate at the LHC is caused by the large hadronic cross section for b-quark production and allows the investigation of a wide range of physics. Approximately one in a hundred collisions will produce a b-quark pair. One task of the B-physics studies is to test the SM with high precision measurements. The B-physics programme will contain, but is not limited to:

- Studies on CP-Violation in B-meson decays, by precise measurements of the phase of the Cabbibo-Kobayashi-Maskawa matrix (CKM matrix),

- Measurements of flavour oscillation periods in B_s^0 and B_d^0 mesons,

- Determination of relative decay rates,

- Studies of very rare decays (e.g. of type $B_{d,s}^0 \to \mu\mu\,(X)$), which may provide indirect evidence for new physics.

The investigation of New Physics means the search for particles predicted in a large variety of SM-extending theories, like Supersymmetry (SUSY), string theory, or Grand Unification Theory (GUT). Furthermore studies of an inner fermion structure and new gauge bosons with masses greater than 100 GeV are possible [ATL99b].

2.4 Detection Principles

Particles traversing matter are detected if an interaction of the primary or secondary particles generated in the interaction, takes place, leaving a 'readable' signature. There are different interactions causing energy loss of a particle passing through matter. Charged particles undergo ionisation-, excitation- and, at relativistic scales, also bremsstrahlung-, pair-production- and photonuclear processes. Neutral massive particles are detected by their production of secondary charged particles in the sensitive detector volume, leaving characteristic interaction signatures. Photons interact via different effects: Pair production of electrons, Compton scattering and the photoelectric effect [WY06].

2.4.1 Energy Loss of Heavy Particles

The energy loss of heavy particles in matter is primarily caused by ionisation and atomic excitation. The average energy loss per length is given by the Bethe-Bloch equation, which does not include bremsstrahlung effects:

$$-\frac{dE}{dx} = 4\pi N_A r_e^2 m_e c^2 z^2 \frac{Z}{A} \frac{1}{\beta^2} \left(\ln \frac{2m_e c^2 \gamma^2 \beta^2}{I} - \beta - \frac{\delta}{2} \right), \qquad (2.1)$$

with:

z - charge of the traversing particle in multiples of the elementary charge,

$Z,\ A$ - atomic number and atomic mass of the absorber,

m_e - electron mass energy equivalent, 511 keV,

r_e - classical electron radius, 2.818 fm,

N_a - Avogadro number, 6.022×10^{23} mol^{-1},

I - mean exitation energy,

δ - density effect correction to ionisation energy loss.

Figure 2.3 illustrates the average energy loss dE/dx of a muon in different materials corresponding to the Bethe-Bloch equation 2.1. Radiative effects are not included. The length unit dx in units of g / cm^2 is used because of its nearly independence from material properties. The energy loss decreases with $1/\beta^2$ at low energy ranges, followed by a broad minimum around $\beta\gamma \approx 4$. Particles with an energy in this region is called Minimum Ionising Particles (MIP). For silicon at standard temperature and pressure (300 K, 1 bar) the MIP energy loss is $-\frac{dE}{dx} = 1.66\ \frac{\text{MeV}}{\text{g/cm}^2}$.
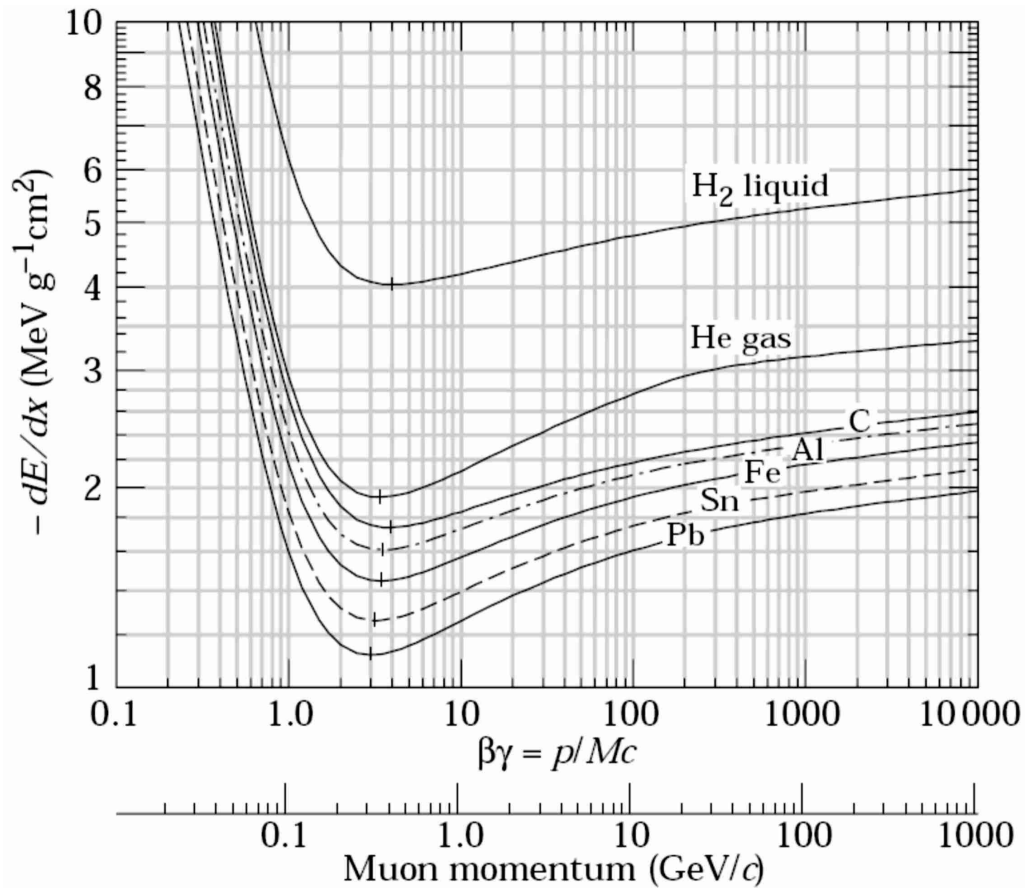
Figure 2.3: Mean energy loss rate in different materials, radiative effects for muons are not included [WY06].

For energies above the minimum energy loss, dE/dx increases logarithmically. The dependence can be approximated by $2 \ln\gamma$. At high energies, the energy loss saturates due to the density effect. Materials, which are thin in terms of dx, show strong fluctuations along the average energy loss, because in primary ionisation electrons of high energies are likely to be generated. These electrons also ionise the material, so low energy transfers at small energies are more probable. The overall distribution for thin materials can be parameterised by a Landau distribution [CG93]:

$$L\left(\lambda\right) = \frac{1}{\sqrt{2\pi}} \cdot \exp\left[-\frac{1}{2}\left(\lambda + \mathrm{e}^{-\lambda}\right)\right], \tag{2.2}$$

with λ as the deviation from the most probable energy loss.
For thick absorbers with $\frac{dE}{dx} \cdot x \;>>\; 2\mathrm{m}_e\mathrm{c}^2\beta^2\gamma^2$, the energy loss can be approximated by a Gaussian distribution [CG93].

2.4.2 Bremsstrahlung, Direct Electron-Pair Production

Highly energetic charged particles also lose energy due to bremsstrahlung. Bremsstrahlung effects take place, when a charged particle is deflected by the electric field of a nucleus and emits a fraction of its kinetic energy as photons. In contradiction to the ionisation energy loss, the energy diminishes proportionally to the energy of the incident particle [WY06]. Another mechanism for energy loss at very high energies is the electron-pair production, by virtual photons, in the Coulomb field of a nucleus. For high energy muons this process is even more important than bremsstrahlung effects. Besides the already described effects, there is also the energy loss due to photonuclear interactions. This is the inelastic scattering of a charged particle via a virtual gauge particle with a nucleus of the traversed material [CG93].

2.4.3 Photon Interactions

Photons can only be detected indirectly in an absorption process, like the photoelectric effect, electron-pair production, or in scattering due to the Compton effect. Photon beam attenuation in matter can be described as:

$$I\left(x\right) = I_0 e^{-\mu x}, \tag{2.3}$$

with μ as the mass attenuation coefficient, which strongly depends on the photon energy and I_0 as the initial intensity. The photon interactions are:

- *Photoelectric Effect*: Photon absorption of an atomic electron, whereas momentum conservation is provided by the presence of a nucleus as third collision member,

- *Pair-Production*: Production of an electron / positron pair in the elctric field of an atomic nucleus. This only happens at sufficiently high energies,

- *Compton Effect*: Scattering of a photon on quasi-free atomic electrons.

2.4.4 Silicon Based Semiconductor Detectors

Semiconductor detectors provide high precision track measurements. They are widely used in high energy particle physics, combining fast readout speed and high spatial resolution. These parameters depend mostly on the segmentation of the sensor layout. For the parameters of the ATLAS Pixel-Detector see Section 4.4.1.
Because of its high density of $\rho = 2.33$ g/cm^3 and low ionisation energy of 3.62 eV (at 300 K), silicon is a good base material for semiconductor detectors [CG93]. The high density provides the possibility to produce very thin sensors, having only a small effect on the particles energy, but allowing the detection of particles in a wide energy range.
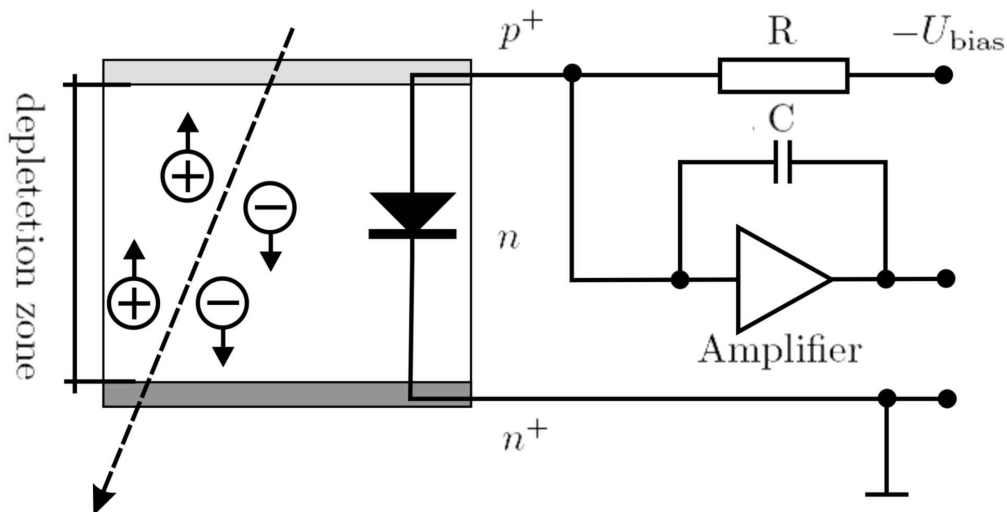
Figure 2.4: Principle of a semiconductor detector with n-type bulk, p$^+$ domain is supplied with negative potential [Gr93].

The basic principle of a semiconductor detector is, that a charged particle traversing a semiconducting material generates electron-hole pairs due to the ionisation effect (Section 2.4.1). Its task is to prevent these electron-hole pairs from recombination and convert these charges into a measurable pulse. In a 250 μm thick silicon layer a MIP deposits a most probably energy of 71 keV, corresponding to roughly 80 electron-hole pairs per μm [Mo99].

In principle a semiconductor detector is a reversly biased diode, which is characterised by a semiconductive material (silicon in our case) with a sharp transition between a positively- (p) and a negatively- (n) doped domain. Doping means, that impurities are brought into the material, providing free charge carriers: Holes (p) for a trivalent- and electrons (n) for a pentavalent- impurity. Between these domains charge carriers recombine until the electrical field, which is caused by the shift of the charges, balances the diffusion current. Consequently, a depletion layer without free charge carriers is generated. This process is

supported by applying a negative voltage to the p-doped domain (reversly biased mode). The extension of the depletion layer enlarges the volume available for particle detection and improves the signal to noise ratio. In pure silicon the thermal noise would be at signal level [CG93].

3 Introducing the LHC

3.1 The Large Hadron Collider

The Large Hadron Collider (LHC) is a circular particle accelerator. It is built at CERN, the european laboratory for particle physics, inside the tunnel of the LEP (Large Electron Positron collider) accelerator, which was operational from 1989 until 2000 (1989-1995 LEP1 and 1996-2000 LEP2) [LEP08]. The underground structures of the LHC are presented in Figure 3.1. The locations of the detectors are shown in Figure 3.2.
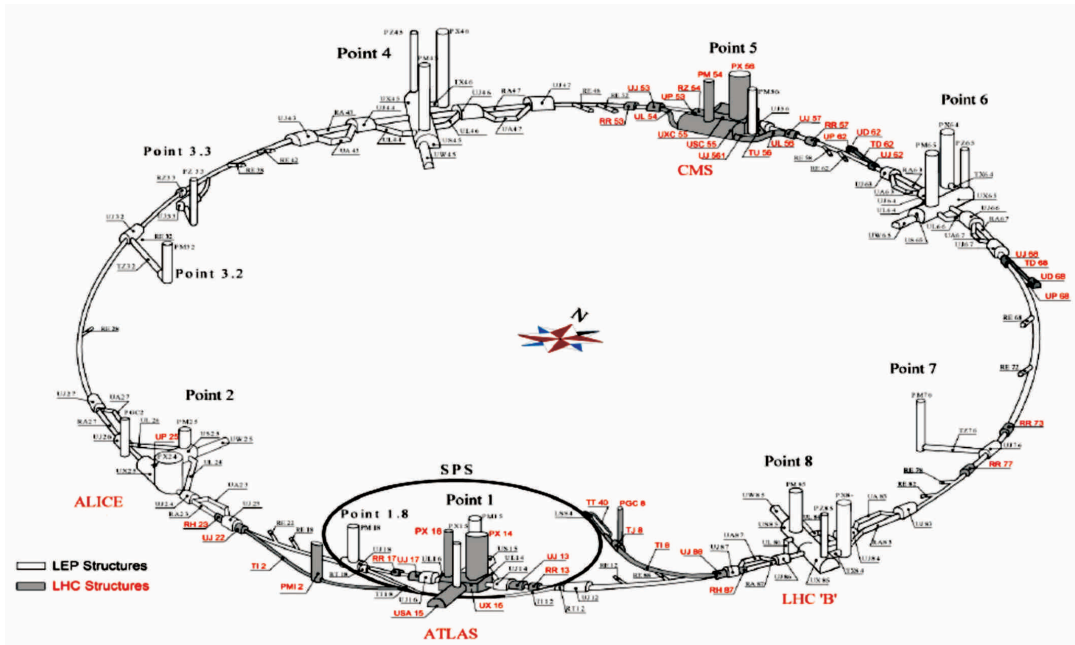
Figure 3.1: Structures of the LHC [LHC08]

In a depth of 50 m to 175 m underneath the Jura on the border between Switzerland and France lies the LHC with a circumference of 26.7 km. In this accelerator two counter directed beams are accelerated to a centre of mass energy of up to 14 TeV at a maximum luminosity of 10^{34} cm^{2}s^{-1}. The total cross section for proton-proton collisions is 100 mb. In four interaction points these beams collide every 25 ns. In each point one of the four main detectors is located. ATLAS and CMS are general purpose detectors, LHCb is mainly for B-physics and ALICE probes for the particles produced in heavy ion (lead) collisions taking place in the future of LHC. ATLAS is mainly designed to serve as a detector for proton-proton collisions. The design parameters for heavy ions are not described in this thesis.

The beams are composed of bunches filled with up to $1.15 \cdot 10^{11}$ protons, which are accelerated in parallel running beam pipes with a common magnetic field. The field intensity goes up to 8 T and can only be reached with superconducting (Helium cooled) magnets [ATL99a].

Before the proton bunches are fed into the main ring of the LHC they run through an accelerator chain: Linac (Linear accelerator), Proton Synchroton Booster (PSB), Proton Synchrotron (PS) and the Super Proton Synchrotron (SPS) increasing the beam energy in each step:
Linac 50 MeV $\rightarrow$ PSB 1.4 GeV $\rightarrow$ PS 25 GeV $\rightarrow$ SPS 450 GeV. The LHC accelerates the protons to their final energy of 7 TeV per beam [LHC04]. Once providing the injection chain for LEP, these accelerators were upgraded to serve their new purpose, to inject a large number of high intensity protons with defined longitudinal and small transversal emittance.

3.2 Main Detectors at the LHC

To detect the products of the collisions four different main detectors are integrated into the structure of the LHC. The ATLAS Detector will be described in Chapter 4.

ALICE is primarily designed to investigate heavy ion collisions which provide the opportunity to study the transition of hadronic matter, where quarks and gluons are confined, into a plasma of (almost) free quarks and gluons. The unrivalled energy scale of the LHC will give the chance to explore the physics of strongly interacting matter under extreme temperature and density [AL04].

One of the main motivations to build the LHC is the discovery of the Higgs Boson, which is also a purpose of CMS. Besides that, extra dimensions, Quantum Chromo Dynamics and flavour physics are under investigation. The name Compact Muon Solenoid hints at the relatively small size (21 m in length and 16 m in diameter), the strong solenoid magnet which provides a field of 4 T and the good muon identification over a wide range of momenta. Detector requirements are e.g. good dimuon mass (approximately 1% at 100 GeV/c^2) and charged particle momentum resolution [CMS06].

LHCb is designed to study CP-Violation and other phenomena concerning B-Meson decays. These high precision measurements will give the opportunity to gain a deeper understanding of quark flavour physics and Physics beyond the SM. To achieve this goal, the detector features a high track reconstruction efficiency, a very good time resolution ($\approx$ 40 fs), and high trigger efficiencies for leptonic and hadronic final states [LHCb03].

3.3 LHCf and TOTEM

In addition to the main detectors there are two more. There is LHCf (Large Hadron Collider forward Experiment) and TOTEM (Total Elastic and Diffractive Cross-Section Measurement). LHCf investigates the energy distribution of particles emitted in the very forward region, which is important for the understanding of cosmic ray phenomena. LHCf shares point 1 with ATLAS. The TOTEM detector will measure the total proton-proton cross-section, study elastic scattering and defractive dissociation at the LHC. The detector is installed in the CMS forward region [LHCf06, TOT07].
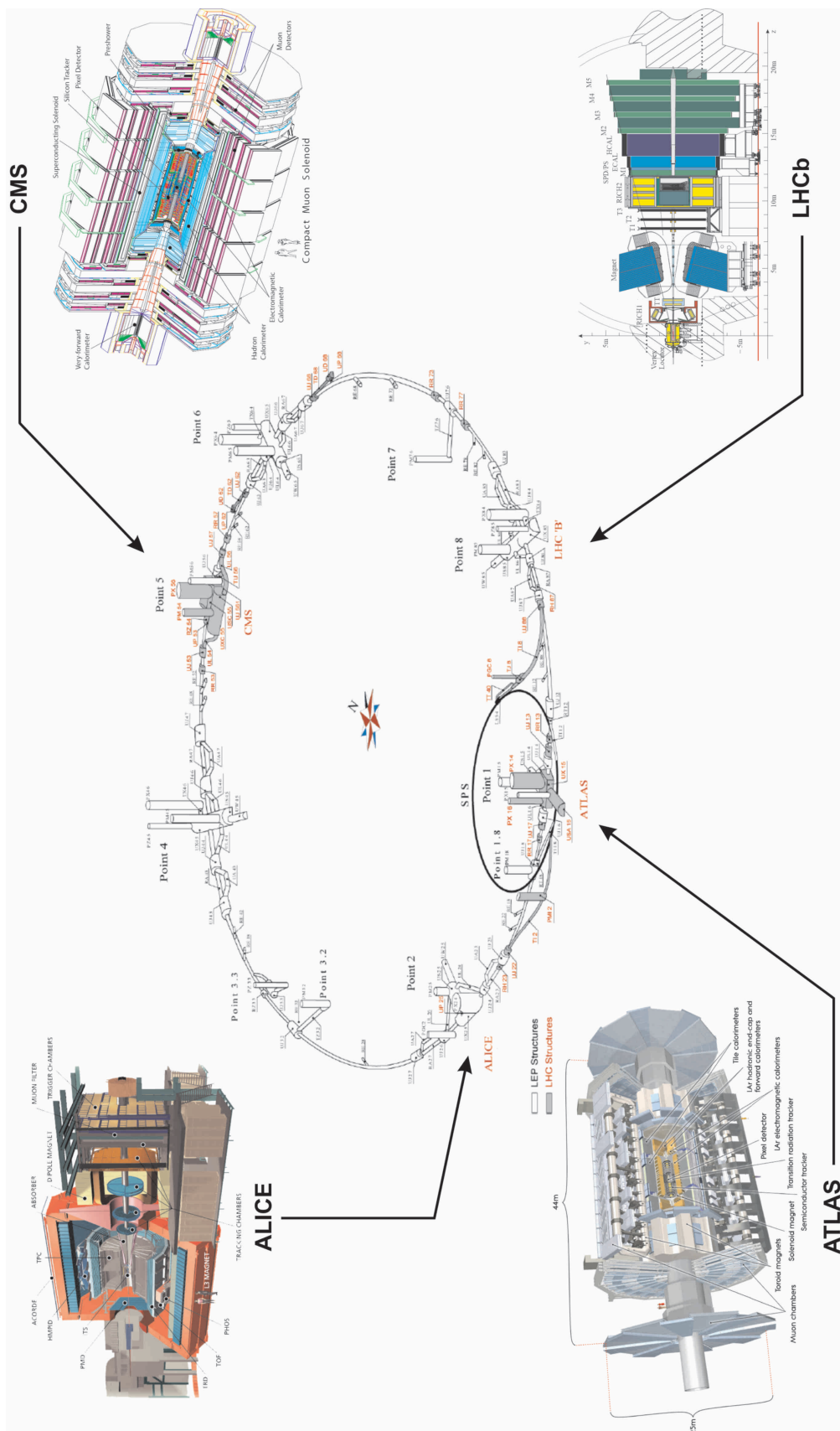
Figure 3.2: Positions of the four main detectors along the LHC [LHC08, ATL99a, CMS06, AL04, LHCb04].

4 The ATLAS Detector

The ATLAS detector is positioned in a cavern at injection point one of the LHC (Figure 3.2). This detector allows to probe for an extensive range of physics, not only in proton-proton, but also in heavy ion collisions.
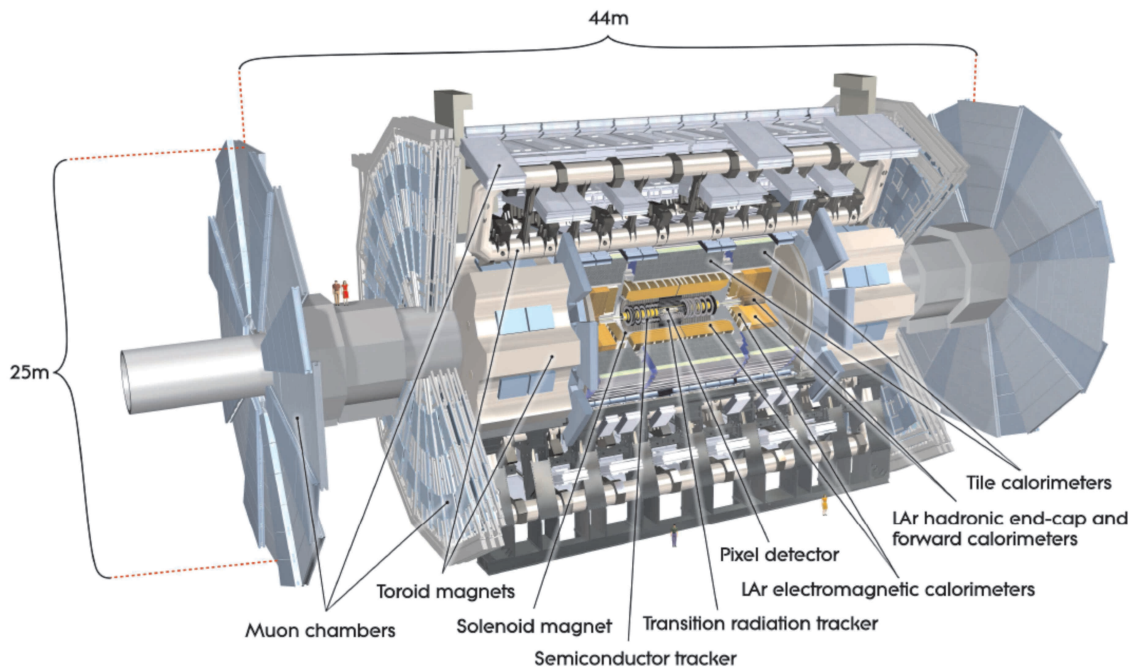
Figure 4.1: Cut-away view of the ATLAS detector [ATLj08].

As Figure 4.1 shows, the ATLAS detector measures 44 m in length and 25 m in diameter, without support structures. Its weight of approximately 7 000 t is only exceeded by the weight of 12 500 t of the CMS-Detector. The ATLAS detector is designed to work in the environment of the LHC. Such as the event rate of 40 MHz and the high particle energies, causing an extensive level of radiation. The detector is built symmetrically around the LHC beam line with the particle interaction point in its centre. So an almost complete solid-angle coverage for the detection of collisions remains is guaranteed.

The coordinate system used to describe the ATLAS detector and its subdetectors, has its origin in the interaction point. The beam direction defines the z-axis. The detector half pointing west in positive z-direction is referred to as side A, the half pointing east in negative z-direction is referred to as side C. The x-axis points to the centre of the LHC ring, which leaves the y-axis of the right-handed system pointing upwards from interaction point. The azimuthal angle ϕ is measured around the beam axis and the polar angle

Θ is perpendicular to the ϕ-plane. The Θ coordinate is not Lorentz invariant, thus the pseudorapidity is used for the polar angle. The pseudorapidity is defined as [ATLj08]:

$$\eta = -\ln\left(\tan\frac{\Theta}{2}\right). \tag{4.1}$$

In the following Sections the individual parts of the detector are described.

4.1 The Muon System

The muon system represents one of the key elements of the ATLAS detector. The muon system provides the outermost and one of the inner detection layers of ATLAS. Aside from muons, there are no detectable particles originating from collision events, that can pass through all the inner layers of ATLAS. Consequently the muons can be used as detection signatures for physical processes.

There are two main functions of the muon detector system. High precision, three dimensional, track measurement of muons, and the supply of Level 1 Trigger information (described in Chapter 4.5). The track measurements in the muon system provide increased precision in the total energy reconstruction. This enhances the accuracy of the missing energy determination of an event.
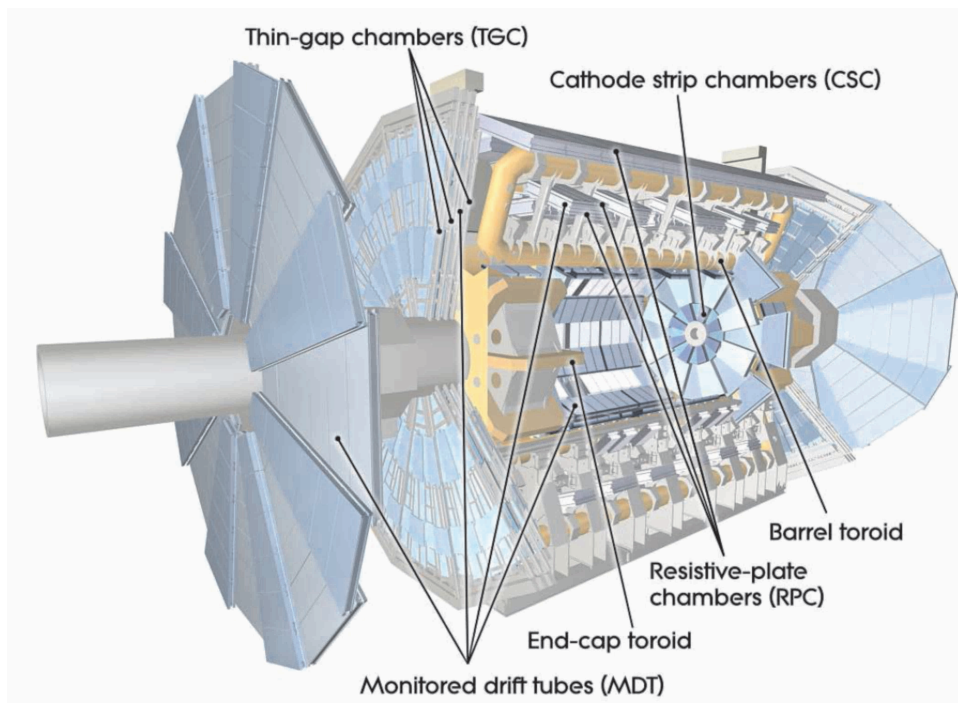
Figure 4.2: Cut-away view of the ATLAS muon sytem [ATLj08].

The magnetic field is provided by air-core toroid magnets (Barrel toroid Figure 4.2). In the range of $|\eta| < 1.4$ the Barrel toroid provides the magnetic field. In the region of $1.6 < |\eta| < 2.7$ this is achieved by two smaller magnets, the end-cap toroids. The space between these η-areas, which is referred to as transition region, is covered by a combination of end-cap and barrel fields [ATLj08].
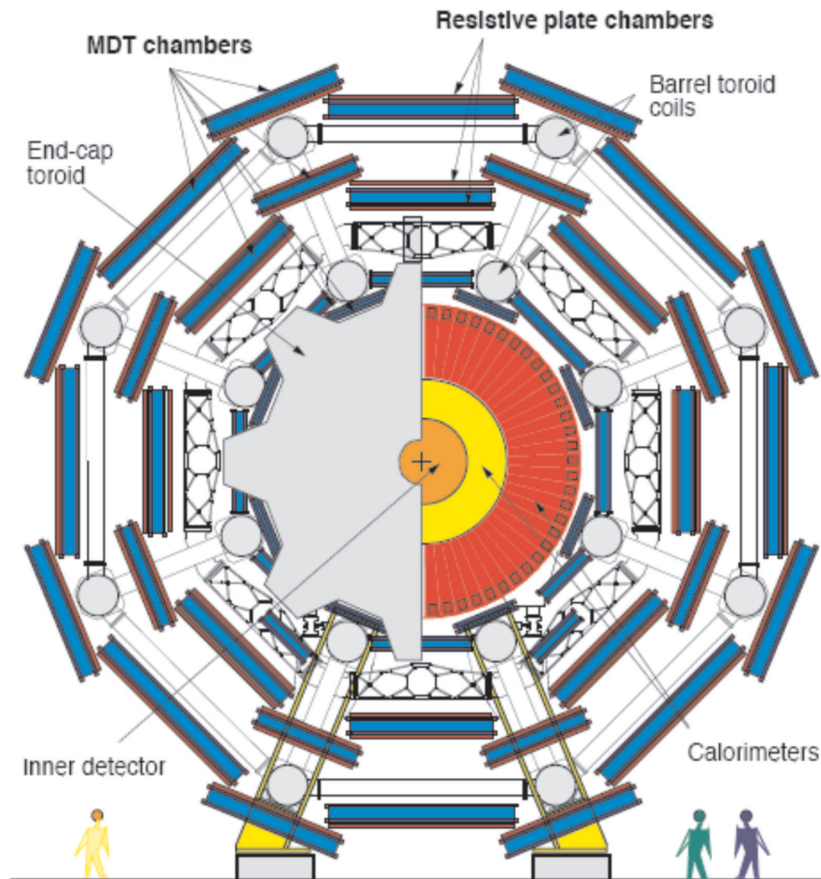
Figure 4.3: Schematic view of the ATLAS muon system in positive z-direction [JW08].

The Barrel part of the ATLAS muon system consists of three layers built symmetrically around the beam axis (radii of 5.0 m, 7.5 m and 10.0 m) and covers a region of $|\eta| < 1.0$ in pseudorapidity. The schematic view can be seen in Figure 4.3.

In the end-cap region four discs, at a distance of 7 m, 10 m, 14 m and 21-23 m from the centre of ATLAS, are installed. These discs cover a pseudorapidity of $1.0 < |\eta| < 2.7$ [ATL99a]. Due to the high level of radiation and the twofold purpose of the muon system, we find different types of subdetectors in the muon system. The radiation is composed mostly of neutrons and photons in the 1 MeV range, which originate from secondary interactions with the detector or beam pipe material.

The different subdetectors are, the Monitored Drift Tubes (MDT) and the Cathode Strip Chambers (CSC) for exact track recording and the Resistive Plate Chambers (RPC) and Thin Gap Chambers (TGC), which provide the Level 1 Trigger signal and secondary co-

ordinates for particle tracking. Both the MDT and the CSC are composed of single wire drift tubes. The name Monitored Drift Tubes hints at the fact, that the MDTs, as well as the CSCs, are controlled by an optical alignment system, to ensure the accuracy of the chamber positioning, which is directly connected to the tracking precision. The RPCs are narrow gaseous detectors and the TGCs are multi-wire proportional chambers, they provide fast trigger information in the barrel and the end-cap regions. The detailed coverage of the subdetectors is [JW08]:

MDT	:	$|\eta| < 2.7$, innermost layer $|\eta| < 2.0$,
CSC	:	$2.0 < |\eta| < 2.7$,
RPC	:	$|\eta| < 1.05$,
TGC	:	$1.05 < |\eta| < 2.7$, respectively 2.4 for Trigger.

The MDTs surround the interaction point in an inner and an outer Barrel-layer, as well as perpendicular to the beam line. The disc shaped chamber system covers the whole diameter of ATLAS and defines the overall shape of the whole detector. In the forward region of the innermost muon system shell there are CSCs with high granularity, that can withstand the high radiation level at these large pseudorapidities. Both the MDTs and the CSCs are installed in an octagon, like the toroid magnets. The trigger system is built by the RPCs in the Barrel and the TGCs in the end-cap region. The main requirement is a fast response, to provide a bunch crossing identification with a time resolution better than 25 ns. A second coordinate measurement, almost parallel to the magnetic field of the Barrel toroid, is provided additionally [ATLMu07].

4.2 The Calorimeter System

The calorimeter system measures the energies of traversing particles. A cut-away view of all its components is shown in Figure 4.4. All ATLAS calorimeters feature sampling technology, which means, that passive absorber and active detector materials alternate [ATL99a].

There are two kinds of calorimeters: The electromagnetic (EM) calorimeter, that determines the energy loss of a particle, subject to electromagnetic interactions. And the hadronic calorimeter, serving the same purpose for particles, that are mainly subject to strong interactions.
The measurement principle is the same in both types of detectors. A primary particle enters the passive absorber and produces cascades of secondary particles, which are detected in the active material. From the depth of the shower the energy of the primary particle and a coarse position information can be derived [CG93].
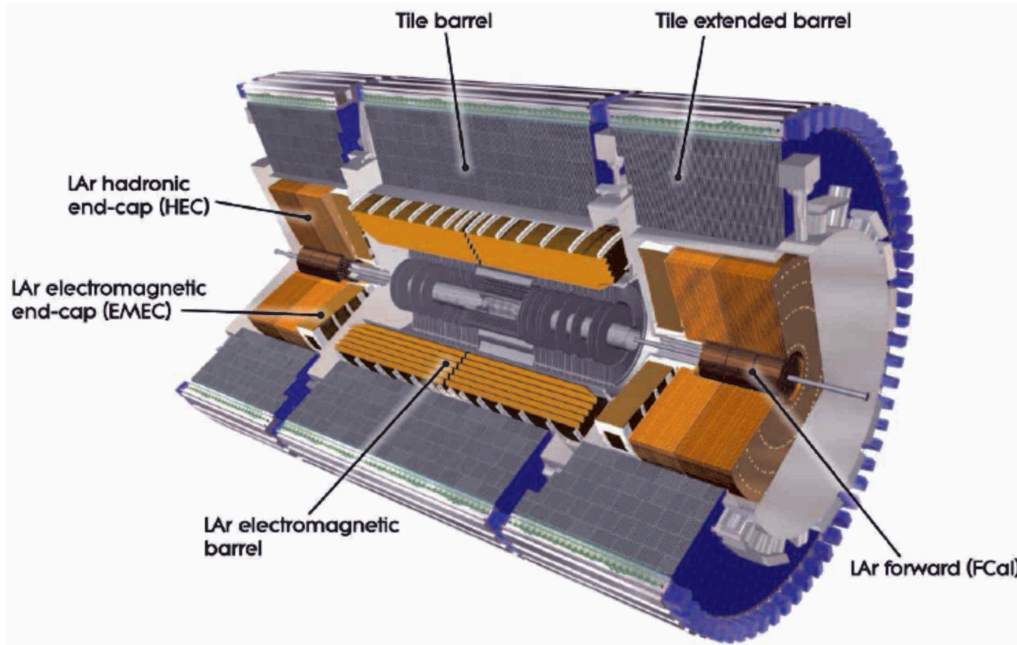
Figure 4.4: Cut-away view of the ATLAS calorimeter sytem [ATLj08].

4.2.1 The Electromagnetic Calorimeter

The EM calorimeter (EMCal) system of ATLAS consists of three sections.
The first section is the EM barrel calorimeter, which is located around the Inner Detector and offers full ϕ acceptance. In the EM barrel calorimeter, lead is used as passive and liquid Argon (LAr) as active material. The second section contains the two end-cap calorimeters (EMEC), featuring the same detector materials as the EM barrel. The third section is comprised of the EM subdetector of the forward calorimeter (FCal), which utilises a copper-LAr sampling technology.

The barrel calorimeter comprises two identical half-shells, separated by a 4 mm wide gap at $z = 0$. The overall structure of accordion-shaped lead absorbers and polyamide electrodes supplies an η-coverage of $0 < |\eta| < 4.9$ and avoids the creation of insensitive detector areas.
The granularities ($\Delta\eta \times \Delta\phi$) vary over the η-range from about 0.025×0.025, in the first layer of the barrel, to 0.1×0.1 in the first end-cap layer [ATLj08]. The part with the highest granularity is the middle section, where the widest spread of particle showers is expected. With higher pseudorapidities, the showers tend to have a smaller spread.
Expressed in multiples of the radiation length X_0, the thickness of the barrel is $> 22\,X_0$ and the thickness of the EMECs is $> 24\,X_0$, which is adequate to minimize the punch-through below the background of prompt and decay muons. This provides a good measurement of the missing transverse energy E_T^{miss}. Without the presamplers, the EMCal features approximately 168 000 readout channels. The presampler is a finer segmented calorimeter, which is used to record the spread of multiple scattering particle showers [ATLj08].

4.2.2 The Hadronic Calorimeter

The Hadronic calorimeter (HCal) features different material combinations. In the tile calorimeter (in Figure 4.4 referred to as Tile Barrel) there are 14 mm thick steel absorbers alternating with 3 mm thick plastic scintillator tiles, used as active components. Two sides of the scintillating tiles are read out using wavelength-shifting fibres, which feed their signals into two separated photomultiplier tubes (PMT).

The hadronic barrel calorimeter consists of three cylinder-symmetrical shells placed in the same layer around the inner EM barrel, two extended and one centred shell. The dimensions of the centred shell are: 5.8 m in length, with an inner radius of 2.28 m and an outer radius of 4.25 m.

The extended shells have the same radii and are each 2.6 m long. The region of $|\eta| < 1.0$ is covered by the inner Tile Barrel and $0.8 < |\eta| < 1.7$ by the two extended Tile Barrels. The gap region between the centre and the extended shells is equipped with modules of steel-scintillator sandwiches, which partially recover the energy, which would otherwise be lost in the detector crack regions. The overall positioning between the muon system and the EMCal reduces the punch-through of hadronic particles to an acceptable rate.

The Hadronic Endcap calorimeter (HEC) is located between the EMEC and the outer muon system discs. Each HEC consists of two segmented wheels per end-cap and shares one cryostat with the EMEC and the forward calorimeter. To avoid big differences in material densities, the HEC's η coverage overlaps with the forward calorimeter and the extended tile calorimeter ($1.5 < |\eta| < 3.2$).

Each of the four wheels consists of 32 wedge shaped modules structured in two layers per wheel, perpendicular to the beam axis. The calorimeter layers utilise copper as passive material, in layers of a thickness of 25 mm, facing the interaction point (24 copper plates plus one 12.5 mm face plate), rather 50 mm in direction of the forward calorimeter (16 copper plates plus face plate). All copper layers alternate with 8.5 mm thick LAr active layers.

The readout cells have a size of $\Delta\eta \times \Delta\phi = 0.1 \times 0.1$ in $|\eta| < 2.5$ and $\Delta\eta \times \Delta\phi = 0.2 \times 0.2$ for $|\eta| \geq 2.5$. In total the hadronic calorimeter features about 10 000 readout channels [ATLj08].

4.2.3 The Forward Calorimeter

The FCal consists of two high density hadronic calorimeters (see the schematic view in Figure 4.5) and the EM calorimeter, which is the FCal part located closest to the interaction point. It covers a region of $3.1 < |\eta| < 4.9$. It is positioned in the same cryostat as the end-cap calorimeters. This results in a hermetic design, that minimises energy losses between the calorimeter structures. To reduce the neutron albedo in the inner detector region, the FCal's position is recessed for about 1.2 m with respect to the EMCal (at a distance of about 4.7 m from the interaction point).

The reduced dimensions, and the requirement, that the background for the muon system has to be minimised, demand the high density design. The EMcal features a copper-LAr (27.6 X_0) sampling technology. The first (91.3 X_0) and second (89.2 X_0) hadronic calorimeter utilise on the contrary a tungsten-LAr sampling technology, with an overall thickness of ten interaction lengths.
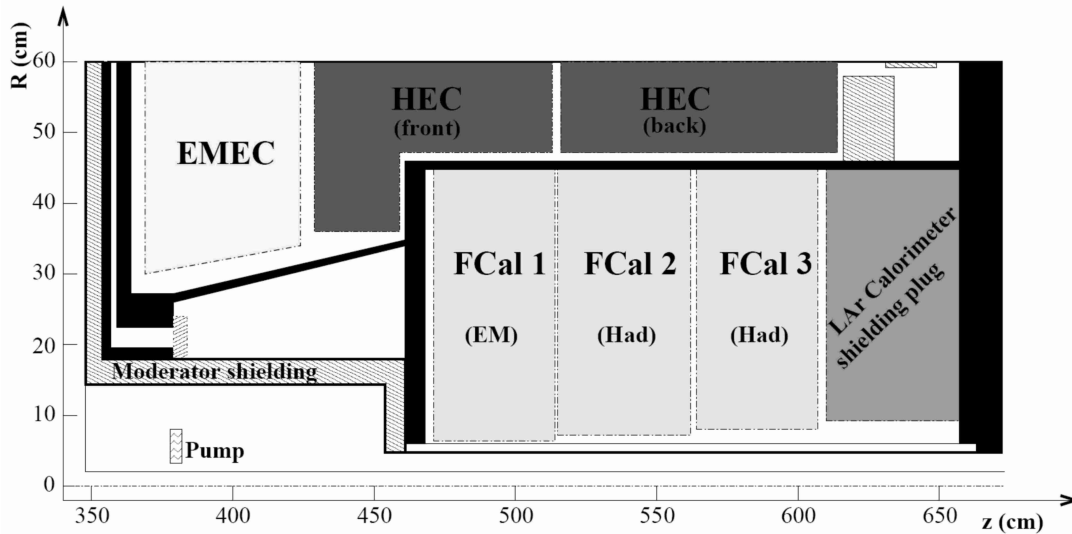
Figure 4.5: Schematic view of the ATLAS FCal [ATLj08].

Due to the high particle flux, the thickness of the LAr gaps is designed to be very small, 0.269 mm for the EM, 0.376 mm for the first, and 0.508 mm for the second hadronic calorimeter, seen in the direction pointing outwards from the interaction point. The small depths of the gaps avoid large ion build-ups in the active material and provide fast signals. The forward calorimeter features 3 500 readout channels [ATLj08].

4.3 The Inner Detector

The ATLAS Inner Detector (ID) consists of three subdetectors in a hermetic system, providing high resolution track measurements, which result in precise position information for primary and secondary vertices.Figure 4.6 displays the three subdetectors: The Transition Radiation Tracker (TRT), the Semi Conductor Tracker (SCT) and the pixel detector. The ID is enclosed by a cylindrical shell of 7.024 m length and 2.30 m diameter, placed inside a 2 T solenoidal magnetic field. The ID covers a range of $|\eta| < 2.5$ [ATL99a, ATLj08].

The TRT is a straw drift tube detector, which is segmented into a centred barrel and two end-cap sections. Each section provides 36 layers of straw tubes with 4 mm diameter and resolutions of roughly 0.2 mm. The barrel section is comprised of 52 544 straws (144 cm length) and each of the end-cap TRTs contains 122 880 straws of 37 cm length.
The detector design utilises the physics principle, that a charged particle, which crosses the border between two materials, with different dielectric constants, emits electromagnetic radiation (transition radiation). At the expected high particle energies soft X-rays will be emitted, which can be detected very easily.
The gaseous proportional straw tubes are designed as drift chambers and are filled with a gas mixture of Xe, CO_2, and O_2. Two detection thresholds are set, a low one for traversing charged particles at an energy of roughly 250 - 300 eV and a high one at about 7 keV. If
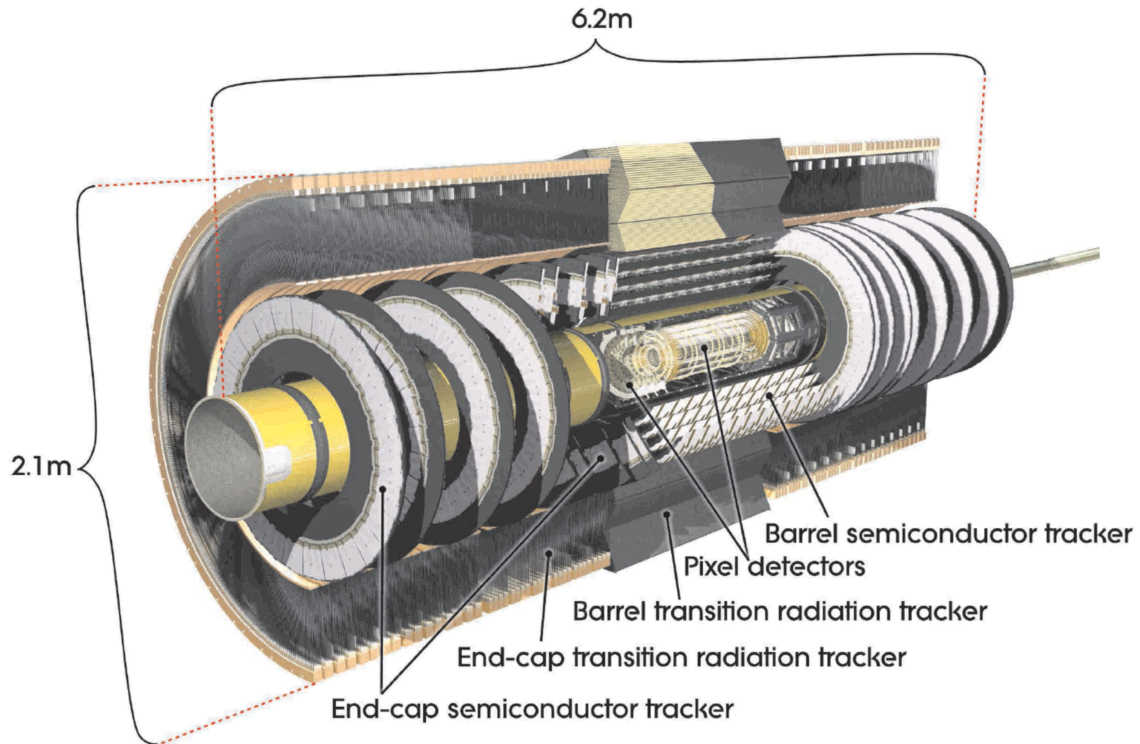
Figure 4.6: Cut-away view of the ATLAS Inner Detector [ATLj08].

a signal crosses both, its origin is a TR photon [EB03, ATL99a, EA03].

The Semi Conductor Tracker is located between the pixel detector and the TRT and contributes four space point measurements (eight silicon strip crossings) per track to the high precision tracking conglomerate of the Inner Detector. It consists of four barrel layers and nine discs per end-cap, which are positioned perpendicular to the beam axis. The SCT features 4 088 silicon modules and provides a space point resolution of $\sigma_{R\phi} = 16$ μm and $\sigma_Z (\sigma_R) = 580$ μm. One module consists of four sensors, arranged in two layers of two wirebonded sensors each. These are glued back to back on a carbon structure and are aligned in a stereo angle of ($\pm$ 20 mrad).
One sensor features 786 readout strips with a constant pitch of 80 μm and a length of 6.4 cm. For the overall dimensions of the Inner Detector see Figures 4.7 and 4.8 [ATL99a, ATLj08, JJ05].

4.3.1 The Pixel Detector

The innermost subdetector of ATLAS is a silicon pixel detector. This detector type was chosen because of the need for excellent three dimensional space point resolution at high track densities. The ATLAS pixel detector is one of the most important factors for the successful b-tagging of jets, determines decisively the ability of secondary vertex reconstruction, and provides critical tracking information for pattern recognition. Secondary vertices are caused by e.g. the decay of B-mesons. The detector has to work in a high
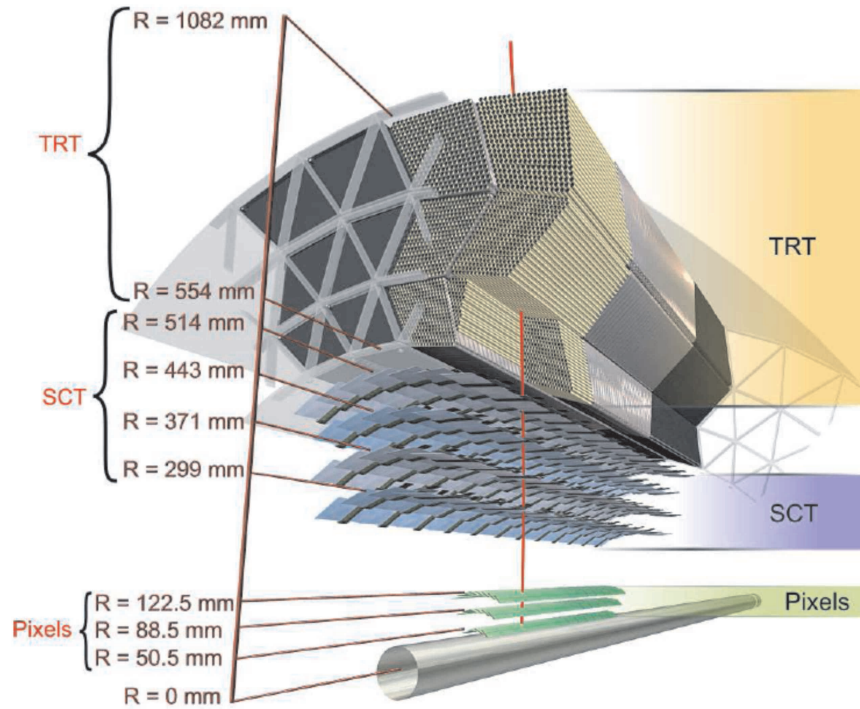
Figure 4.7: Schematic layout of the Inner Detector Barrel, without containment [ATLj08].
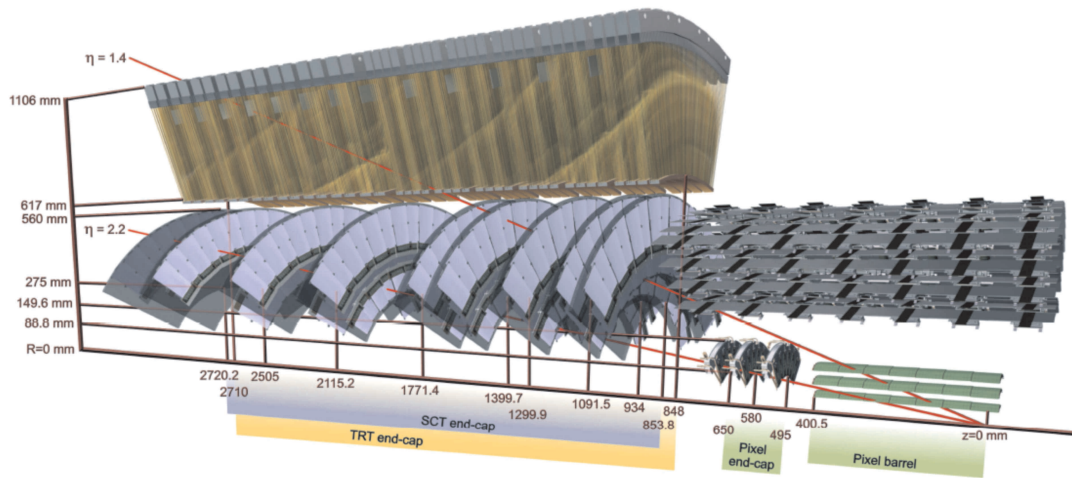
Figure 4.8: Schematic layout of the Inner Detector Discs, without containment [ATLj08].

level radiation environment, in which it has to withstand an estimated lifetime dose of 500 kGy (or 10^{15}_{neq} cm^{-2}) over ten years of operative lifetime [ATLEl08].

The pixel detector measures three space points in a region of $|\eta| < 2.5$ with a resolution of 12 μm in r/ϕ and 100 μm in z-direction. The finer segmentation in r/ϕ was chosen to ensure a precise transversal momentum measurement, which is essential for energy reconstruction. Overall 1 744 identical sensor modules are built into three concentrical barrel layers and two end-caps with three discs each in the forward region, as can be seen in

Figure 4.9. For radii and overall dimensions see Figures 4.7 and 4.8 [ATLPix98].
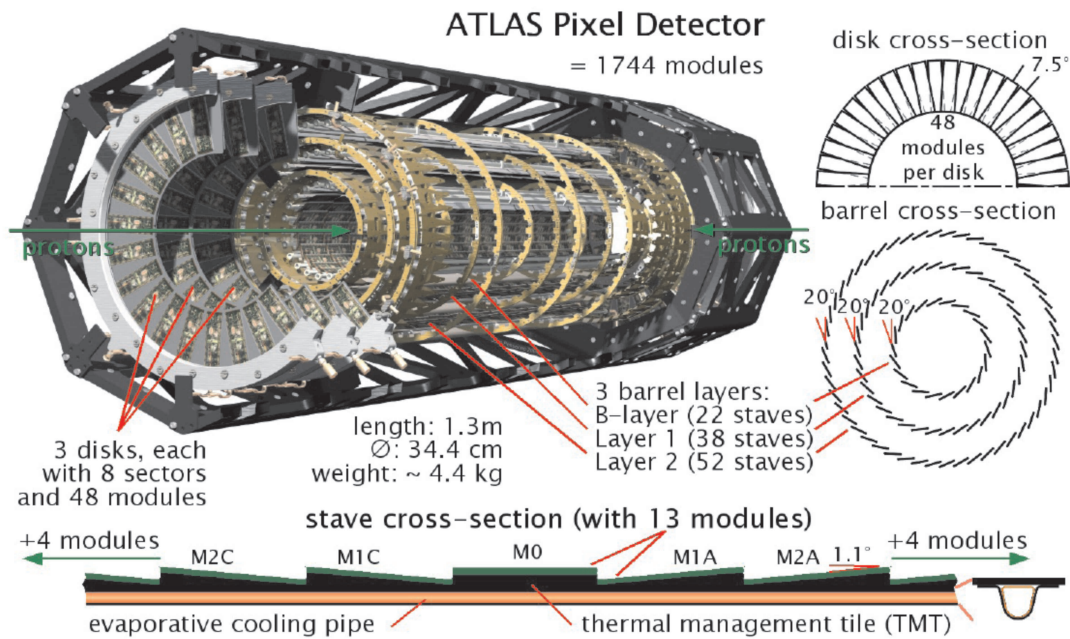
Figure 4.9: Cut-away view of the ATLAS pixel detector [ATLj08, DD07].

Every layer consists of a different number of carbon support structures (staves), that carry each 13 Pixel Sensor Modules. These staves are organised in pairs of two (called bistaves), sharing one linked cooling pipe on their backside (the side facing away from the interaction point). Carbon is used because of its stiffness and low weight, which reduces the number of passive structures to a minimum and prevents multiple scattering processes. In order to avoid detector insensitivities, the modules are inclined in z- and azimuthal direction (Figure 4.9). Along the beam axis there is an angle of $0.9°$ facing towards the interaction point and the centre module of each stave lies parallel to the beam line. In azimuthal direction the modules are tilted by $20°$ and overlap. The overlap has the advantage, that the detector alignment, which is crucial for exact track and vertex studies, can be checked by measuring tracks in these overlap regions. Moreover dead spots are prevented. There are 286 modules in the B-Layer, 494 modules in Layer-1 and 676 modules in Layer-2. Each disk is equipped with 48 modules in two layers, enclosing a tilt angle of $7.5°$ between two components. The ATLAS pixel detector utilises over 80 million readout channels [ATL99a, ATLj08].

4.3.2 System Architecture

Figure 4.10 illustrates the ATLAS pixel detector system architecture. There are 16 Front-End chips (FE) organised in two rows of eight chips. They are read out by a Module Controller Chip (MCC), using Low Voltage Differential Signaling (LVDS) serial links. The Optoboard is an on-detector digital-optical converter from where an optical fibre connects every module to the off-detector Read Out Drivers (RODs). One down link is used for transmitting clock-, trigger-, command-signals, and configuration data and two up links are used for the event data readout.

The readout is configured in a 'data-push' architecture, which means, that each segment of the chain always transmits with its maximum rate. Every upstream component monitors the data stream and compares the number of received events with the number of trigger signals. If the difference exceeds a defined value, the trigger downstream is blocked and empty events are generated [ATLEl08].
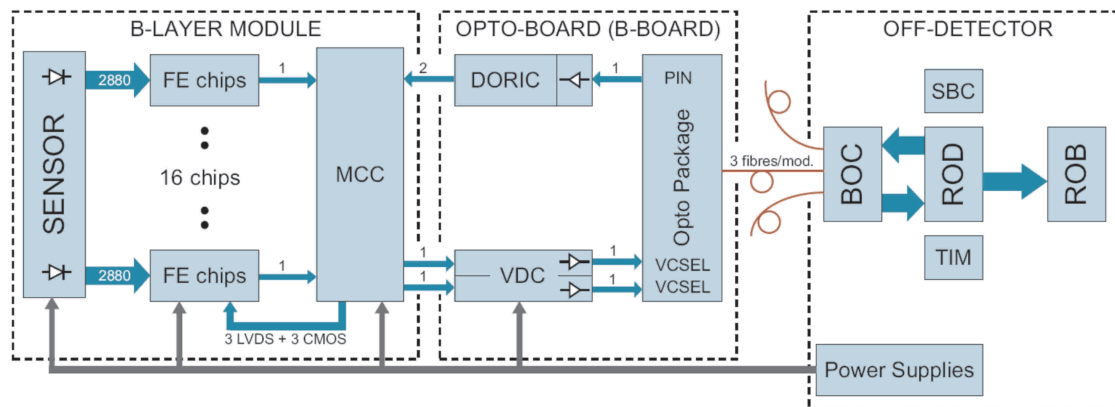
Figure 4.10: Block diagram of the ATLAS pixel detector system architecture [ATLEl08].

4.4 The Pixel Module

The ATLAS pixel detector utilises approximately 1.7 m^2 of sensitive area, built by 1 744 uniform sensor modules. The Pixel Module is a combination of sensor and front-end/readout electronics. It features 6.08 cm×1.64 cm of detecting surface.
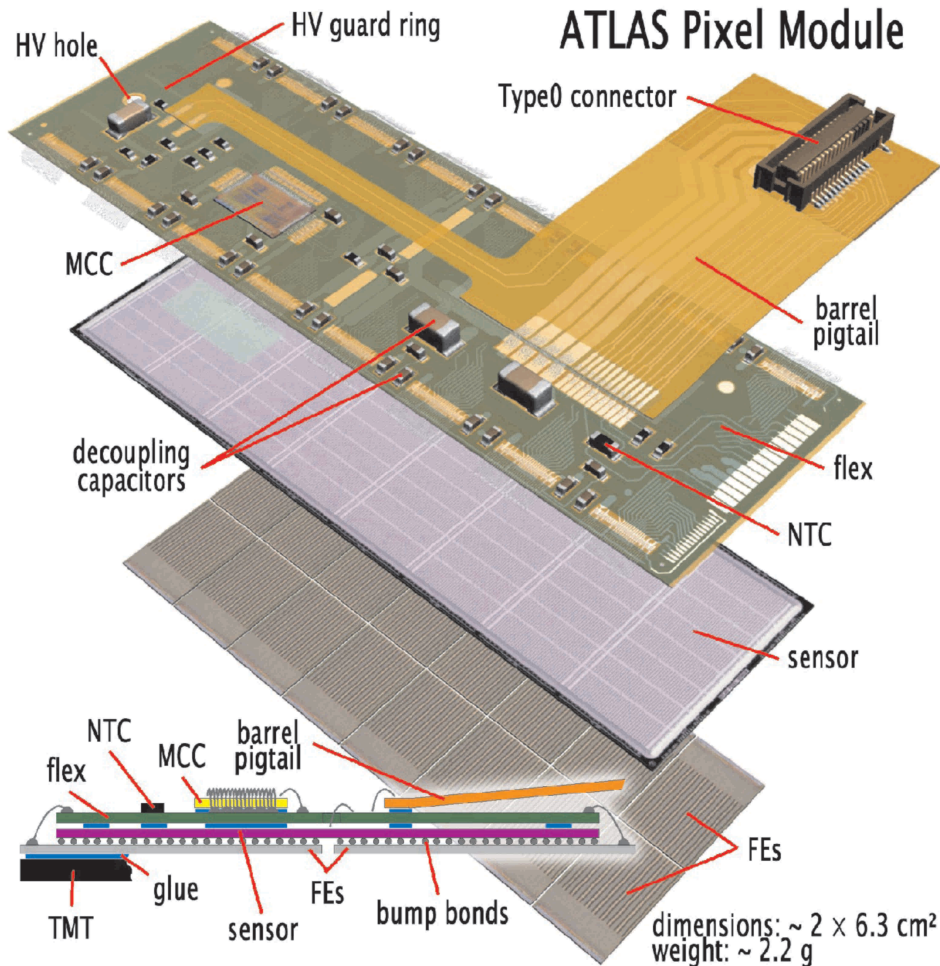
Figure 4.11: Exploded view of an ATLAS Pixel Module [DD07].

4.4.1 Sensor Tile

The sensor tile contains 47 232 pixels, consisting of a 256 μm thick n-bulk, close to intrinsic charge concentration. A schematic cut through one pixel sensor and its connection to the FE electronic is shown in Figure 4.12. The sensor functions by creation of a wide depletion zone between the n$^+$ implant on the readout side and the p$^+$ implant on the opposite side, by utilising the pixel as a reversely biased diode. According to Section 2.4.4 a traversing MIP generates approximately 20 000 electron-hole pairs in the ATLAS Pixelsensor.
89 % (128 columns) of the pixels have a size of 400 $\times$ 40 μm^2, these pixels are in this

26

thesis referred to as normal pixels. 11 % (16 columns) have a size of $600 \times 50~\mu m^2$ and are referred to as long pixels. In each column, the eight centre pixels are wired to pairs with a common readout, these pixels are called ganged pixels. There are 320 independent readout rows, corresponding to 40 680 readout channels. This design matches the requirement to connect the sensor tile to the 16 FE chips.
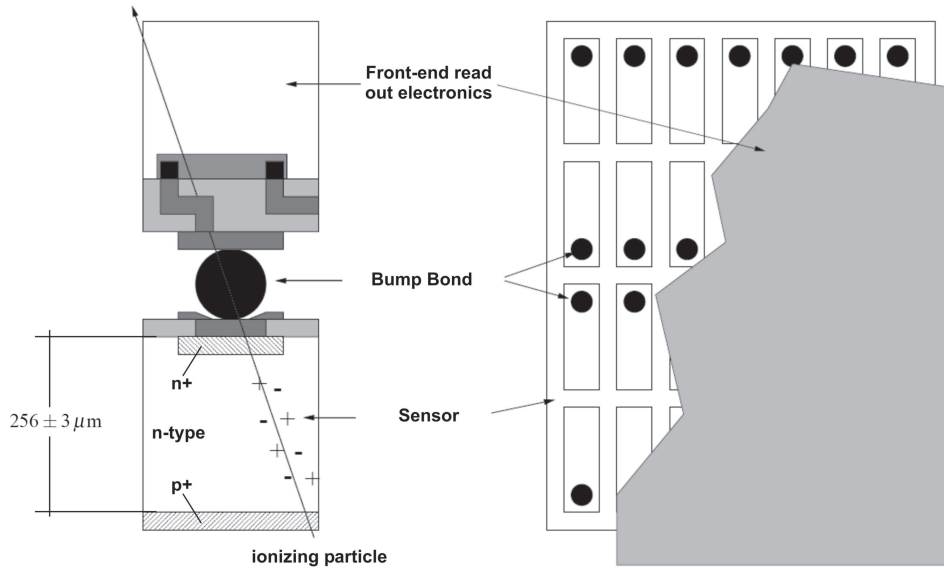
Figure 4.12: Schematic cut through a pixel and it's FE electronic [FH01].

The sensor design ensures the electrical isolation of the pixels and their functionality in a high level radiation environment. Most of the radiation damages occur when a particle traverses the active silicon material and deflects a lattice atom from its place. The deflected atom, as well as the vacant position, can migrate through the lattice and, if the energy is sufficicient, create new defects. These impurities can accumulate and form clusters, which also move through the silicon matrix (at high temperatures) and cause further damage. Radiation damages change e.g. the depletion voltage (because of the disbalance in charge concentration), leading to an increase of the current of the reversely biased diode (leakage current) and a lowering in the charge collection efficiency.
In the material used, the doping of the n-bulk will invert (type inversion) during irradiation, due to a rise in acceptor producing defects. Moreover the depletion voltage will first decrease and, after type inversion, increase again to a point, where full depletion of the active material is no longer possible [Mo99].

4.4.2 Front End Electronic

The bottom layer of the Pixel module (Figure 4.11) is the Front-End (FE) electronics, which is segmented into 16 equal chips. Each chip contains 2 880 pixel cells (the analogue part is shown in Figure 4.13) and the corresponding amplifier circuitry. The sensor tile is connected to the FE via bump bonds. Two different techniques for bonding were used,

an electroplated-solder (PbSn) bumping and an evaporative-indium bumping, which show slight differences in the charge collection efficiency. Every pixel is connected to one pixel cell with one bonding, aside from the ganged pairs, where two pixel utilise one readout cell. Therefore, the arrangement of the pixel cells follows the the sensor tile row/column structure.
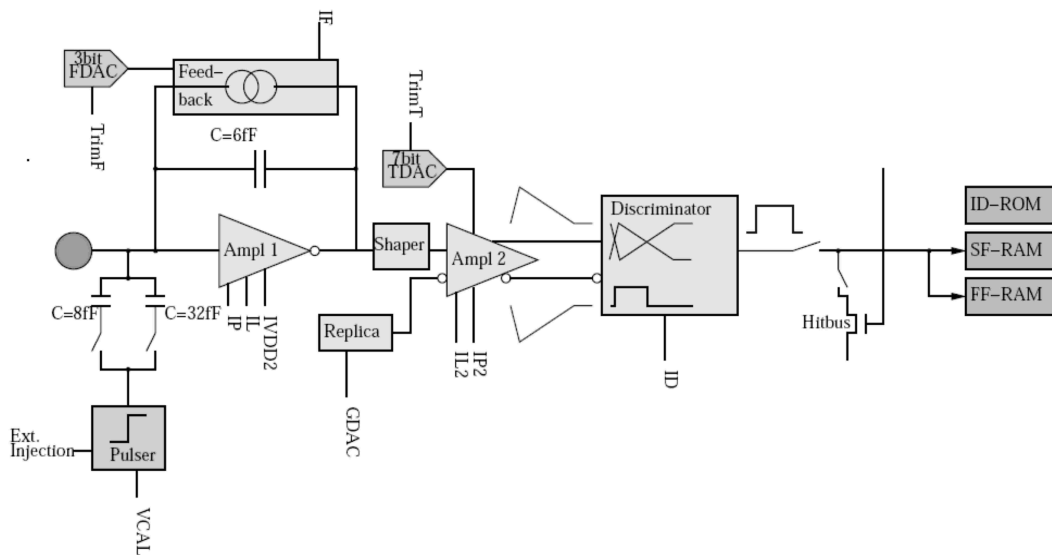
Figure 4.13: Block diagram of the analogue part of one pixel cell [TF06]

.

The power consumption of a pixel module is 35 mA at 1.6 V for the analogue and 75 mA at 2.0 V for the digital segment. The detection of a particle, traversing the sensor tile, starts in the depletion zone inside the n-bulk, where electric charges are set free through ionisation. These charges are collected and pass the bump bond (represented by the circle on the left side of Figure 4.13), causing a signal, amplified by the first charge sensitive amplifier.
This signal is then integrated by a 6 fF feedback capacitor and discharged through the feedback circuit, by a constant current. After passing a second amplifier the signal has an approximately triangular shape, representing the charging and discharging of the feedback capacitor. The signal amplitude is proportional to the charge collected in the pixel sensor. This triangular shaped signal is fed into the discriminator, its output is a defined Time over Threshold (ToT) signal with a rectangular shape. The length of this pulse is counted in units of 25 ns, corresponding to the bunch crossing rate of the LHC (detailed description in Section 5.1). This signal can be adjusted by the use of three Digital-Analogue-Converters (DACs). The FDAC (Feedback DAC), affecting the slope of the pulse's falling edge, by regulating e.g. the current, which discharges the feedback capacitor, the GDAC (Global DAC), globally (module wide) effecting the threshold of the discriminator and finally the TDAC (Trim DAC), which does the same for each pixel cell separately. All three DAC adjustments afflict the width of the ToT pulse, which is proportional to the energy deposited in the sensor.

A time stamp (one for the rising and one for the falling edge) and the Cell ID are stored

in the TE (Trailing Edge) and the LE (Leading Edge) RAM. These memory blocks are labelled as SF and FF RAM in Figure 4.13(german: 'Steigende Flanke' and 'Fallende Flanke'). The time stamp is generated by a Gray-coded 8 bit counter, triggered by the 40 MHz LHC-clock, i.e. time information is only available in units of 25 ns.

The pixel cells are arranged in nine double columns with 160 rows each, that feed the ToT time stamps and the cell ID into the End of Column (EoC) buffers. Every double column is connected to 64 EoCs. The EoC's logic calculates the ToT value as the difference between the LE and the TE time stamp. This comparison is achieved with respect to a delayable clock signal. By choosing the correct delay value, the effects of Time of Flight and different cable lengths can be compensated. That minimises the assignment of simultaneous hits to different bunch crossings. The EoC can also compensate the timewalk effect (described in Chapter 5.1), by copying ToT values below a certain threshold and their positions into the datastream of the precedent bunch crossing. This procedure is called hit doubling.

If the arrival of a Level-1 trigger signal plus a programmable latency coincides with the LE time stamp of the hit, the time information is written into the trigger FIFO (First In First Out 16 word memory) and the readout sequence is initiated. This sequence scans the EoCs for the corresponding time stamp. If hits are found they are transferred to the Module Controller Chip (MCC). If no hit is found, the FIFO entry is deleted [TF06, ATLPix98, ATLEl08].

4.4.3 Module Controller Chip

The sensor tile is followed by the Flex Hybrid (Figure 4.11), which is a double-sided, flexible, printed circuit, with a thickness of about 100 μm, that routes signals and powerlines [ATLEl08].
The Module Controller Chip (MCC) is fixed on the Flex Hybrid. The MCC is a central part of the Pixel module. It has a wide range of tasks to fulfill in a harsh radiation environment: Distribution of the LHC clock or Level 1 Trigger signals from the muon system, readout of FE data, event building and data transmission, storing, managing and distribution of configuration data for the FEs (e.g. DAC settings).
A block diagram of the MCC architecture is shown in Figure 4.14. The final design of the MCC was produced in 2003 (MCC-I2.1) and featured 880 000 transistors on an area of 6.84×5.14 mm^2, implemented in 0.25 μm CMOS-technique (Complementary Metal Oxide Semiconductor) [ATLEl08].
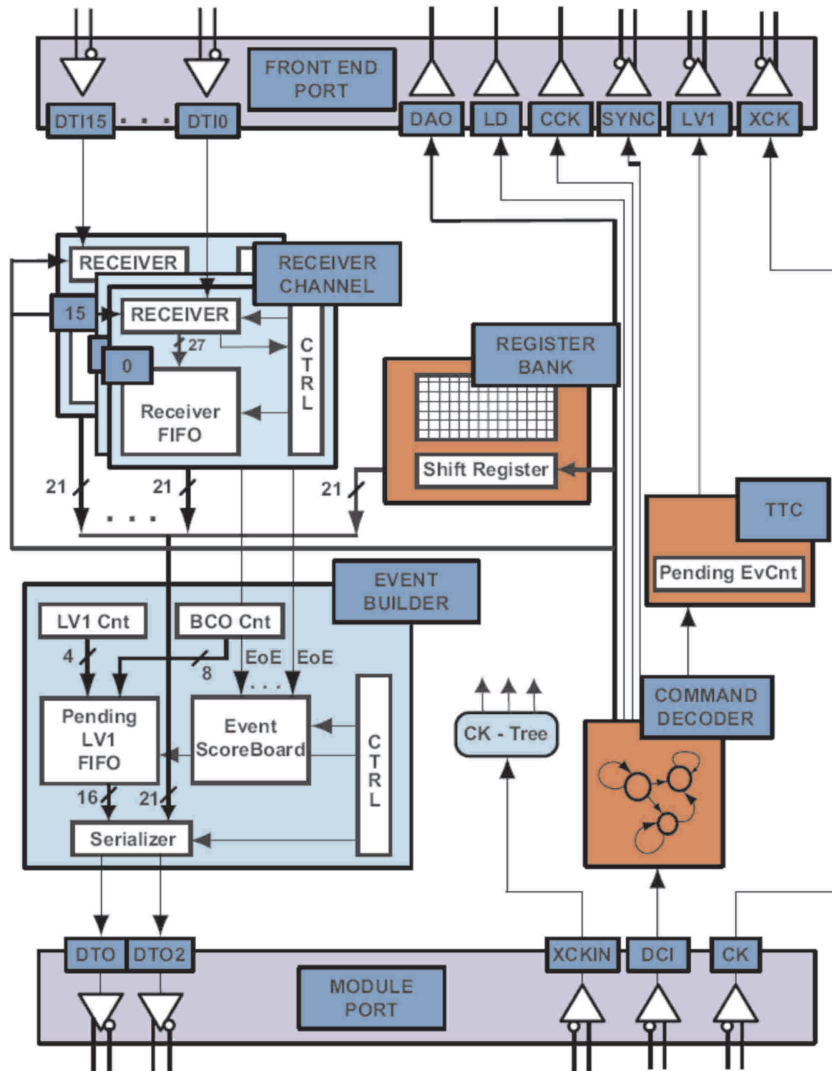
Figure 4.14: Block diagram of the internal architecture of the MCC [ATLEl08].

The tasks of the operational blocks are:

- *Command Decoder*: Decodes Level-1 trigger signals, read/write operations to internal MCC registers and FE chips,

- *Timing Trigger and Control*: Generates Level-1 Trigger and reset signals, can provide calibration strobes,

- *Front End Port*: Interface between the MCC core and the FE chips,

- *Receiver Channel*: 16 receiver blocks, one for each FE chip(128×27 bit deep), monitoring the input lines. Hits are stored in the receiver FIFO and are managed by the Controller (CTRL), which is also capable of recognizing End Of Event (EoE) lines send by the FE chip, completing the hit input,

- *Register Bank*: Set of configuration and status registers. The MCC architecture allows up to 16 (16-bit) general purpose registers,

- *Event Builder*: Contains two tables used for event generation. Pending Level-1 FIFO (Lv1FIFO), storing the content of the Level 1 trigger counter (L1Cnt) and the Bunch crossing clock Counter (BcoCnt, 40 MHz) when a Level 1 trigger signal is processed. When the hit corresponding to the Level trigger signal is retrieved, the Lv1FIFO content is written to the Event Block. The Event Scoreboard surveys the complete events, that are stored in the Receiver FIFO. If an event is completely stored in the MCC it is transmitted to the Event Builder,

- *Module Port*: Interface between the MCC core and the ROD.

In the following the three main tasks, configuration management, trigger (reset and timing) and event building, are described in detail:

As illustrated in Section 4.4.2, the FE-electronic has to be supplied with configuration data, like the DAC settings for the controlled discharging of the feedback capacity of every pixel (see Figure 4.13). Since there is no solid state storing device, the configuration data has to be restored after every power-up.

The second main task is the distribution of Level-1 (LVL1) trigger signals, initializing the readout from the EOC buffers. When a trigger signal is processed by the MCC and there are less then 16 unprocessed events (Lv1Cnt $<$ 16), the Trigger, Timing and Control Chip (TTC) sends a trigger signal to the FE chips. In the case, that there are more than 16 unprocessed instances, the incoming trigger signal is not distributed to the FE chips and the corresponding event is lost.
The number of missing events is sent to the Read Out Drivers (RODs) to maintain the event synchronisation. Furthermore, the TTC can issue reset signals to multiple FE chips or to the MCC, like the BCR (Bunch Crossing Counter Reset), which is issued after every beam turn of the LHC, or the Event Counter Reset, which triggers the deletion of all unprocessed event data.
Calibration strobes to the FE chips are provided by the TTC logic to calibrate the analogue pixel cells. The delay of the strobe (with respect to the clock) can be adjusted in steps of 0.5 ns. The strobe delay is varied by a number of 0 to 63 delay counts with a length of roughly 0.5 ns/count for delay range zero and approximately 2.5 ns/count. The MCC can send out the data of up to 16 bunch crossings stored in the EOC buffers. These

time windows of 25 ns are called Level-1 trigger Accept (LVL1A). For studies of cosmic particles six LVL1A windows are read out [AtA08], when the LHC runs at maximal luminosity only one LVL1A window will be read out [RB02, ATLEl08].

Event building is the function, that requires most of the space of the MCC. It includes the receiver channel- and the Event-Builder- block. From the FE chips, a serial data signal is sent as a response to the Level-1 trigger signal. The data is buffered in the 16 FIFO memories, which are used to derandomise the data stream, extract single events, and prepare the data for transmission to the RODs. The data transmitted to the ROD is structured on an event-by-event basis, i.e. the FIFO stores all subsequent hits, until an End of Event word is generated. Then a truncated event flag is stored in the receiver FIFO and in the MCC output stream. This prevents the output of corrupted event data (e.g. by buffer overflows). When the Event Builder das received all data of one event it starts the build-up and the transmission. First a Bunch Crossing Identifier (BCID) and a Level-1 trigger identifier is written to the data stream, then all FIFO data until the EoE word is read out and transmitted. After that, a trailer word informs the ROD, that the event has ended [ATLEl08].

4.5 Trigger System

The LHC is designed to run at a bunch crossing rate of 40 MHz, with a luminosity of 10^{34} cm^{-2}s^{-1}. This leads to an interaction rate of about 10^9 Hz. At this point, the corresponding bandwidth and data storage capability needed for this amount of data cannot be provided. So the events stored have to be constrained to those that include interesting physics. The technically feasible rate, to store selected event data, is 100 Hz. The event selection is accomplished by a three level trigger system, one hardware based (Level-1) and two software based (Level-2 and Event Filter) [ATLTrig98].

Figure 4.15 shows a simplified block diagram of the three trigger stages, which are used in ATLAS. The Level-1 Trigger (LVL1) reduces the event rate from 1 GHz to 75 kHz (upgradable to 100 kHz). Due to the complexity of the events at the LHC an event selection within 25 ns is not possible. Therefore, it is necessary to store the events in pipeline memories (as the EoC buffers in the Pixel Modules) and extend the time for the decision. The trigger decision is based on low granularity information from fast subdetectors (RPC, TGC, ECal) either in coincidence or as a veto. The trigger selection is programmable and can be revised to select more complicated signatures. The target latency of the LVL1 Trigger signal to arrive at the subdetectors is 2 μs plus 0.5 μs as a safety margin. Selected events are read out from the pipeline memories and are sent to the readout buffers (ROB). To prevent instabillities, caused by high event rates, intermediate buffers (derandomisers) normalise peaks and match the data flow to the available bandwidth [ATLTrig98].

The selected event data is stored in the ROBs until it is rejected (and deleted from the ROBs) or accepted by the Level-2 Trigger. The data in the ROBs is composed of fragments of one event with one fragment per ROB. The event building process assembles all these fragments into a fully reconstructed event, which can be accessed by the Event
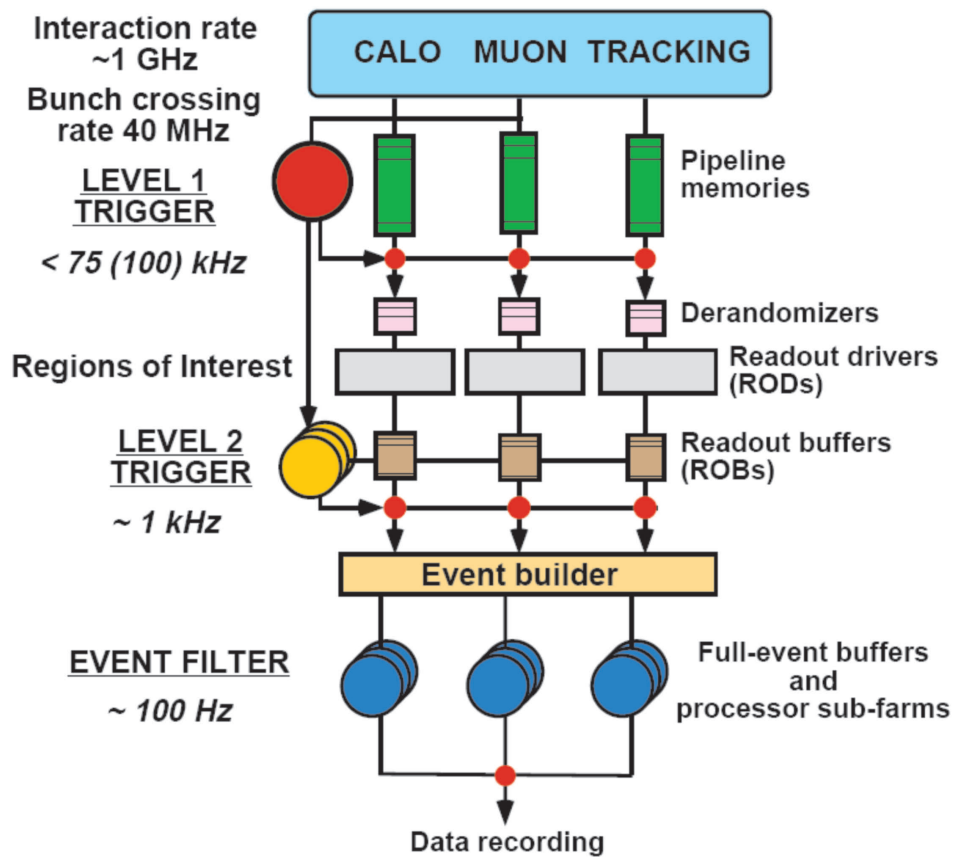
Figure 4.15: Simplified block diagram of the ATLAS trigger system [ATLTrig98]

Filter. The Level-2 Trigger utilises the Region of Interest (RoI) information provided by the Level-1 Trigger, to select data from the ROBs. RoI data includes position (η and ϕ), the p_T range of candidate objects (muons, electrons, hadrons, jets) and energy sums. The Level-2 Trigger reduces the event rate to roughly 1 kHz and has a latency of less than 10 ms averaged per event [ATLTrig98].

The last stage of selection is performed by the Event Filter, which further reduces the event rate to 100 Hz with an estimated event size of 1 Mbyte. Contrary to the Level-2 Trigger, the Event Filter uses fully reconstruced events for the selection and its algorithms take up to 1 s to decide if an event is stored permanently [ATLTrig98].

5 Timing of the ATLAS Pixel Detector

This chapter discusses timing related issues. In this thesis the term 'timing' refers to the assignment of the correct Bunch Crossing Identifier (BCID) to a hit in a sensor of the ATLAS pixel detector. If the detector is ideally 'timed', most of all hits from one bunch crossing are assigned with the right BCID. To adjust the timing of the detector, the readout of earlier arriving (fast) signals has to be delayed, compared to the readout of later arriving (slow) signals. This is achieved by delaying the clock, which triggers the BCID generation, see Section 5.3. A misstimed detector loses possibly important data of the initial bunch crossing

The effects, in which the timing differences originate, have unique characteristics for each pixel module. In fact, the timing is different between the analogue pixel cells, but it can only be adjusted for the whole module, because the BCID generation is triggered module wide by the MCC. Effects influencing the timing are the ToF of the detected particles, cable lengths and the timewalk effect.

The ToF is the time a particle needs to traverse from its point of origin to the sensor where it is detected. Differences in ToF depend on the detector geometry. The signal transmission time is proportional to the cable length, which depends on the cable ducting to the in- and off-detector signal-processing stages. The timewalk effect is described in Section 5.1.

5.1 Timewalk Effect

As described in Section 4.4, the charge generated in the pixel sensor is collected by the feedback capacitor of the charge sensitive preamplifier. The feedback capacitor is discharged by a constant current (c.f. Figure 4.13). The preamplifier response to this charge signal has a nearly triangular shape, where the risetime of the signal $t_{passage} + t_{drift}$ is independent of the charge generated in the pixel sensor. Therefore the slope of the leading edge of the output signal depends on the charge generated in the sensor. The length of the trailing edge can be changed by adjusting the feedback current, which discharges the capacitor. In Figure 5.1 the signal from charge Q_a crosses the discriminator threshold later than the signal from charge Q_b. This behaviour is called timewalk effect.

The diagram (a) in Figure 5.1 shows an estimated charge signal of two traversing particles with different charge depositions. The passage time $t_{passage}$ is the time, that the particles need to cross the sensor and the drift time t_{drift} is the time the electrons need to be collected at the sensors anode. Diagram (b) shows the output signals of the preamplifier. The signal for a charge Q_a (solid line) has the same risetime as the signal originating from a larger charge deposition (dashed line). Due to a smaller peak value, the signal of the smaller charge crosses the discriminator threshold later, see (c).

The difference between the arrival time of the fastest hits and the leading edge of the ToT pulse is called timewalk.
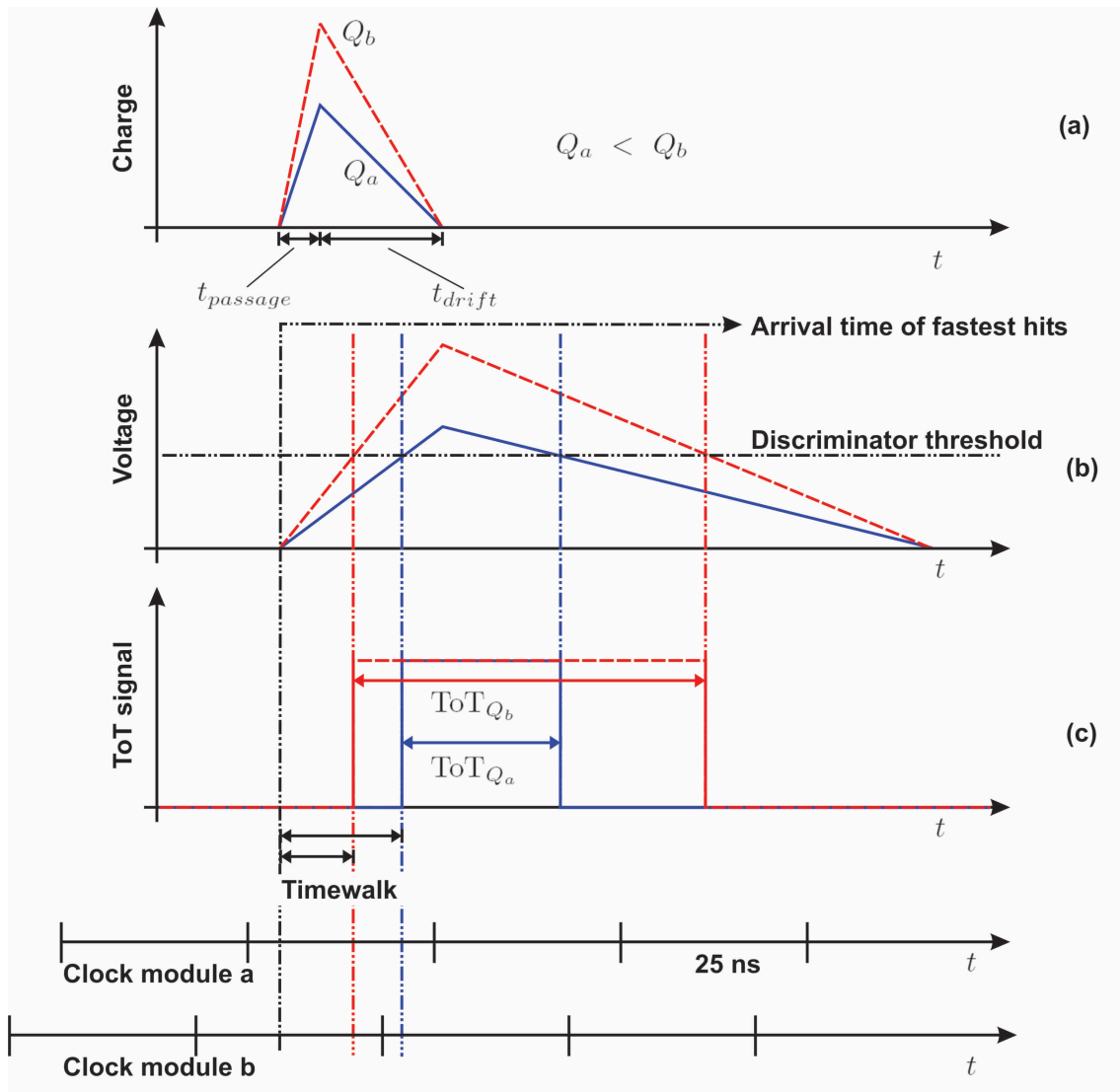
Figure 5.1: Origin of the timewalk, triangular pulse-shapes in (b) are approximated.

On the bottom of Figure 5.1, two hits, originating from the same event, are assigned to two different bunch crossings, due to a wrongly adjusted clock phase and additionally to the timewalk effect.

The BCID is generated by the Central Trigger Processor (CTP) readout logic, using a 12 bit counter. This counter is reset by the Bunch Counter Reset signal, which is generated on receipt of the LHC ORBIT signal from the Timing Trigger and Control (TTC). The ORBIT signal is a square wave of period 88.924 s, which is received from the LHC machine and used for the generation of signals which are synchronised to the LHC orbit [ATLTrig98].

The phase of the module clock is adjusted in such a way, that hits with large energy deposition (resulting in charges of about $100\,000$ e$^-$) cross the discriminator threshold 5 ns after the beginning of the rising edge of the module clock. This difference of 5 ns is chosen as a safety margin to level out differences in the response behaviour of the pixels, consequently 20 ns remain for the detection of signals. If a hit arrives within this readout window, the hit is detected in-time. If the module clock is adjusted as described, the loss in efficiency due to the timewalk effect is minimised.

A typical charge/ToT relation is shown in Figure 5.2.
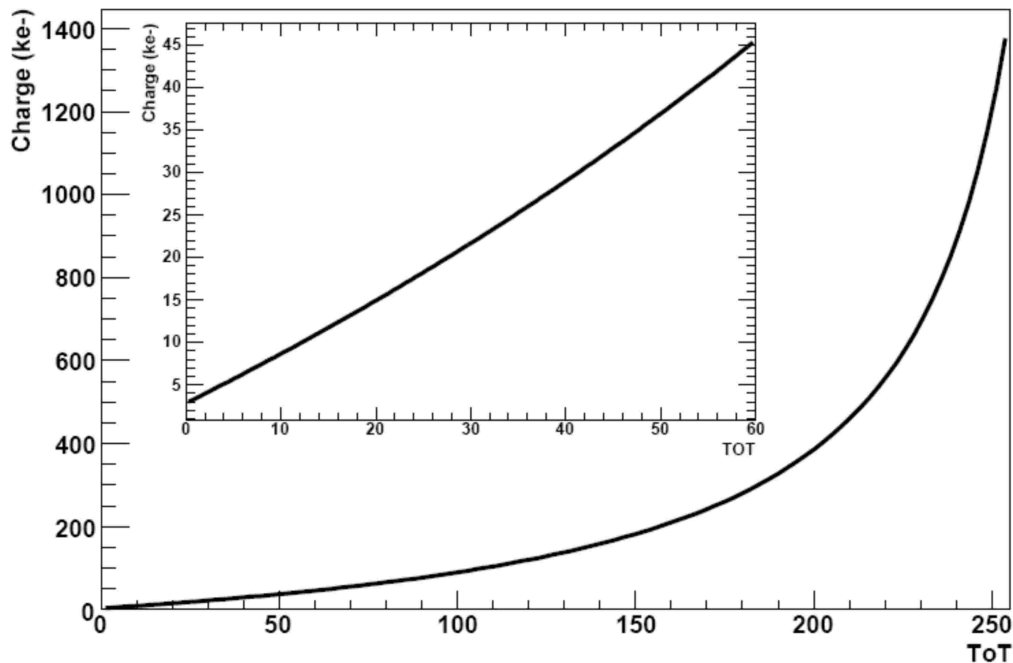
Figure 5.2: Typical relation between generated charge and Time over Threshold values [TF06].

The translation between the collected charge and the resulting ToT values was determined for each pixel during the production measurements for each FE chip. The $ToT\,(Q)$ calibration function was chosen to be

$$ToT\,(Q) \;=\; A \cdot \left(\frac{Q + E}{Q + C}\right), \tag{5.1}$$

with A, C and E as fit parameters, which are determined by fitting function 5.1 to a distribution of injected charges vs. the measured ToT values. Charges can be injected via the external injection line (Figure 4.13).

5.1.1 Timewalk Parameterisation

The typical profile of a delay distribution is shown in Figure 5.3, which is the result of a calibration scan performed at a test setup for pixel detector modules. In order to detect hits with a low ToT value in the desired time window, hits with low ToT values have to be delayed less than hits with high ToT values. For very high charges (three or four times the MIP-charge) the timewalk is considered to be zero. For charges in the order of the pixel threshold the timewalk is high. For increasing input charges the timewalk shows an exponential decrease. The parameterisation of the delay profile has to match these physical constraints.
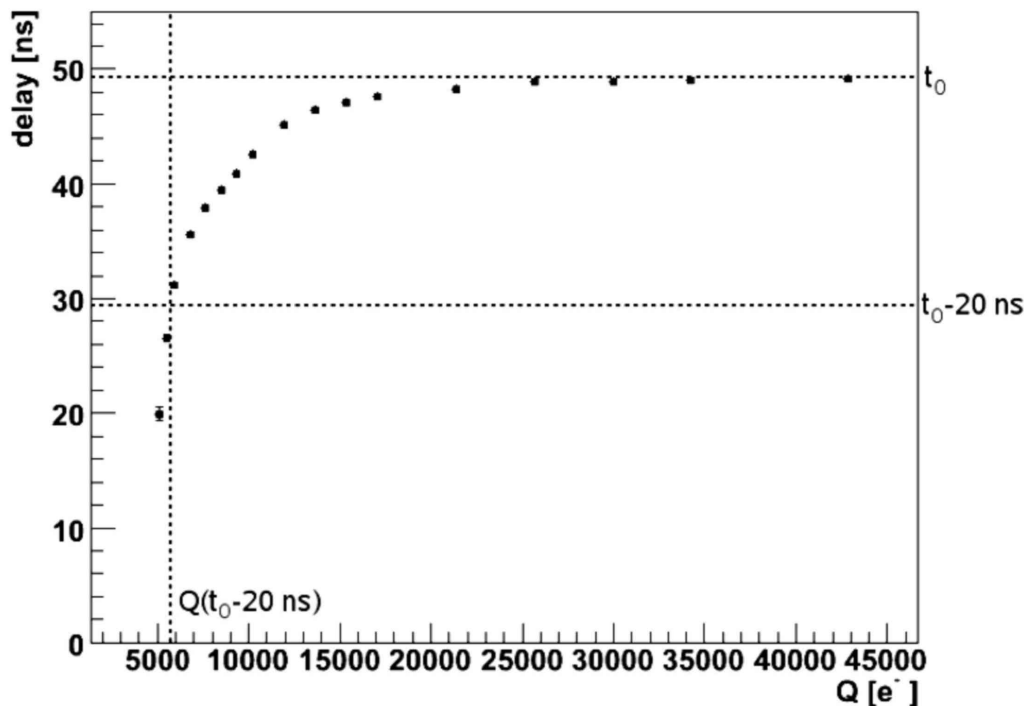
Figure 5.3: A typical delay profile, which is the result of charge injections into the external injection line of a pixel cell [MK08].

(5.2) shows the parameterisation of the delay, measured in Figure 5.3,

$$delay\left(Q_{signal}\right) = t_0 - \underbrace{\frac{P_0}{\left(Q_{signal} - P_1\right)^{\alpha}}}_{\text{timewalk}} \ , \tag{5.2}$$

with t_0, P_0 and P_1 as free parameters. Whereas parameter t_0 describes the delay value for a hit with high charge deposition. This delay is the result of cable lengths, computing times and ToF, which are different for each module of the ATLAS pixel detector. So the value of t_0 is an offset to the timewalk. For high charge depositions the timewalk is zero, because the signals from these charges cross the discriminator threshold almost instantaneously. The constant exponent in (5.2) is determined to $\alpha = 2.5$. For this value the χ^2 for all modules tested in [FL07] converged.

The timewalk and the delay profile differ slightly for different pixel types, which are described in Section 4.4.1, e.g. long pixel have a different charge collection characteristic, due to their bigger volume. If not stated explicitly, all figures in this thesis are based on data from normal pixels.

As shown in [FL07] the timewalk parameters P_0 and P_1 are correlated with the overdrive Ω (see Section 5.2) and can be calculated using the following equations:

$$P_0 = A_0 \cdot \Omega + B_0, \tag{5.3}$$

$$P_1 = A_1 \cdot \Omega + B_1, \tag{5.4}$$

with
$$A_1 = 7.675 \times 10^7 \text{ ns} \,(e^-)^{1.5}, \quad B_0 = -2.648 \times 10^{10} \text{ ns} \,(e^-)^{2.5},$$
$$A_1 = -1.597, \qquad\qquad\qquad B_1 = 943 \; e^-.$$

Correlation between the TW parameters and the overdrive according to [FL07], the overdrive is the difference between the in-time threshold and the threshold of a pixel cell, see Section 5.2.

5.2 In-Time Delay

The in-time delay is the period between the particle passage through the sensor, corresponding to the hit recognition in the discriminator. If this period is smaller or equal to the length of the readout window (25 ns diminished by 5 ns safety margin), the hit is assigned to the correct bunch crossing and is presumed to arrive 'in-time'. Figure 5.4 shows the correlation between low ToT values and the in-time delay.

In order to understand Figure 5.4, the two terms 'threshold' and the 'in-time' threshold need to be explained:

- The threshold (discriminator threshold) of a pixel is defined as the amount of charge deposited in the sensor for which the detection efficiency of the pixel cell exceeds 50 %.

- The in-time threshold is the smallest charge detectable within the 20 ns readout window of a well calibrated FE chip.

By using Figure 5.2, the exemplary in-time threshold value of 4 ToT, derived from Figure 5.4, can be translated into a charge of approximately 5 000 e^-. A Minimum Ionising Particle (MIP) deposites about 20 000 e^- (most probably value) in the pixel sensor. This is above the value of the in-time threshold derived from Figure 5.4.

That assumption holds true, if the particle traverses one single pixel, but it is possible that up to four adjacent pixels are hit by the same particle and the deposited energy is shared between four pixels. In this case each sensor detects 5 000 e^-, if the charge is shared equally, which is of the same order as the in-time threshold. This process is called
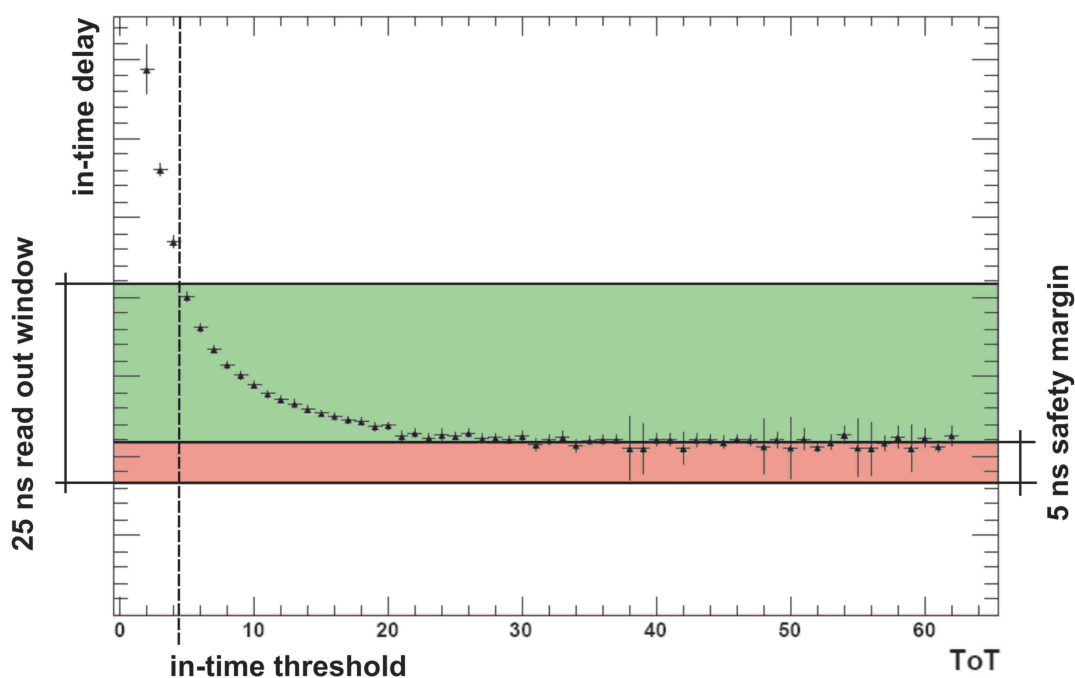
Figure 5.4: Delay setting of the in-time delay versus ToT. This measurement has been
performed in 2004 during the combined testbeam runs [TF06].

charge- or hit-sharing. For an irradiated pixel sensor the amount of charge, which a MIP
generates initially, is significantly smaller [Mo99].

In order to reconstruct the overall energy deposited during the particle passage, the shared
charge has to be summed again. This procedure is called clustering.

A misstimed module loses tracks with isolated hits of low ToT values (measured to about
0.2 % during the testbeam measurements in 2004 [TF06]), as explained in Section 5.1. It
is more likely, that hits with low ToT values (small deposited charges) are part of clusters.
For the testbeam measurements, that was the case for about 10 % of the tracks [TF06].
A distribution of the cluster sizes from reconstructed tracks in the pixel detector is shown
in Figure 5.5. The distribution is based on 20 394 events, simulated according to Section
7.1. For this simulated data approximately 28 % of the hits from reconstructed tracks in
the pixel detector are part of a cluster with more than three hits per cluster.

The threshold is determined by injecting a certain charge into the preamplifier of the
pixel cell (see Figure 4.13). The number of detected electrons in up to sixteen consecutive
LVL1A windows is counted many times and the detection efficiency is calculated. This
procedure is repeated for different charges and the hit probability is plotted against the
input charge. This efficiency curve is ideally a step function. Charge values below the
discriminator threshold are not detected, but above the threshold the detection proba-
bility ideally reaches 100 %. The step function is smeared by thermal noise and shows
an S-curve shaped profile. This distribution is fitted by a convolution of a step- and a
Gaussian function. The charge value at 50 % efficiency is the adjusted threshold value.
By calibrating the TDAC and GDAC (see Section 4.4.2) settings, the threshold can be
tuned to a value of approximately 4 000 e$^-$ [ATLEl08].
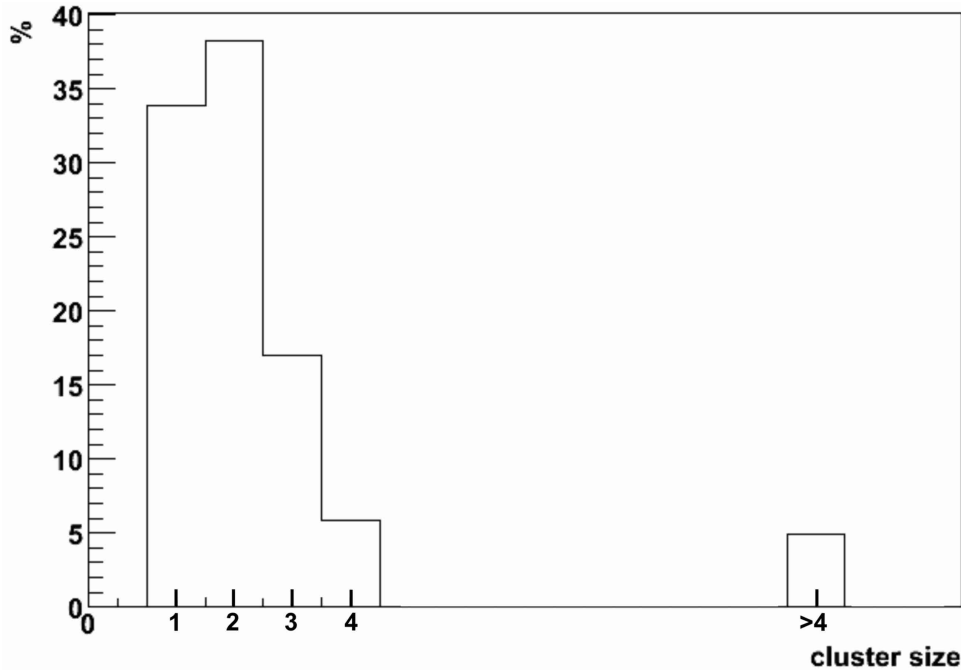
Figure 5.5: Distribution of cluster sizes from reconstructed tracks, generated from a datasample containing 20 394 events, 1 842 394 reconstructed tracks and 5 749 767 clusters.

The in-time threshold is determined after calibrating the timing and the threshold of the FE chip in a way, that high charge hits cross the discriminator threshold after 5 ns (this is done by adjusting the MCC strobe delay, see Section 4.4.3). Then a threshold scan is performed, with the difference, that only one LVL1A window is read out. Because of that the in-time threshold is usually 1 400 e^- larger than the discriminator threshold.

The difference between threshold and in-time threshold is called overdrive, which is an important parameter for the determination of the timing, as described in Section 7.2.

5.3 Clock Adjustments

The module clock is distributed by the Back of Crate Card (BOC), which is the first off-detector part of the data-distribution/readout chain of the pixel detector. Its position in the ATLAS system architecture is shown in Figure 4.10. Each BOC supports 26 modules of the pixel detector. The functionality of the BOC includes e.g.: Distribution of incoming clock signals from the TTC Interface Module (TIM), reception of control signals for the modules from the Read Out Drivers, distribution of the according Bi-Phase Mark (BPM) encoded signal to the Optoboards, and timing-, threshold-adjustment of the received optical data [TF06].

The tuning capabilities of the BOC comprise a finely adjustable delay for the BPM encoded module clock signal. A coarse delay in steps of 25 ns in a range of 0 ... 775 ns and a fine delay in steps of 280 ps in a range of 0 ... 35.56 ns is adjustable. It is therefore possible to tune the clock phase separately against the bunch crossing for each module [TF06].

6 ATLAS Offline Software

The ATLAS Offline Software provides tools for processing, reconstruction, and analysis of event data from the trigger and data acquisition systems of ATLAS. It also supplies the user with routines for Monte Carlo event generation and detector simulation. in order to serve the different requirements during the operational lifetime of ATLAS the structure of the software used has to be highly modular and flexible.

This flexibility is achieved by an object-oriented approach, using the C++ programming language, with some components based on FORTRAN and Java. Java refers to different software products and specifications, that provide a system for development of application software. An application, in the ATLAS offline software, is built from plug-compatible components, based on a diversity of configuration files. The embedding of the Offline Software into a framework, with common data processing standards, matches the requirements of the widely spread developer and user community of ATLAS. The common framework is called Athena framework and is described in Section 6.1 [ATLC05].

In the case of a complex detector like ATLAS a special software package for each of the hardware components is needed. Therefore, several domain decompositions were introduced:

- *Hardware domains*: Subdetectors of ATLAS, e.g.: Inner Detector, Liquid Argon Calorimeter, Tile Calorimeter, and Muon Spectrometer,

- *Software domains*: Software domains, which each of the detector subsystems has to provide are e.g.: Event generation, simulation, digitisation, reconstruction, physics analysis, calibration, and alignment processes [ATLC05].

The Athena software framework incorporates all of these basic data processing activities and combines them into a common structure.

6.1 The Athena Framework

The Athena framework is a common ATLAS-LHCb project and is an enhanced version of the Gaudi framework, which was developed for the LHCb experiment.

One of the underlying design principles is e.g. the use of abstract interfaces, that can be optimised to match different data stream and storage requirements. Additionally the manipulation of components sharing a common interface is supported. Furthermore data and algorithms are separated, e.g. the administration of transient data is done by a data class, while the processing, or generation of data objects, is handled by an algorithm class. Transient data is erased after the program has ended. Another major design principle is the distinction between data types and also between the data's lifetime, e.g. calibration, or alignment data has a significantly longer lifetime than event data.

An application using this framework is referred to as Job [ATLC05].

The major components of an application and their interactions are shown in Figure 6.1.
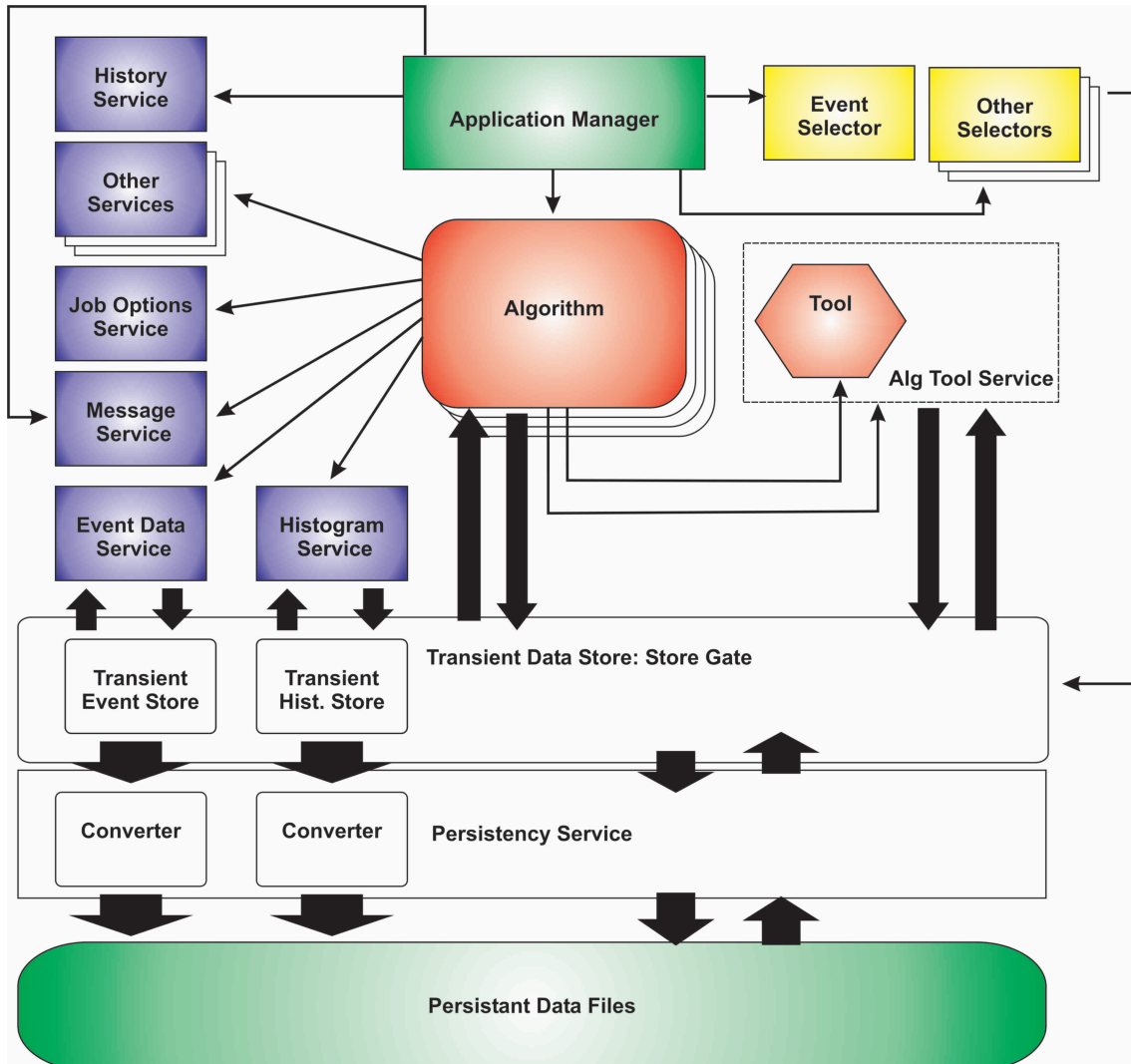
Figure 6.1: Athena components and interactions between them, according to [ATLC05].

- *Application Manager*: The Application Manager coordinates the activities of all components within an application.

- *Algorithm*: All algorithms included in one application share a common interface. An algorithm perfoms defined operations on each event and is called per definition only once per event. The algorithm itself can produce transient and persistent output data. Algorithms can be processed in sequence, so e.g. the input data can be filtered by one algorithm and processed by the following.

- *Tools, Alg Tool Service*: Tools, like algorithms, process input data and generate output data. The differences between tools and algorithms are, that tools can be called several times on one event and they do not share a common interface. Tools

can be owned by an algorithm, a service, or by the Alg Tool Service, which would be the default setting.

- *Services*: A service supplies the algorithm with defined operations, e.g. booking and import of histograms and n-tuples, where both transient (read/write) and persistent (read) datastore can be accessed. Services themselves can call other algorithms and can be linked to other services.

- *Transient Data Store*: The ATLAS Transient Data Store (TDS) is called StoreGate. It is the common memory of the algorithms, where data can be written and accessed. Once an object is posted to the TDS, the StoreGate takes ownership of the object and administers its lifetime and removal, according to the chosen presets. The TDS also converts transient to persistent data, using converters in the persistancy service. The StoreGate also provides an Application Program Interface (API) to access persistant data.

- *Event Selector*: The Event Selector selects the input events, that the application will process. Other selectors are used to choose objects within the TDS.

- *Converters*: Converters transform data from transient to persistent representations.

The StoreGate is designed to work with user type objects, which can be any Standard Template Library (STL) assignable. The user type object is stored as a data object in the StoreGate. The StoreGate defines an identifier for each data object (DO), so the user does not have to call the DO explicitly, it can be retrieved by the use of the unique identifier. The two components of the identifier are the type of the DO and the identifier of the algorithm instance, that produced the DO. So it is possible, that the TDS contains several instances of the same data produced by different algorithms and the user is able to distinguish them by means of their origin [ATLC05].

The services listed in Figure 6.1 are just exemples. The Job Option Service (JobOptionSvc) is a collection of modifiable algorithms, tools and other services. The History Service records the state of all services, tools, algorithms, run-time parameters and environment variables at the start of the Job. Also the type, class ID, and the exact store address of every object, which is written to the StoreGate, is recorded. The objects holding this information are called History Objects (HO). These objects are hierarchically linked, in a way that every data HO is connected to its generating algorithm HO and the Job HO. So each step in the generation of an object is comprehensible for the user [ATLC05].

Athena utilises Python scripts for the configuration and steering of algorithm, tool sets, and services, which process the event data. Python is an open source programming language featuring a multi-paradigm programming approach and a structure, which is reduced to an elementary syntax. The main Python control script is a user interface, which starts the Athena Application Manager and uses Python bindings to the core application sets. These Python bindings are collections of scripts that are based on a more abstract level of steering and are called JobOptions [ATLC05].

6.1.1 Event Simulation

As described in Chapter 6.1, the simulation of detector data is one of the main tasks of the Athena software framework, the corresponding simulation data flow is shown in Figure 6.2. The input for the simulation algorithms is produced in a Monte Carlo (MC) generator, in form of 4-vector classes, which are stored in the HepMC. The MCTruth information, separated by the Particle Filter, is directly processed by the simulation. MCTruth data contains the produced particle types, their exact tracks, and energy information. The simulation generates hit information from the MCTruth data. The hit information is then passed to the digitisation and transformed into Raw Data Objects, ready for reconstruction. The steps in event simulation are explained in detail below [ATLC05].
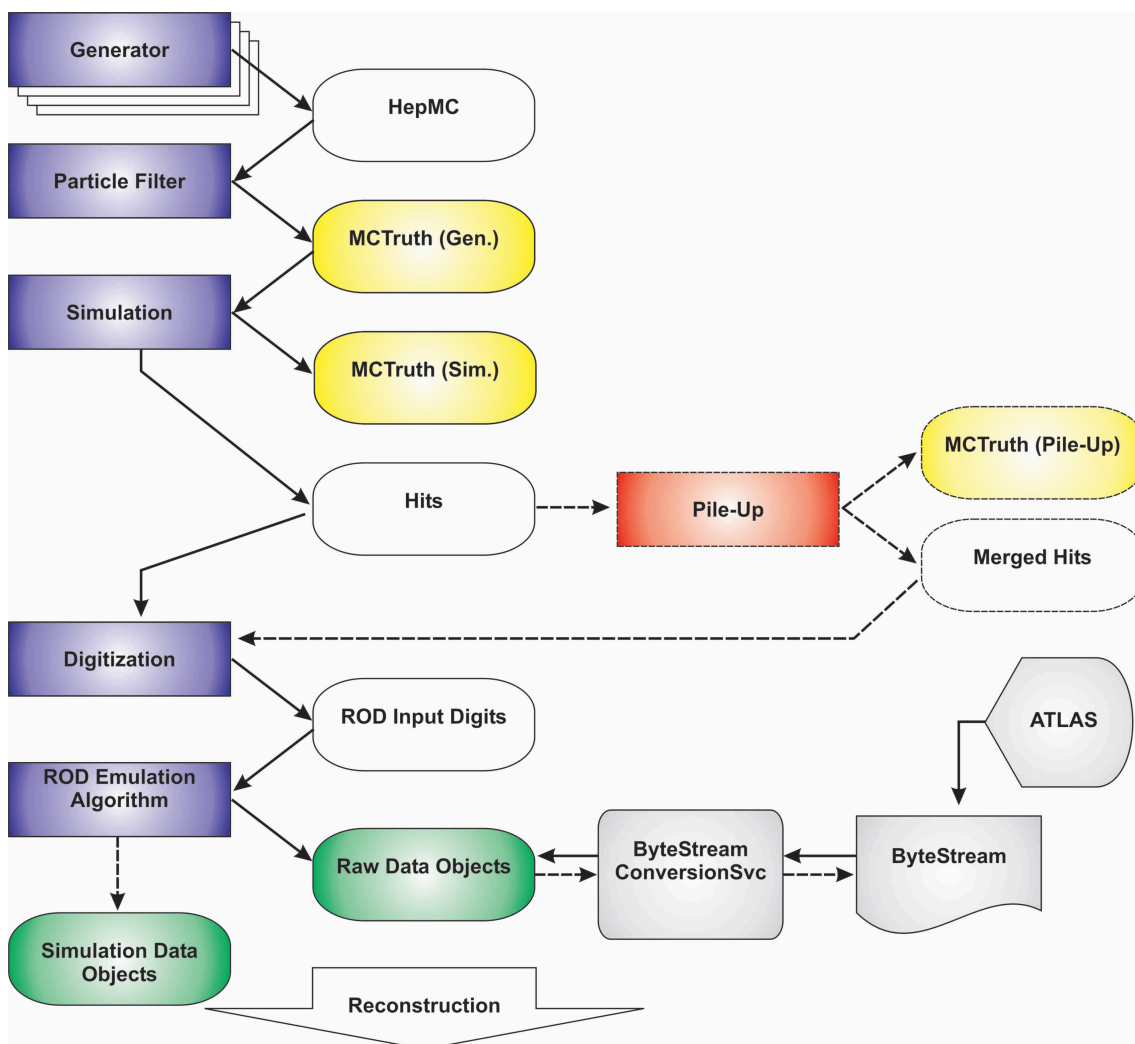
Figure 6.2: Simulation data flow according to [ATLC05]. Rectangles represent processing stages, rounded rectangles represent objects within the event data model. Dashed lines show optional stages.

Figure 6.2 shows the following items:

- *Generators*: Generators are tools for the modelling of physics processes. Generators are used for a wide range of tasks, e.g.: Modelling of hard, soft processes, initial and final state radiation, multiple interactions, and parton distributions. The output of the different generators is converted in a common format and a container, of the data produced, is placed in the TDS. A widely used generator is e.g. Pythia, which generates the hard process with two incoming and two outbound particles. A complete list of the available generators is given in [ATLC05].

- *Simulation*: The ATLAS simulation program Geant4 (G4) is based on the Geant3 simulation used for the preparation of the ATLAS Letter of Intent in 1992 [ATL92]. Geant4 provides solutions for, e.g.: Geometry and material description, passage of particles through matter, hadronic physics models, visualisation [ATLC05]. The output of G4 is a detailed description of real particle interactions. A more detailed overview of ATLAS G4 is found in [AR04].

- *Pile-Up*: The Pile-Up is an optional processing stage, it overlays the signal with additional proton interactions, cavern background and detector pile-up effects. The overlaid signals are called merged hits.

- *Digitisation*: The digitisation is the conversion of the hits produced by the G4 detector simulation, or by merged hits from the Pile-Up, into the detector output of ATLAS. This takes into account e.g. the charge propagation or the response of readout electronics separately for each subdetector.

- *ROD Emulation Algorithm*: ROD stands for Read Out Driver. The ROD emulation algorithm generates the ROD response to the simulated detector signals.

- *ByteStream*: The ByteStream is the persistent data format, which is the output of the detector high level trigger. ByteStream can be translated into the RDO format and vice versa.

The output of the digitisation stage are Raw Data Objects (RDO), which ideally match the form of real data from the detector. Also Simulation Data Objects (SDO) are produced, which contain information about the simulation. The SDO files are independent from the RDOs and navigation between SDO and RDO takes place, using identifiers. The digitisation is organised in packages for each subdetector and subsystem in which the individual settings (e.g. magnetic field, calibration values, noise level) are managed. These settings can originate from the JobOptions set by the user, or from the condition respectively the detector description database [ATLC05].

6.1.2 Reconstruction

The reconstruction is a composition of many different algorithms, which process the raw data information, necessary for physics analysis. This includes e.g. track information, missing transverse energy, position of the primary vertex, and particle identification. The data from all subdetectors is combined to ensure high precision processing over the full momentum and rapidity range of ATLAS.

Reconstruction algorithms use RDOs, previously reconstructed data from the TDS, or converted Byte Stream objects as input and utilise common tools for data processing. These tools are shared between the tracking and calorimeter subdetectors and feature shared interfaces for e.g. different types of track extrapolations, or energy reconstructions. The

output of a reconstruction algorithm is in general one collection of reconstructed objects, which can be e.g. a ROOT n-tuples, ESDs, or AODs.
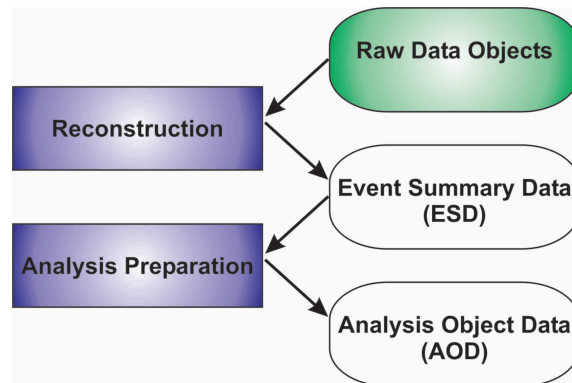
Figure 6.3: Reconstruction processing according to [ATLC05]. Rectangles represent processing stages, rounded rectangles represent objects within the event data model.

Figure 6.3 shows the following items:

- *Raw Data Object*: The RDO is a C++ object representation of the ByteStream information.

- *Event Summary Data*: The ESD includes detailed information of the detector reconstruction using approximately 500 kB disk space per event.

- *Analysis Preparation*: The Analysis Preparation reconstructs complex objects (e.g. b-tagging object JetTag) and reduces considerably the disk space, which is needed for the storage of an event.

- *Analysis Object Data*: The AOD is a summary of reconstructed event data needed for physics analysis. The disk space, which is used per event, is approximately 100 kB [ATLC05].

6.1.3 PythiaB

PythiaB provides an interface to the generator Pythia6. The location of the generator in the simulation chain of Athena is described in Section 6.1.1. PythiaB accelerates the generation of events containing b-quarks, by simulating only wanted decay channels. Optimal b-production parameters are set as default, but can be changed by the user. Furthermore, selection cuts can be applied, before and after the hadronisation process. After parton showering additionally, trigger and offline-like cuts can be assigned. PythiaB provides three basic mechanisms to produce b-quarks:

- *Flavour Creation*: $gg \rightarrow b\bar{b}$, $qq \rightarrow b\bar{b}$,

- *Flavour Excitation*: $gb \rightarrow gb$,

- *Gluon Splitting*: $g \rightarrow b\bar{b}$.

PythiaB interrupts the simulation before the hadronisation process and checks the generated events on the presence of a $b\bar{b}$ quark pair, within the user defined constraints on transverse momentum and η-range. Events not matching the defined requirements are discarded [MS05].

6.1.4 ATLFAST 2.0

As described in Section 6.1.1, the simulation of event data is a CPU-time consuming process. In order to create high event statistics in a short period of time, the ATLFAST package was developed for the Athena framework. It provides fast estimates for signals and background rates of specific channels. ATLFAST 2.0 is an independent package written in FORTRAN77 and is used for fast detector simulation, providing the most important detector aspects. To speed up simulation, not all detector effects are fully parameterised and only basic information about the detector geometry is used. Due to the fact that these limitations only affect the calorimeter simulation, the Inner Detector region is fully simulated. This makes ATLFAST 2.0 the suitable instrument for the simulation of large numbers of events for timing determination.

The main goal of the ATLFAST 2.0 package is the simulation and analysis of fully generated events including e.g.: Selection of isolated photons and leptons, jet reconstruction, labelling of b-, c- and τ- jets and the estimation of missing transverse energy [ERW98].

6.1.5 Conditions Database

The conditions database, or COOL (LCG Conditions Database Project) contains: Technical databases (detector production, installation and survey data), detector geometry, online/TDAQ databases, conditions databases (online and offline), event data, offline processing configuration and bookkeeping, distributed data management, and distributed database and data management services [ATLC05]. The conditions database can be accessed using Athena.

7 Timing Determination Using Offline Data

In this chapter the determination of the timing of the ATLAS pixel detector, using data from reconstructed events, is discussed. First the simulation and digitisation of the datasets used are described. Then the method of the timing determination and the discussion of the errors is presented, ending in the conclusion and outlook of this thesis. All histograms with continuous distributed entries comprise a binning including the lower and excluding the upper edge.

7.1 Simulation of Offline Data for Timing Studies

Two samples of event data are prepared, as described in Section 6.1.1 [KG08]. The first dataset contains 20 394 events with a timed detector and a second dataset contains 20 455 events, with the timing shifted by 15 ns, according to (7.1). Both data samples were not produced in a single step, each sample was generated in sets of 100 events per set. There are different numbers of events in each sample, because the number of events per produced dataset can vary slightly [KG08]. The events were generated using Athena production cache version 14.2.20.3, utilising the ATLFAST 2.0 simulation package and the Pythia6 generator. The PythiaB wrapper was used with default setting, to speed up the simulation. Geometry version ATLAS-GEO-02-01-00 was used in the simulation of the detector.

According to Section 5.1, shifts in the clock phase result in the assignment of a hit to a wrong bunch crossing, consequently a wrong LVL1A bin in the readout window. Following the simulation data flow of Figure 6.2, the Athena simulation produces Monte Carlo hit data, which are used as input for the digitisation. The digitisation simulates the detector response to the generated events. The LVL1A bin to which a hit is assigned, is created during digitisation. The parameter BCID (Bunch Crossing Identity) has to be adjusted. The BCID holds the number of the LVL1A bin the corresponding hit is assigned to. The following description of the digitisation only refers to the digitisation for the pixel detector and is based on the C++ source code of the Athena digitisation package, which is found on [ALXR].
The steps in the generation of charge and timing information are the following [LXR01]:

1. *Generation of Surface Charge*: According to the G4-simulated hit information the charge in the pixel cell is generated.

2. *Calculation of Crosstalk*: If a hit generates a charge greater than three times the discriminator threshold, the crosstalk between neighbouring pixels is calculated and added to the charge value from step one. The crosstalk depends on the length of the common border of two adjacent pixels.

3. *Simulation of Thermal Noise*: Thermal noise is simulated by variation of the charge according to a Gaussian distribution with a width of 200 e^-.

4. *Addition of Random Noise*: Noise is added randomly to pixel cells, independently of the fact that some cells have not been hit.

5. *Merging of Ganged Pixels*: The charge depositions from pixel cells, which share a common readout cell (ganged pixels), are merged.

6. *Treatment of Special Pixels*: A mask of special pixels derived from the conditions database is applied. According to the mask, the different behaviour of spexial pixels is taken into account for the charge variation in this step. Pixels are referred to as 'special', if they are noisy or have a disconnected bump bond, are unusable or dead for unknown reason, are disabled, or provide corrupt ToT information. The special pixel map was created during the production tests and includes the differences in the charge collection efficiency, which depend on the type of bump-bonding, used in the pixel cell (described in Section 4.4.2). The calculated charge variation, due to the behaviour of the special pixel, is added to the charge from steps one to five.

7. *Simulation of the Discriminator Response*: The discriminator response is simulated for each pixel cell. The BCID (= LVL1A bin) of the hit and ToT information according to the charge from steps one to six are calculated .

The BCID generation in step seven is achieved by a function in the digitisation of the Athena software framework, which is called `PixelTimeWalkGenerator::relativeBunch()` [LXR01]. The input parameters of this function are the threshold, the in-time threshold value of the corresponding pixel cell and the total charge according to steps one to six. The threshold values are taken from the conditions database (see Section 6.1.5). If no database connection is available, default values are used: $4\,100\ e^-$ for the regular threshold and $5\,400\ e^-$ for the in-time threshold [LXR01].

In the function `PixelTimeWalkGenerator::relativeBunch()`, the timewalk t_{tw} is calculated, using the parameterisation shown in (5.2). To this timewalk value a variation of the initial value is added. The variation is calculated by generating a factor σ_g from a random generator, following a Gaussian distribution, with a mean value of 0 and a sigma of 1. The factor from the random generator is then multiplied by $0.2\ t_{tw}$. This creates the effective timewalk $t_{etw} = t_{tw} + 0.2\ t_{tw}\ \sigma_g$.

The timing information is generated by adding the effective timewalk t_{etw}, the time at which the particle crossed the sensor (`TimeZero`), the G4 time, and random jitter. By default, the jitter value is set to zero. If e.g. data from cosmic particles is digitised, the jitter follows a flat distribution from $-12.5\ldots 12.5$ ns, because it is not known if a particle crosses the detector at the beginning or at the end of a LV1A bin. From this timing information the simulated computing time t_{comp} is substracted. The BCID is then computed by dividing this value by the time between two bunch crossings (25 ns default) and rounding the result to the next smallest integer value [LXR02]:

$$BCID = \frac{1}{25\ \text{ns}} \cdot (t_{etw} + t_{t0} + t_{G4} + t_{jit} - t_{comp} + t_{off})\,. \tag{7.1}$$

By adding an offset parameter t_{off} to the timing information, a known clock phase is added to all digitised hits (7.1). The clock phase for all hits of the second RDO sample used in the timing analysis presented is set to $t_{off} = 15$ ns.

7.2 Timing Studies

This section describes the access to the simulated event data on RDO level using the Athena software framework and how to extract the timing information. The method chosen for the analysis is called the LVL1A fit method. It utilises the fit of a finely-binned delay distribution (bin width < 1 ns), generated using (5.2), to the LVL1A distribution as it is simulated using the real detector response (bin width 25 ns). This allows to determine the time between the beginning of the readout window and the arrival of the fastest hits. The finely-binned distribution is generated by taking into account only the timewalk of the input charges, which are calculated from the ToT distribution for each FE chip. In detail this method and the corresponding error analysis are shown in Section 7.4.

Extraction and analysis of the timing related data are separated. The data extraction is achieved using a self-developed algorithm, which utilises the Athena software framework. The analysis is implemented as a stand-alone C++ program, which relies on ROOT libraries. The analysis program is based on the ROOT macro used in [MK08].

7.2.1 Access to Timing Information

The data needed for the LVL1A fit method is accessed during the reconstruction of the Athena software framework and will also be available once the ATLAS detector produces real data. An algorithm was appended to a reconstruction sequence, to extract the data needed to determine the timing of the ATLAS pixel detector. Only particle tracks in the Inner Detector (pixel detector, SCT, TRT) region are reconstructed. The reconstruction of objects like the calorimetry and muon chambers is switched off to minimise the computing time. On an Intel XEON Quadcore processor with 1.8 GHz an RDO with 100 events is processed in approximately 28 minutes.

Timing Related Data

In order to create a pure data sample with a small amount of noise, only hits from reconstructed tracks are taken into account for the analysis. Therefore, the `ExtendedTracks` container is used to mark those hits in the TDS, which are part of reconstructed tracks. Then the `PixelRDOs` container is used to extract the data of these hits for the LVL1A fit method. The TDS identifier, pointing to hit information on pixel level, is called rdoID. The rdoID is used to find the marked hits of the `ExtendedTracks` in the `PixelRDOs` container. The `NewTracking` algorithm was utilised to reconstruct tracks [AS07].

The `ExtendedTracks` container comprises pointers to all necessary track parameters. The `PixelRDOs` container contains a summary of all hit data from the pixel detector.

Two kinds of input data are needed for the timing analysis: hit information and calibration data from the pixel detector. The hit information includes:

- The position of the hit in the pixel detector, which is given by detector element, layer, module position and FE number.

- The pixel type. Different pixel types are combined into three groups: Group one includes normal pixel, group two includes ganged-, long-ganged and long-interganged pixels and group three comprises long pixels. To extract the pixel type, the row and the column of the hit on the FE have to be known.

- The ToT value and the LVL1A bin of the hit.

The calibration data is available for every FE chip, separately for each of the three pixel type groups:

- The calibration parameters A, C and E according to (5.1).

- The threshold and in-time threshold values for timewalk calculation according to (5.2), (5.3) and (5.4).

Hit related data is extracted on three levels, the track, cluster, and pixel level. Data on the track level is only used for the investigation of differences in the simulated RDO datasets and is not relevant for the LVL1A fit method. Data on cluster level was used to determine the differences in the ToT and LVL1A distributions, if hit-sharing is compensated by the addition of simultaneous low charge hits in adjacent pixels (clustering). Data on cluster level is not used in this thesis, but is needed, if the timing of the ATLAS pixel detector is determined based on data of cosmic particles [MP08].

Data on pixel level is used in this thesis. 'Pixel level' means, that for this data no clustering is applied. It was necessary to use data on pixel level, because clusters can contain more then one pixel type. This has a negative influence on the timing determination, because the calibration parameters, used in the LVL1A fit method, are different for each pixel type. As a consequence of the summation of the charges of the pixels contained in a cluster, the LVL1A and ToT values on cluster level are different from those on pixel level. Without the compensation for charge sharing (pixel level), the Landau shaped charge response behaviour of the pixel sensors (described in chapter 2.4.1) cannot be observed.

The described differences in the distribution of ToT values are shown in Figure 7.1. On pixel level, the Landau shaped distribution, with a most probably value (mpv) of approximately a ToT of 30, is overlaid with a distribution with a dominant peak at values of a ToT of roughly 6. The mpv of a ToT value of approximately 30 can be explained by taking into account the mpv of generated charge of a MIP of roughly $20\,000\ e^-$ (see Section 4.4.1) and the charge/ToT conversion, shown in Figure 5.2.

As described in Section 5.1 the timewalk effect increases for small charge values in the pixel sensor. Therefore, small charge depositions are detected later. This effect is observed in Figure 7.2, where approximately 5 % of the hits from LVL1A bin one are shifted to LVL1A bin two, by breaking up clusters into single pixel hits. In Figures 7.1 and 7.2 the bin entries have been normalised to the number of entries in the whole distribution, $5\,749\,767$ hits on cluster and $9\,027\,347$ hits on pixel level.
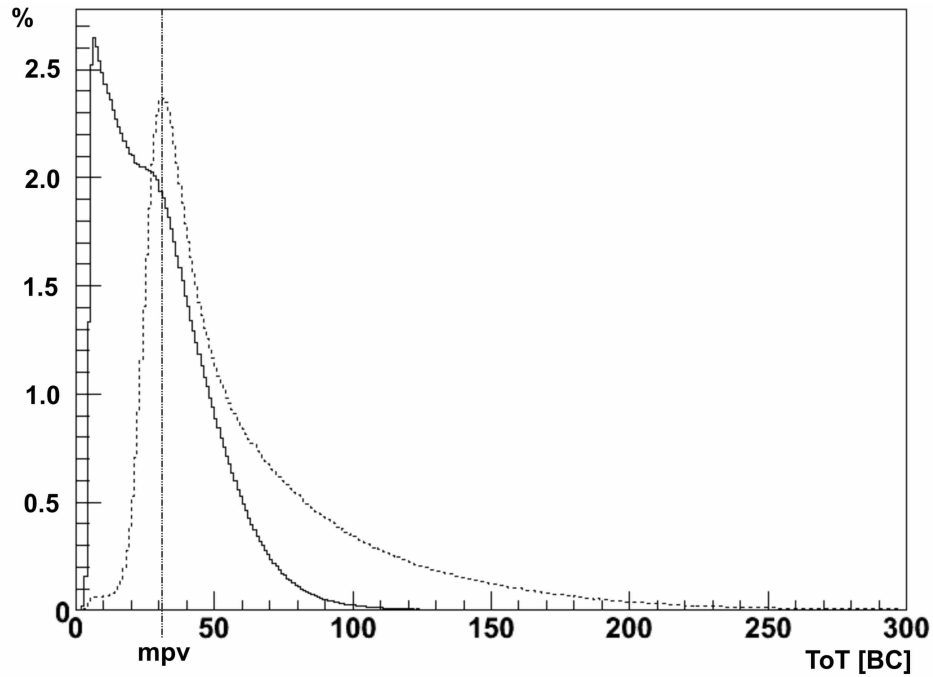
Figure 7.1: ToT value distribution of hits from reconstructed tracks in bunch crossings [BC] = 25 ns, for values on cluster (dashed line) and pixel level (solid line), normalised to 5 749 767 entries on cluster and 9 027 347 entries on pixel level.
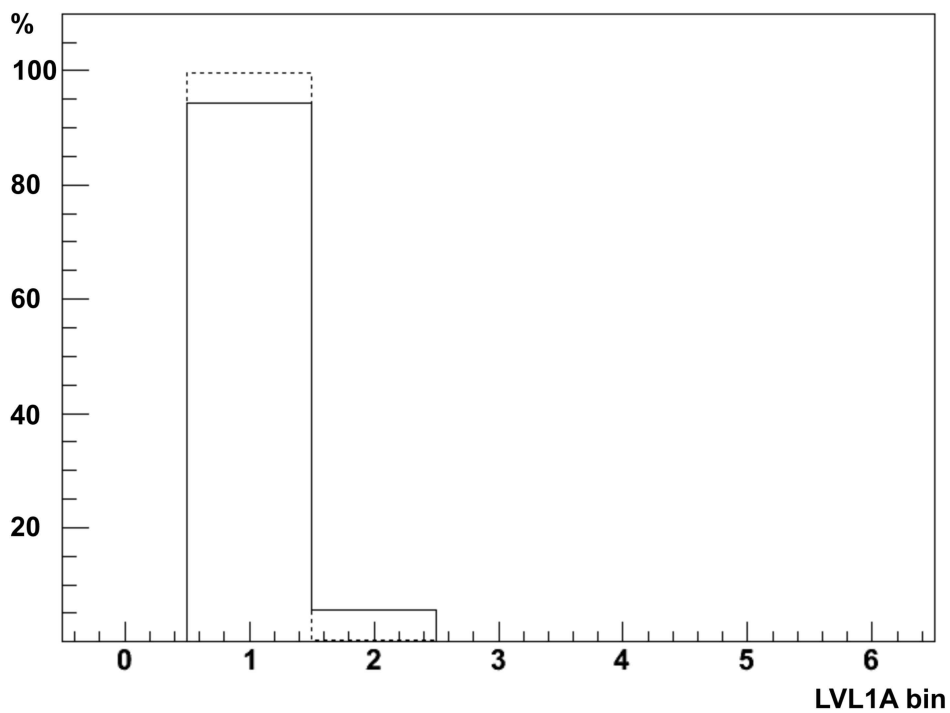
Figure 7.2: LVL1A distribution of hits from reconstructed tracks, for values on cluster (dashed line) and pixel level (solid line), normalised to 5 749 767 entries on cluster and 9 027 347 entries on pixel level.

Data Extraction Using Athena

The Athena based extraction algorithm (EA) writes the data into ROOT n-tuples, one n-tuple with the timing information, containing data on track, cluster, and pixel level and another one with calibration data. The EA processes data from the TDS, which is held in two containers, which are created during the reconstruction of hit data. These containers are called `ExtendedTracks` and `PixelRDOs`. The `ExtendedTracks` container comprises not only data from the pixel detector, but also TRT and SCT track information. The structure of the EA is shown in Figure 7.3.
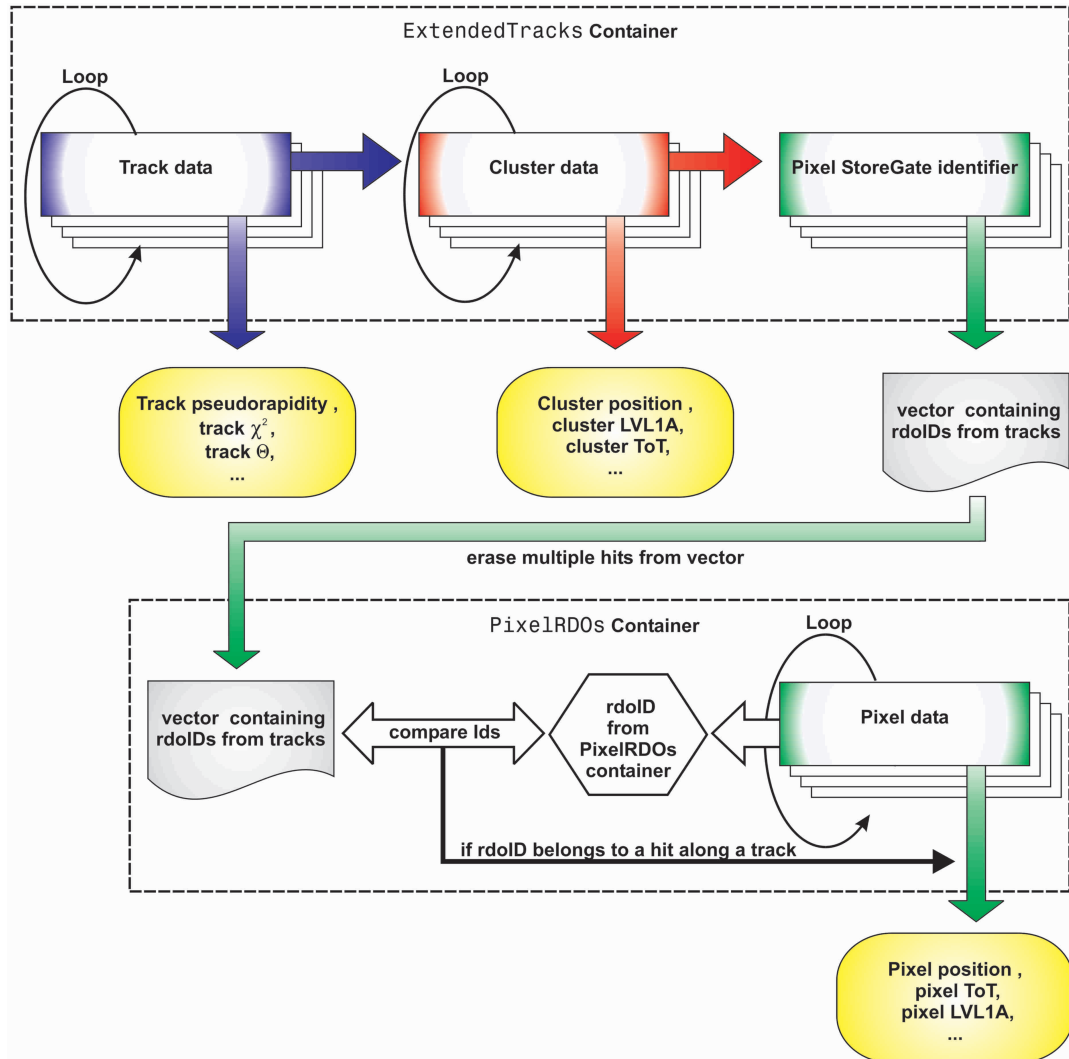
Figure 7.3: Structure of the EA. Dashed lines comprise the content of a specific container and rounded rectangles represent persistent data.

The EA loops over the individual reconstructed track data of an input event. Pointers to this data are held in the `ExtendedTracks` container. In this loop data on track level, for each reconstructed track, is written to the n-tuple which contains timing data. For each individual track a second loop, over the pixel clusters, through which the track traverses, is processed. During this loop data on cluster level is written to the n-tuple containing timing information. This second loop over the cluster also grants access to the rdoID,

which points to the transient data of the individual pixels, which each cluster comprises. The rdoID is written to a vector for further use.

The identifiers from this vector are then compared to those found in the `PixelRDOs` container, which holds pointers to hit data on pixel level. If the comparison confirms, that an rdoID is also found in the `ExtendedTracks` container, the data according to this StoreGate identifier is written to a ROOT n-tuple.

If the geometrical track density is high, a cluster can be assigned to up to four different tracks. In order to prevent a statistical bias caused by multiple processing of certain hits, the contents of the vector are filtered, so that each identifier is only contained once.

The information, which is extracted for each event using the `ExtendedTracks` container, is listed below.

- *Track Level*: Longitudinal impact parameter, azimuthal and zenith angle of the track, track pseudorapidity η, track χ^2 divided by the number of degrees of freedom.

- *Cluster Level*: Cluster size, cluster ToT and LVL1A value, cluster position.

- *Pixel Level*: TDS identifier (rdoID) of the pixels composing the clusters.

Using the `PixelRDOs` container the following data is collected:

- *Pixel Level*: Pixel type, pixel hit position, pixel ToT and LVL1A value.

7.2.2 Module Coordinate System

The coordinate system used for the pixel modules is different from the ATLAS coordinate system introduced in Section 4. The position of cluster and pixel hits is identified by the detector element of the pixel detector, the layer, the values of ϕ_{mod} and η_{mod} for the module, and the FE number.

The detector element can be end-cap A (ECA), end-cap C (ECC) or barrel. Each detector element has three layers. The ϕ_{mod} position is the number of the stave for barrel modules and the number of the end-cap modules. This number starts at zero and is increased clockwise from the uppermost stave. For the end-caps the ϕ_{mod} position varies between $0 \ldots 47$ and for the barrel it depends on the layer, for the b-layer it is $0 \ldots 21$, for layer one $0 \ldots 37$ and for layer two $0 \ldots 51$.

The module η_{mod} position is an integer number between $-6 \ldots 0 \ldots 6$. Each stave carries thirteen modules, which are numbered starting from -6 (pointing to ECC). In Figure 7.4 the coordinates are shown for e.g. barrel layer two of the pixel detector.

The hit positions for a barrel layer are recorded by FE number according to the following assignments:

$$
\phi_{mod} \rightarrow \begin{matrix} \text{FE} > 7: & 2\,\phi_{mod} + 1 = \phi_{fe}, \\ \text{FE} < 8: & 2\,\phi_{mod} = \phi_{fe}, \end{matrix} \tag{7.2}
$$

$$\eta_{mod} \quad \rightarrow \quad \begin{array}{l} \text{FE} \; > \; 7 : \quad \eta_{mod} \; 8 + \text{FE} - 8 = \eta_{fe}, \\ \text{FE} \; < \; 8 : \quad \eta_{mod} \; 8 - \text{FE} + 7 = \eta_{fe}, \end{array} \qquad (7.3)$$

with FE as the front end number on the pixel module. The value η_{mod} denotes the position of the module along the stave.
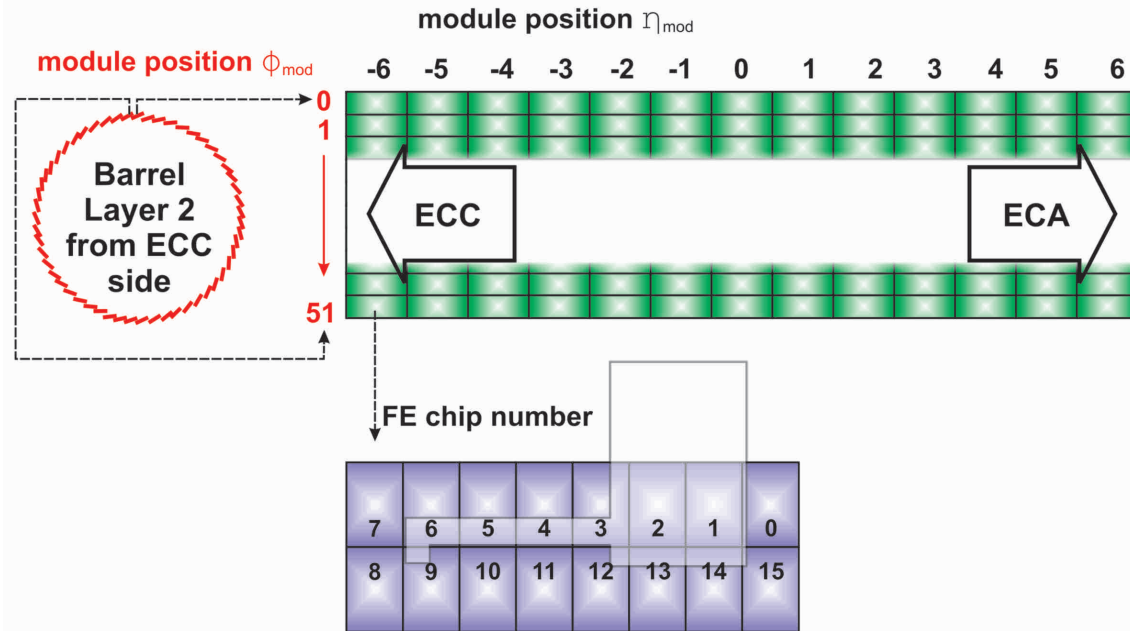
Figure 7.4: Module coordinates used by the extraction algorithm for e.g. barrel layer two of the ATLAS pixel detector.

7.3 Differences due to the Shift of the Timing Offset

As described in Section 7.1 two RDO datasets were simulated as input for the timing analysis. The first dataset was simulated with a timed detector ($t_{off} = 0$ ns). The second dataset features a shift in the BCID generation of $t_{off} = 15$ ns, as described by (7.1). Due to the fact that six LVL1A bins are used for the reconstruction, the shift in the BCID generation does not affect the cluster or track finding algorithms. The data of hits with a low ToT value appears in the wrong LVL1A bin, but the information of the hit is still available.

The negative effects, due to the shifted timing offset are only perceivable if the number of readout LVL1A bins is reduced. Only then hit information is lost. The investigation of the influence of a detector with a shifted timing offset on the reconstruction algorithms lies beyond the scope of this thesis and will be subject of future studies.

The differences in the BCID assignment between a detector with optimal and shifted timing offset are observed in the ToT distributions associated with a single LVL1A bin. This is shown in Figure 7.5 for the detector without timing offset and Figure 7.6 for the detector with an applied timing offset. In Figure 7.5, 94 % of all entries in the b-layer of the

ATLAS pixel detector lie in LVL1A bin one and 5.6 % of all entries lie in LVL1A bin two. Only a fraction of entries are found in bin three. The entries tagged with LVL1A bin two are distributed around a value of ToT = 6. This changes if the timing offset is applied. In Figure 7.6 75 % of all entries are in LVL1A bin one, 23 % of all entries in LVL1A bin two and 2 % of all entries in LVL1A bin three. This shows, that for an applied timing offset of $t_{off} = 15$ ns large numbers of hits with low ToT values are shifted to higher LVL1A bins.
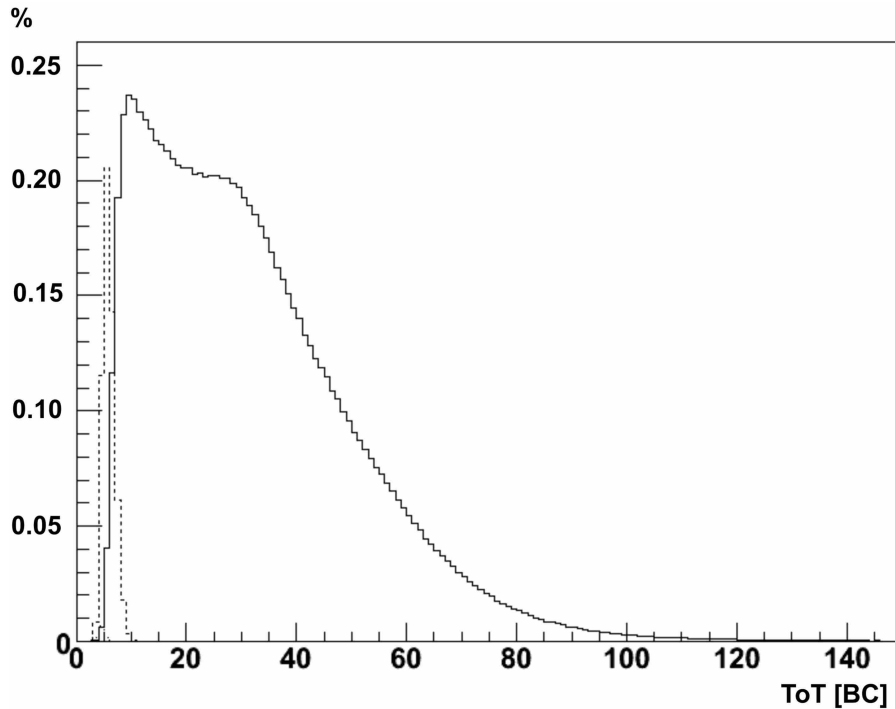
Figure 7.5: ToT distribution for LVL1A bin 1 (solid line) and LVL1A bin 2 (dashed line) in units of bunch crossings ([BC] = 25 ns), normalised to 3 592 086 entries for the ATLAS pixel detector without timing offset and the b-layer.

Both RDO datasamples show an azimuthal dependence of the hit occupancy on cluster and pixel level. Due to a misplaced beamspot in the Inner Detector some modules show a higher hit occupancy in ϕ-direction, because they are closer to the beamspot [AtA08]. The azimuthal dependence is not found in the distribution of the track azimuthal angle ϕ_0, because the point of origin for the tracks is the displaced beamspot. The distribution of the ϕ_0 values of the reconstructed tracks is shown in Figure 7.8.

The observed azimuthal dependence was found to be the same for both detector timing settings, on cluster and pixel level. According to the coordinate conversions in (7.2) and (7.3) the occupancy maps were created separately for the three barrel layers of the ATLAS pixel detector. The map for the b-layer (Figure 7.7) shows significant fluctuations in the hit occupancy in ϕ-direction. In Figure 7.7, the normalised hit occupancy is projected into the ϕ-plane. The observed anisotropy has no effect on the quality of the timing determination.
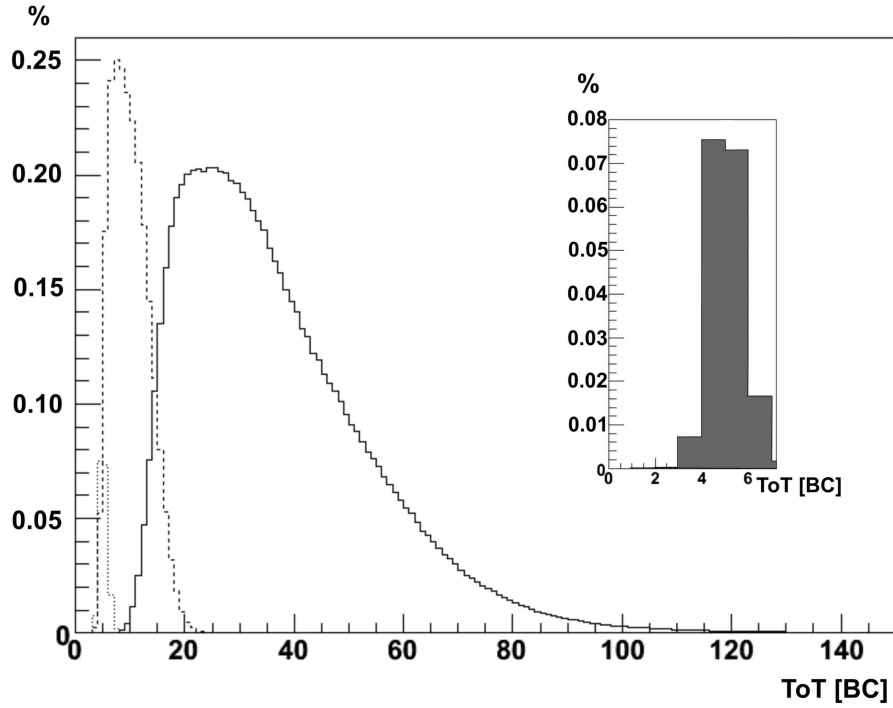
Figure 7.6: ToT distribution for LVL1A bin 1 (solid line), LVL1A bin 2 (dashed line), and LVL1A bin 3 (grey filled region in the inserted histogram), in units of bunch crossings ([BC] = 25 ns) normalised to 3 591 608 entries in b-layer and the ATLAS pixel detector with an applied timing offset of 15 ns.
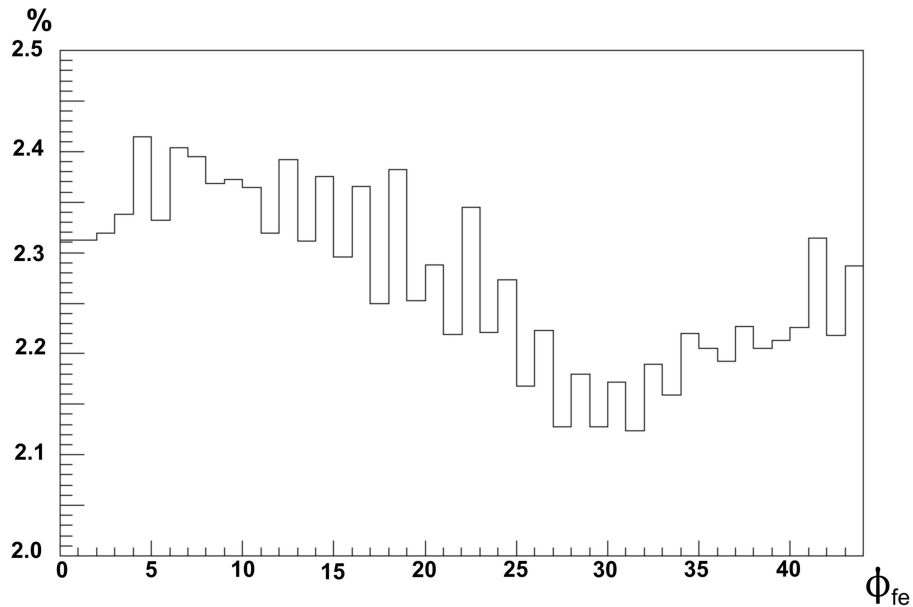
Figure 7.7: Hit occupancy on pixel level for the b-layer, as a projection into the ϕ_{fe} plane, normalised to 3 592 086 entries for the ATLAS pixel detector without shifted timing offset. The coordinates ϕ_{fe} are given according to (7.2) and (7.3).
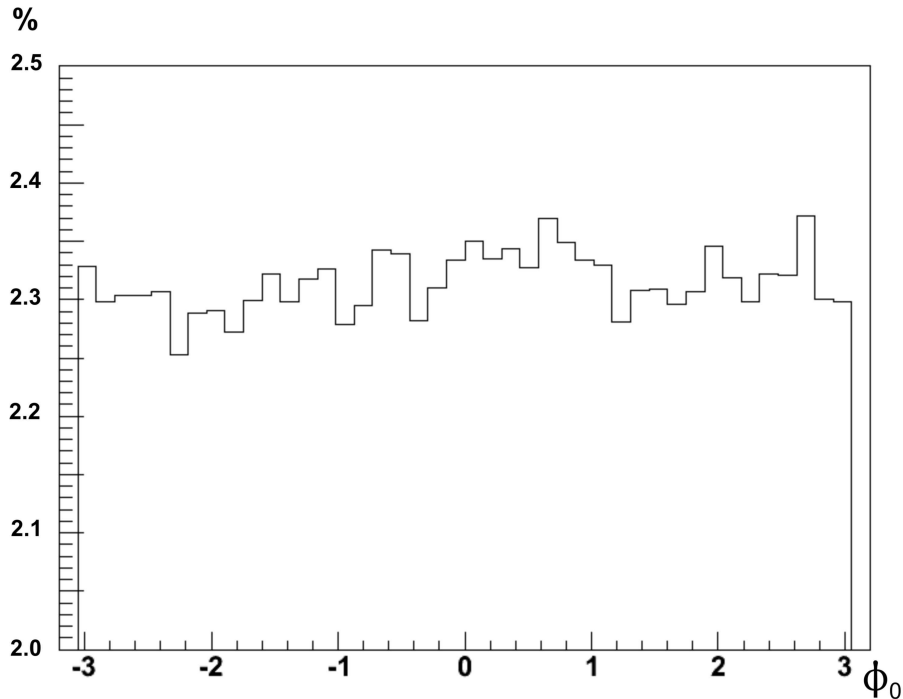
Figure 7.8: Distribution of the azimuthal angle ϕ_0 (in rad) of reconstructed tracks in the pixel detector, normalised to $1\,842\,394$ tracks.

7.4 LVL1A Fit Method

The method chosen to determine the time between the beginning of the readout window and the arrival time of the fastest hits t_d is the LVL1A fit method. As outlined in the beginning of Section 7.2, this method utilises a fit of a finely-binned (bin width < 1 ns) delay distribution to a coarsely-binned (bin width = 25 ns) LVL1A distribution. The coarsely-binned LVL1A distribution is created from the data, which the Extraction Algorithm (EA) provides by processing simulated events. This distribution is referred to as 'measured' LVL1A distribution, because it is the result of the simulated detector response. The finely-binned distribution is referred to as 'simulated' delay distribution, because it is generated outside the Athena framework, using an stand-alone C++ macro.

All distributions shown in this section comprise data from single FE chips. The LVL1A fit method is also performed on data collected by single FE chips. It is possible to perform this fit method on whole pixel modules, or sections of the pixel detector. The FE chip based approach was chosen, because the calibration parameters needed for the timing analysis are available for each FE chip separately. In this way an accurate timing analysis can be performed for each FE chip and the pixel module timing can be derived from the mean value of the timing of the FE chips, that are contained in the module.

The LVL1A distribution shows the number of detected hits as a function of the readout clock windows. The timewalk effect causes a spread of the measured hits over up to three

different bunch crossings, depending on the charge generated in the pixel sensor. The points in time, at which signals from high charge hits cross the discriminator threshold and appear in the chosen readout window, define the shape of the measured LVL1A distribution. Hence the measured LVL1A distribution is used to determine t_d with a resolution better then 25 ns. In the measured LVL1A distributions up to sixteen LVL1A bins can be recorded in a readout window, this is achieved by repeating the LVL1A trigger signal in the MCC. In this thesis the readout window has a length of six LVL1A bins (150 ns). Figure 7.9 shows the measured LVL1A distribution for the detector without shifted timing offset (solid line) and with timing offset (dashed line). The distributions show, that, due to the applied timing offset, a significant number of hits is shifted from LVL1A bin one to bin two.
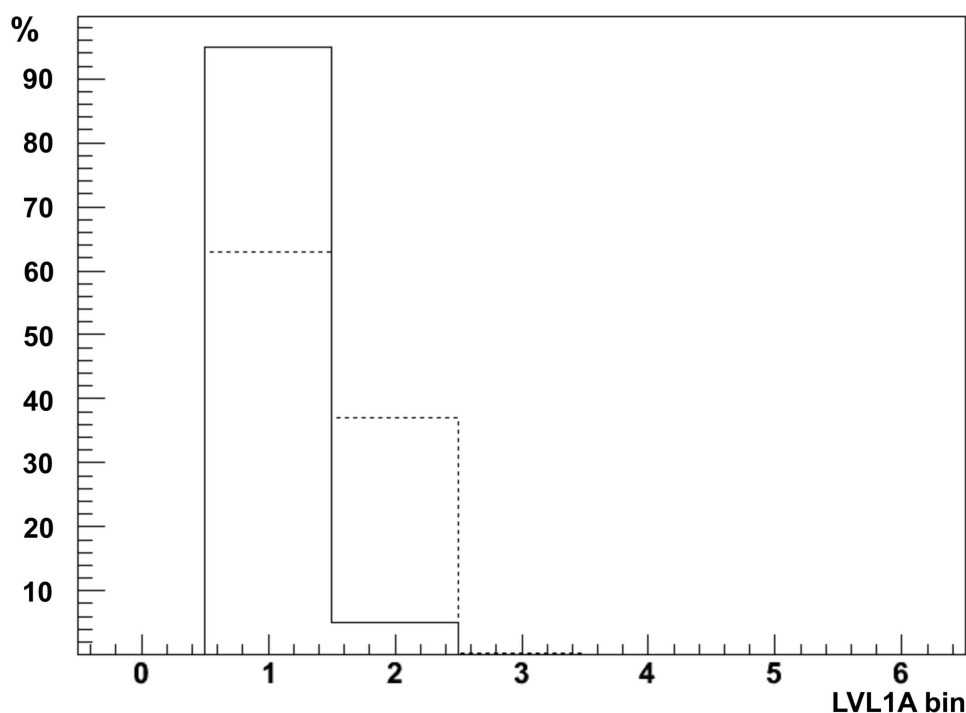
Figure 7.9: LVL1A distribution for one FE-chip without shifted timing offset (solid line) normalised to 440 hits and with applied timing offset (dashed line) normalised to 572 hits. Position: $\eta_{mod} = -1$, $\phi_{mod} = 1$, FE chip number 13 in the b-layer.

7.4.1 Selection of Input Data

The analysis described here can be performed on any module of the pixel detector. In this thesis the studies were performed in detail on ten modules, which are located in the b-layer of the ATLAS pixel detector. The modules were chosen using the following procedure:

The modules are selected from three occupancy ranges, before the preparation of the input data described in Section 7.4.2 was applied:

1. $0 - 500$ hits in average per FE chip,

2. $500 - 1\,000$ hits in average per FE chip,

3. $1000 - \infty$ hits in average per FE chip.

From these ranges the ten modules with the highest hit occupancies were chosen. On the data of these modules the LVL1A fit method was performed. The module timing determination is assumed to be stable if the LVL1A fit of at least nine of sixteen FE chips showed a $\chi^2 < 1\,000$.

The hit occupancies of the modules in occupancy range one, proved to be too low for a stable application of the LVL1A fit method, the fits of all modules were unstable ($\chi^2 > 1000$). In range two four of ten modules were discarded as unstable, three modules showed an average χ^2 of approximately $\chi^2 = 270$. Three modules showed stable results. The modules of range two, for which the LVL1A fit method succeeded all had an average hit occupancy of roughly 980 hits per FE chip. For range three no module was discarded.

This leads to the assumption, that before the input data is prepared for further analysis a module should at least have an average hit occupancy of 1000 hits per FE chip in order to obtain stable results from the LVL1A fit. Therefore, all modules from range three are suited for the analysis. In order to save time only ten modules with highest hit occupancies have been selected for further analysis.

7.4.2 Preparation of Input Data

This analysis utilises FE based LVL1A distributions of both generated RDO samples and the according calibration parameters as input data. The hits, which are finally used for the timing analysis, are selected from the measured ToT distribution for each FE chip. The ToT values of the chosen hits follow a uniform distribution in a range of ToT $= 6 \ldots 27$ BC. The uniform shape is chosen for the sake of simplicity and because the shape of the ToT distribution has to be known, in order to match the simulated ToT distribution precisely to the measured ToT distribution.

The upper limit of the uniform distribution was chosen, because the timewalk decreases exponentially with increasing ToT values (5.2). Consequently, higher ToT values are unlikely to be shifted to a higher LVL1A bin, due to timewalk. The lower limit was chosen, because the ToT calibration function (5.1) shows deviations from the measured distribution for charge values smaller than $5\,000$ e$^-$, which corresponds roughly to a ToT value of 6 BC [MK08].

The values for the uniform ToT distribution are chosen as described in the following itemisation:

- Find the bin in the range of ToT $= 6 \ldots 27$ BC with the lowest number of entries n_{low},

- Select randomly a number of n_{low} hits of each of the other bins in the chosen range,

- Fill the ToT values of the selected hits in one histogram and the corresponding LVL1A values in another one, Figure 7.11.

The number of entries per bin depends on the number of hits in the FE chip. An exemplary initial ToT distribution of one FE chip is shown in Figure 7.10. From this ToT distribution 616 entries in the described ToT range are selected as input for the timing analysis. The ToT distribution of selected hits and the corresponding LVL1A distribution

are shown in Figure 7.11.
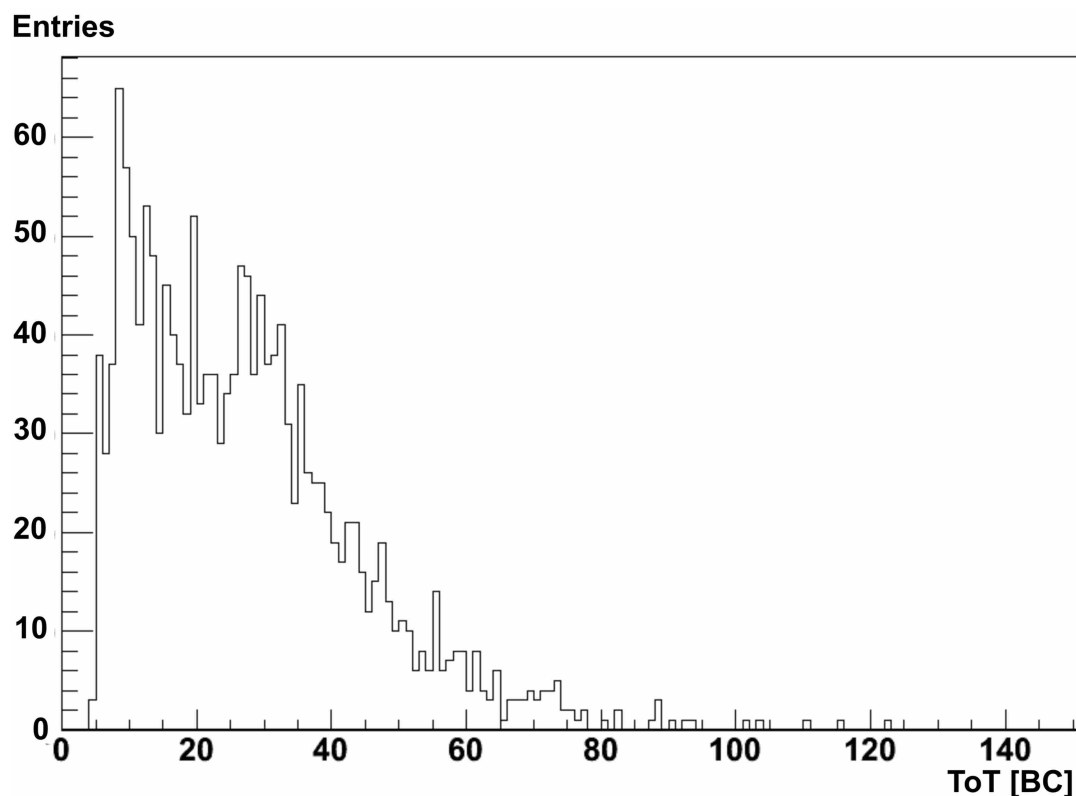
Figure 7.10: ToT distribution created from data on pixel level for reconstructed tracks, 1 660 entries for the ATLAS pixel detector without timing offset.

The described input data selection is performed, because it is necessary to match the shape of the finely-binned simulated delay distribution to the shape of the measured LVL1A distribution. In order to increase statistics in the chosen data sample, it is possible to select the hit data according to other distribution shapes. The uniform distribution is used for the sake of simplicity. Another approach would be the use of all available hit data. However, this complicates the simulation of the finely-binned delay distribution, because the shape of the underlying ToT distribution is not exactly known as was pointed out in Section 7.2.1.

7.4.3 Generation of the Simulated Delay Distribution

Instead of directly simulating a finely-binned delay distribution, a ToT distribution is generated. This is done in order to comprehend the charge/ToT conversion characteristics, which are different for each FE chip [MK08]. This ToT distribution matches the constraints described in Section 7.4.2. The simulated range is chosen to be $ToT = 5.5 \ldots 27.5$ BC, because hits with measured $ToT = n \pm 0.5$ BC are assumed to be assigned to $ToT = n$, by the discriminator of the analogue part of the pixel cell. In order to smoothen the spectrum, the number of simulated ToT values is fifty times larger than the number of
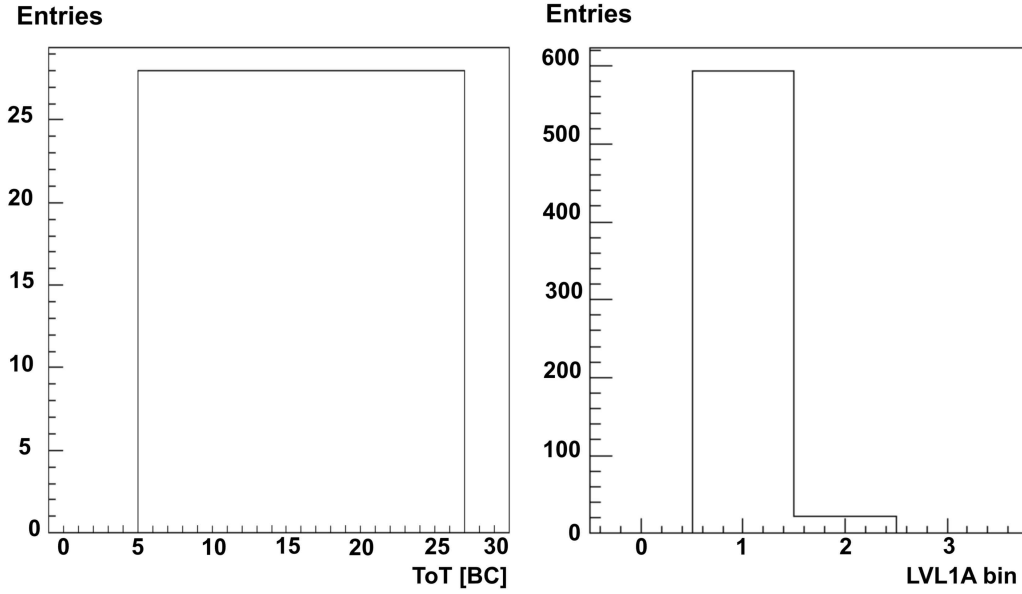
Figure 7.11: ToT (left) and LVL1A (right) distribution of 616 selected hits from Figure 7.10 of the ATLAS pixel detector without applied timing offset.

selected hits from the input data set. The number of entries per bin is then scaled down to match the initial number of entries of the selected data. An exemplary ToT distribution is shown in figure 7.12. The simulated ToT values are converted into delay $d\,(ToT)$ values by:

$$d\,(ToT) = \frac{P_0}{\left(\frac{A\ E - ToT\ C}{ToT - A} - P_1\right)^{2.5}}\ ,\tag{7.4}$$

according to (5.2) and (5.1). The calibration parameters A, C, and E are derived for every FE chip from the TLAS conditions database using the Athena software framework. The parameters P_0 and P_1 are calculated using the overdrive $\Omega = \Omega\,(Q_t, Q_{it})$, the values Q_t and Q_{it} are derived from the conditions database:

$$P_0 = A_0 \cdot \Omega + B_0,\tag{7.5}$$

$$P_1 = A_1 \cdot \Omega + B_1,\tag{7.6}$$

with $\begin{aligned} A_1 &= 7.675 \times 10^7 \text{ ns}\,(e^-)^{1.5}, & B_0 &= -2.648 \times 10^{10} \text{ ns}\,(e^-)^{2.5}, \\ A_1 &= -1.597, & B_1 &= 943\ e^-. \end{aligned}$

An exemplary delay distribution is shown in Figure 7.13. This distribution was created using the simulated ToT data shown in Figure 7.12. The finely-binned delay distribution has been rebinned in bins of 25 ns width. After the new binning is applied, the shape of the delay matches the shape of a typical LVL1A distribution. Details of the rebinning process are explained in the next Section.
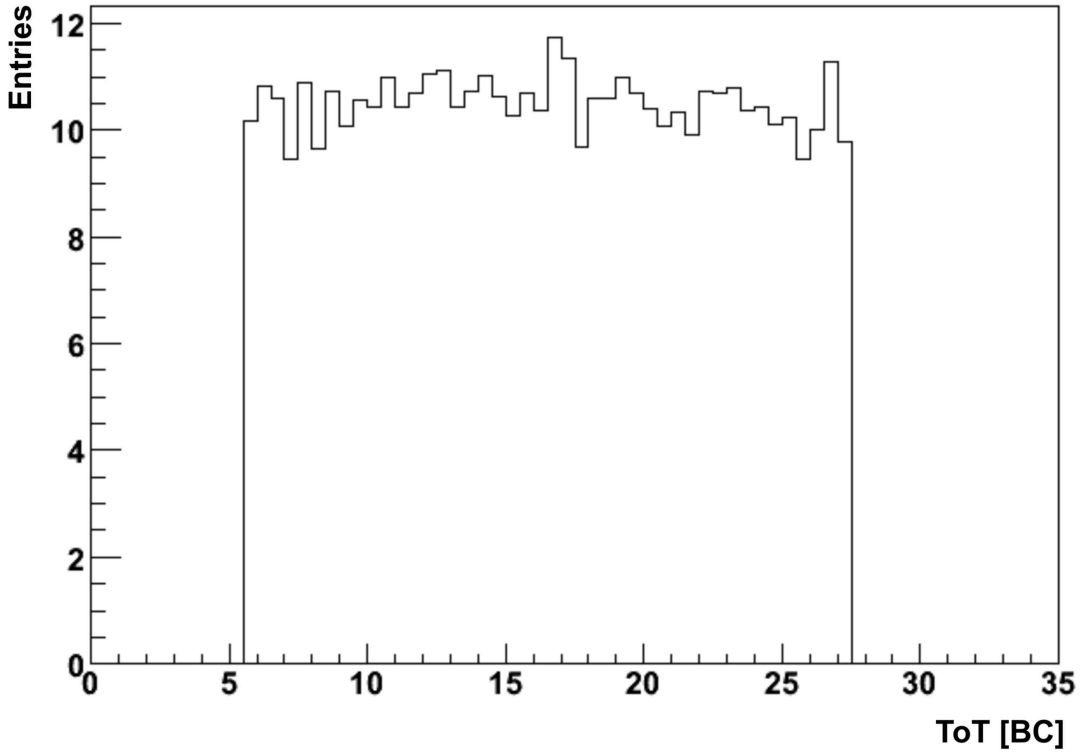
Figure 7.12: Simulated uniform ToT distribution, normalised to 572 hits in a range of ToT = $5.5 \ldots 27.5$ BC.

7.4.4 Fit of the Simulated Delay Distribution

The finely-binned simulated delay distribution is generated by taking into account only the delay originating in the timewalk effect. Hits with very large charge deposition (= large ToT value) are found in the first filled bins of the distribution shown in Figure 7.13. In order to perform the fit, the finely-binned simulated delay distribution is rebinned in bins of 25 ns width. The binning offset t_d, counted from delay value zero, defines the arrival time of the fastest hits with respect to the beginning of the readout window and is the only free parameter of the fit. The small number of entries per bin in the simulated delay distribution has no influence on the quality of the performed fit, because after the application of the new binning of 25 ns width the number of entries per bin is significantly higher. In the fit, the binning offset is shifted in steps of 0.1 ns to find the value of t_d, for which the simulated delay distribution agrees best with the measured LVL1A distribution. The paramter t_d can not be increased continuously, because the simulated delay distribution is represented by a histogram. For every step the χ^2 value is calculated using:

$$\chi^2 = \sum_{i=0}^{i=6} \frac{(\alpha_i - \beta_i)^2}{\sigma_{\beta_i}^2}, \tag{7.7}$$

with i being the index of the examined LVL1A bin, α_i the number of entries in bin i of the measured LVL1A distribution, β_i the number of entries in bin i of the rebinned, simulated delay distribution, and σ_{β_i} the statistical error of β_i. The value of $\sigma_{\beta_i}^2$ is calculated ac-
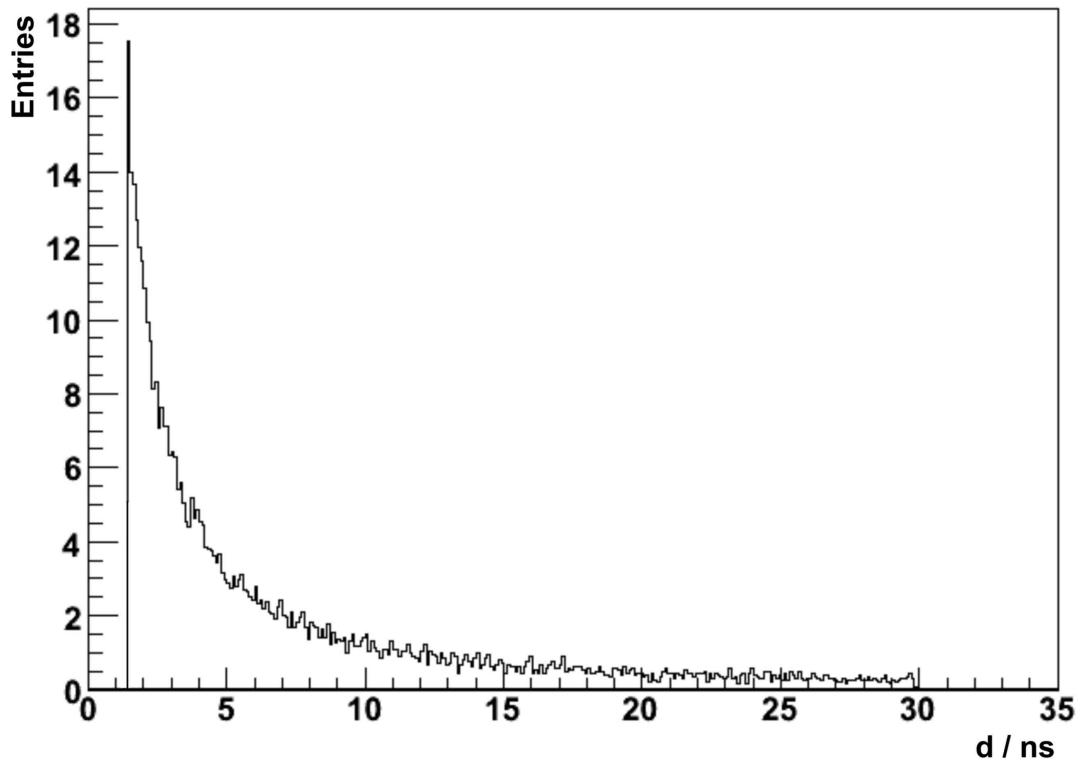
Figure 7.13: Simulated finely-binned delay distribution, converted using (7.4) from the ToT values of the distribution shown in Figure 7.12. The bin width is 0.1 ns.

cording to [TUZX07], because the available number of entries does not allow an approach assuming Poissonian errors.

The statistical error of every bin of the rebinned simulated delay distribution is calculated by:

$$\sigma^2_{\beta_i} = \left(\frac{(\beta_i + 1)(\beta_i + 2)}{(n + 2)(n + 3)} - \frac{(\beta_i + 1)^2}{(n + 2)^2} \right) n^2, \tag{7.8}$$

with n as the total number of entries in the simulated delay distribution.

Figures 7.14 and 7.15 show the measured LVL1A distributions and the fitted simulated delay distributions for FE chip number 13 of pixel module $\phi_{mod} = 1$, $\eta_{mod} = -1$ in the b-layer of the ATLAS pixel detector without timing offset and with timing offset applied. The distributions of the χ^2 values according to the performed fits in Figures 7.14 and 7.15 are shown in Figures 7.16 and 7.17. The low value of the minimal χ^2 documents the excellent agreement between the fitted and the measured distribution.
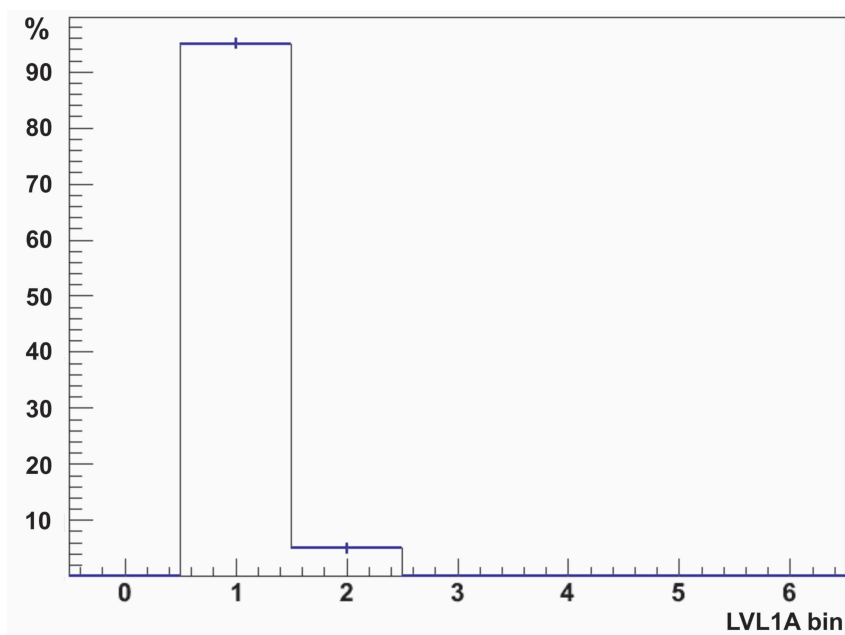
Figure 7.14: Measured LVL1A distribution (thin line) and fitted simulated delay distribution (thick line) with the vertical line being the statistical error of the bin, for a single FE chip and without timing offset for the detector without timing offset, normalised to 462 entries.
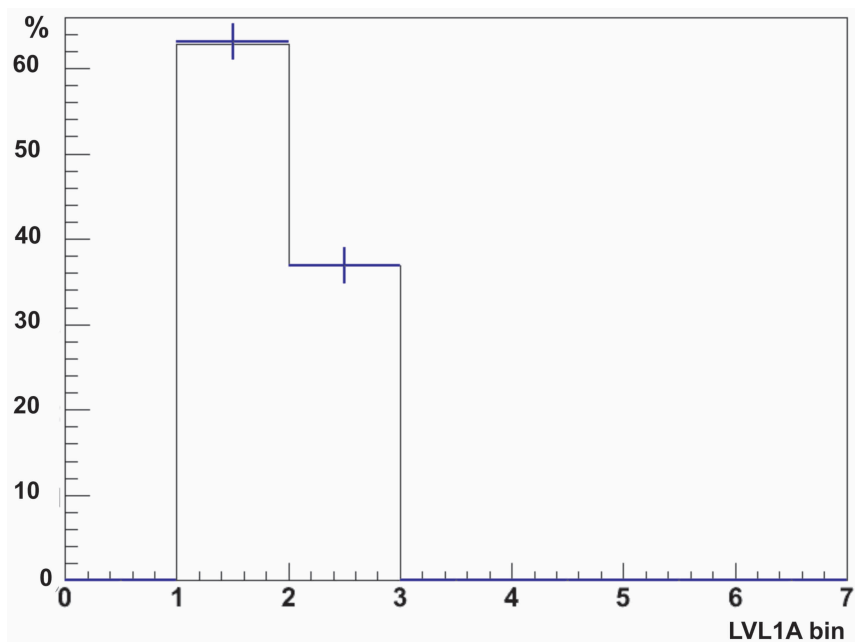
Figure 7.15: Measured LVL1A distribution (thin line) and fitted simulated delay distribution (thick line) with the vertical line being the statistical error of the bin, for a single FE chip for the detector with timing offset applied, normalised to 506 entries.
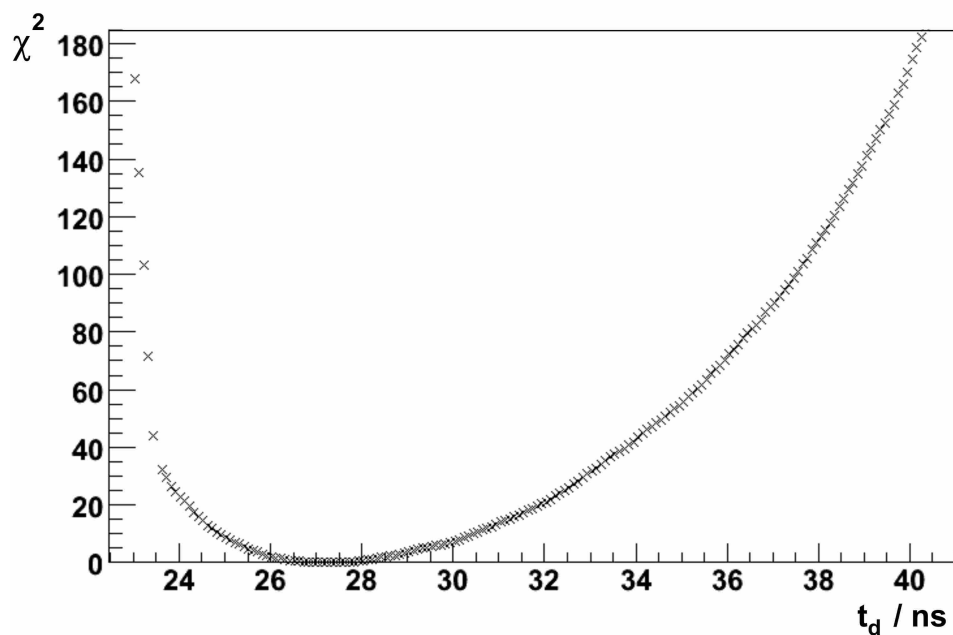
Figure 7.16: χ^2 plot for values of the binning offset t_d for the detector without timing offset. The fit according to the t_d value of minimal χ^2 is presented in Figure 7.14.
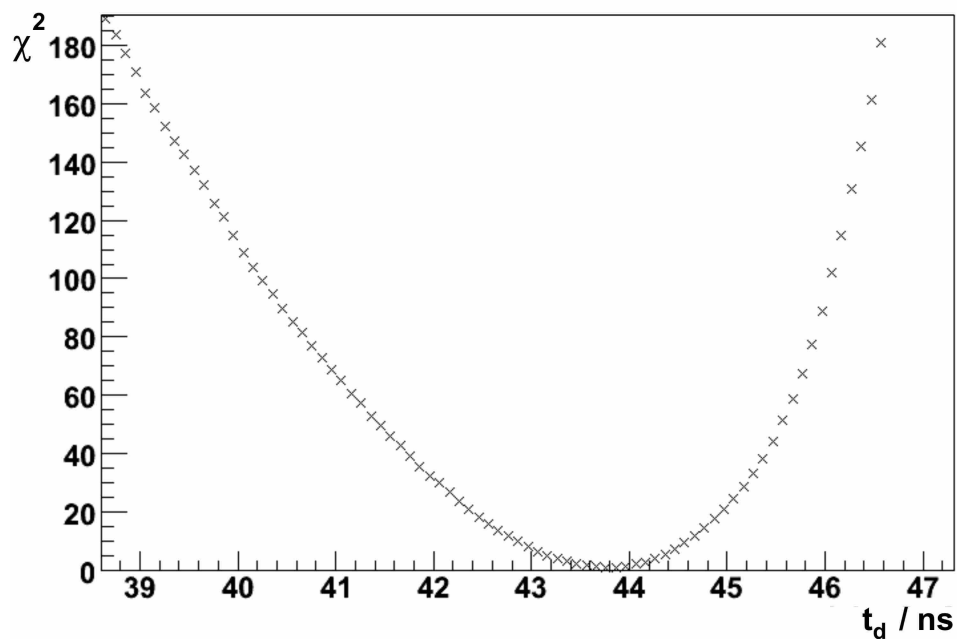
Figure 7.17: χ^2 plot for values of the binning offset t_d for the detector with timing offset applied. The fit according to the t_d value of minimal χ^2 is presented in Figure 7.15.

7.4.5 Error Analysis

The total error on t_d is composed of three components. Firstly, the error caused by the finite resolution of the fit step width σ_{res}, which is symmetrical. Secondly, the error caused by the fit quality σ_{stat}, which can be derived from the χ^2 distribution of the fits performed for each FE chip. And the third contribution, the error caused by systematic uncertainties σ_{sys}, which are due to uncertainties in the calibration parameterisations. The errors σ_{stat} and σ_{sys} are asymmetric.

The asymmetry of σ_{stat} and σ_{sys} is due to the shape of the delay distribution. The step width of the fit is 0.1 ns, because this is the resolution of the finely-binned simulated delay distribution. The number of entries n_{shift}, shifted in different 25 ns bins of the rebinned simulated delay distribution, is not constant, while the value of t_d increases constantly by 0.1 ns. The total errors $\sigma_{t_d}^{\pm}$ are given by:

$$\left(\sigma_{t_d}^{\pm}\right)^2 = \sigma_{res}^2 + \left(\sigma_{stat}^{\pm}\right)^2 + \left(\sigma_{sys}^{\pm}\right)^2 \ . \tag{7.9}$$

In general the addition of squared asymmetric errors is not correct [RB04]. The implementation of the method from [RB04] lies beyond the scope of this thesis. The expected deviations between the correct and the simplified approach are negligible as shown in [MK08].

Error due to the Resolution of the Simulated Delay Distribution

The symmetrically distributed contribution to the total error σ_{res} is caused by the finite resolution of the delay distribution. Assuming, that inside one delay bin of width Δt the true delay values are distributed according to a normal distribution, the expectation value $\overline{t_r}$ and the variance of the resolution σ_{res}^2 are calculated:

$$1 \ = \int_0^{\Delta t} c \ dt \ \Rightarrow \ c \ = \ \frac{1}{\Delta t} \ , \text{with } c = const \ , \tag{7.10}$$

$$\overline{t_r} \ = \int_0^{\Delta t} \frac{1}{\Delta t} t \ dt \ = \ \frac{\Delta t}{2} \ , \tag{7.11}$$

$$\sigma_{t_r}^2 \ = \overline{t_r^2} - \overline{t_r}^2 \ = \int_0^{\Delta t} \frac{t^2}{\Delta t} \ dt - \frac{(\Delta t)^2}{4} \ = \ \frac{(\Delta t)^2}{12} \ , \tag{7.12}$$

with a chosen resolution of $\Delta t = 0.1$ ns the error is $\sigma_{res} = \frac{0.1}{\sqrt{12}}$ ns $= 0.03$ ns.

Statistical Error of the fit

The statistical error from the fit quality is defined as the deviation of $t_d^{\pm}$ from t_d, with $t_d^{\pm}$ being the value for which the minimal value of χ^2 increases by one, i.e $\chi^2 = \chi_{min}^2 + 1$. The delay distribution has a resolution of 0.1 ns, so the values of $t_d^{\pm}$ can only be derived in steps of 0.1 ns. The selection criteria is, that the $t_d^{\pm}$ value is chosen such, that the corresponding χ^2 value is the closest upper approximation of $\chi_{min}^2 + 1$. Thus the error,
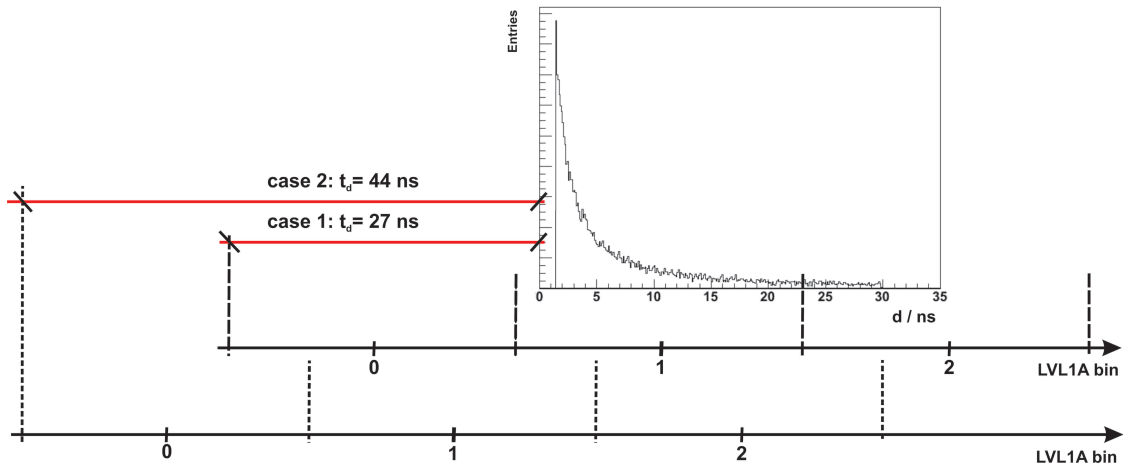
Figure 7.18: Graphical representation of the rebinning process, t_d is the binning offset.

due to the quality of the fit, is given by:

$$\sigma^-_{stat} = t_d - t^-_d \ , \tag{7.13}$$

$$\sigma^+_{stat} = t^+_d - t_d \ . \tag{7.14}$$

The asymmetry of $\sigma^\pm_{stat}$ is caused by the asymmetric shape of the χ^2 distribution for the LVL1A fit. Two cases have to be distinguished:

1. Measured LVL1A distribution whithout applied timing offset: large difference in the number of entries of LVL1A bins one and two, shown in Figure 7.14.

2. Measured LVL1A distribution with applied timing offset: smaller difference in the number of entries of LVL1A bins one and two compared to case 1, shown in Figure 7.15.

Both cases are illustrated in Figure 7.18.

In case 1 the binning offset t_d for a minimal χ^2 has to be chosen in a way, that bin zero of the rebinned simulated delay distribution is empty. Most of the entries lie in bin one and a fraction of entries in bin two. Consequently the edge of the rebinned simulated delay distribution, between bins zero and one, is located at the very edge of the finely-binned simulated delay distribution, shown in Figure 7.18. Small variations of t_d around this edge lead to strong fluctuations in the number of entries in bin zero and one of the rebinned simulated delay distribution. Therefore, the slope of the left side of the χ^2 distribution is much steeper then the slope of the right side.

In case 2 the binning offset for a minimal χ^2 has to be chosen such, that bin zero is empty. Roughly 60 % of all entries are in bin one, approximately 38 % of all entries lie in bin two and a small amount in bin three. Hence the edge between bin one and two of the rebinned simulated delay distribution is located in the middle of the finely-binned simulated delay distribution. Therefore, the fluctuations in the number of entries for bin one and two are small for variations of t_d.
But, since the edge between bin two and three of the rebinned distribution is located near

the cut-off of the finely-binned simulated delay distribution, the number of entries in bin three changes rapidly for variations of t_d. Consequently the slope of the right side of the χ^2 distribution is now steeper than the slope of the left side. Due to the wide spread of the χ^2 distribution the asymmetry of the errors is not very strong. The wide spread of the χ^2 distribution itself is caused by the small size of the data samples for each FE chip. Each selected sample contains between 400 and 700 hits (per FE Chip).

The value of the error, due to the quality of the fit is roughly $\sigma_{stat}^{\pm} = 0.8$ ns, with an asymmetry $\alpha = 0.2$ ns, for a timing offset of $t_{off} = 0$ ns. Furthermore, the value of the error for an applied timing offset of $t_{off} = 15$ ns is approximately $\sigma_{stat}^{\pm} = 0.4$ ns, with an asymmetry of $\alpha = 0.1$ ns.

Systematic Uncertainties

In order to determine the systematic uncertainties σ_{sys}, the error of the delay σ_d, which is the main input of the timing analysis, is calculated using the error propagation for:

$$d\left(ToT\right) = d\left(ToT, A, C, E, \Omega\right) = \frac{P_0\left(\Omega\right)}{\left(\frac{A\ E - ToT\ C}{ToT - A} - P_1\left(\Omega\right)\right)^{2.5}} \ , \tag{7.15}$$

with $\Omega = \Omega\left(Q_t, Q_{it}\right)$, where Q_t is the threshold and Q_{it} is the in-time threshold of the FE chip processed. Then two delay histograms are created from the simulated ToT distribution. Both are filled with delay values according to:

$$d^{\pm}\left(ToT\right) = d\left(ToT\right) \pm \sigma_d \ . \tag{7.16}$$

The first histogram is filled with values d^+ and the second with values d^-. To both histograms the LVL1A fit method is applied, as described in Section 7.4.4. The results of these fits are delay values of $t_d^{\pm\sigma_d}$. The differences between the values of t_d and $t_d^{\pm\sigma_d}$ define the upper and lower limits of the systematic error $\sigma_{sys}^{\pm}$:

$$\sigma_{sys}^+ = t_d - t_d^{+\sigma_d} \ , \tag{7.17}$$

$$\sigma_{sys}^- = t_d^{-\sigma_d} - t_d \ . \tag{7.18}$$

Figures 7.19 and 7.20 show the two varied delay distributions for d^+ and d^-, respectively.
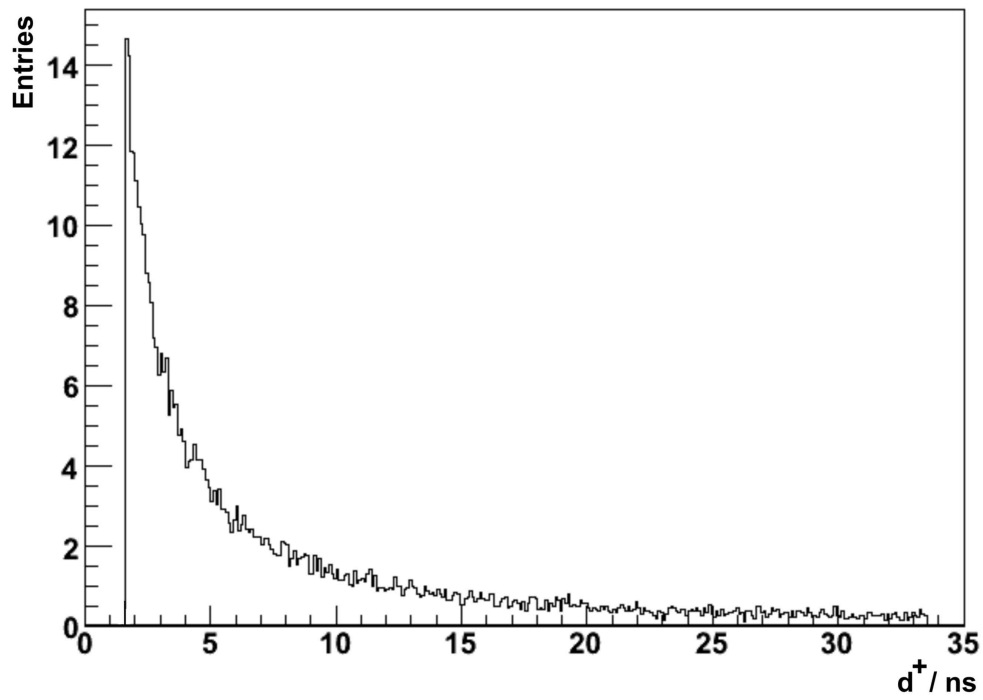
Figure 7.19: Simulated delay distribution for d^+, for FE chip 13 on module $\phi_{mod} = 1$, $\eta_{mod} = -1$ in barrel layer 0 and bin width is 1.0 ns.
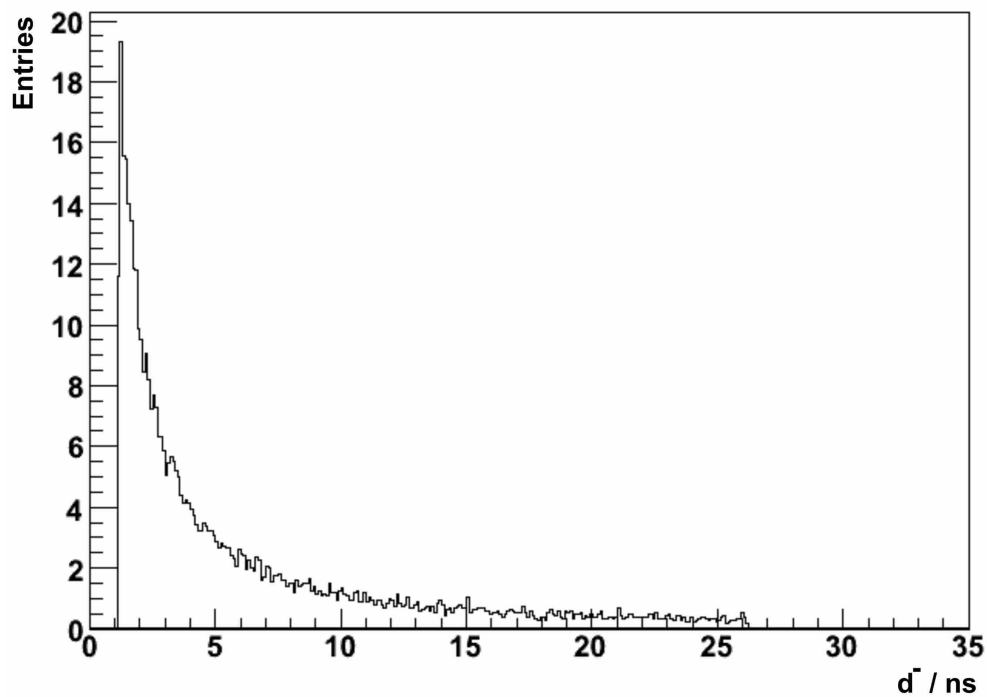
Figure 7.20: Simulated delay distribution for d^-, for FE chip 13 on module $\phi_{mod} = 1$, $\eta_{mod} = -1$ in barrel layer 0 and bin width is 1.0 ns.

The value of σ_d is calculated using the covariance matrix for the input parameters in 7.15 and the partial derivatives of $d\left(ToT, A, C, E, \Omega\right)$, according to [SB99]:

$$\sigma_d^2 = DCD^T ,\tag{7.19}$$

with D as the vector of partial derivatives and C as the covariance matrix:

$$D = \left(\frac{\partial\, d}{\partial\, ToT}, \frac{\partial\, d}{\partial\, A}, \frac{\partial\, d}{\partial\, C}, \frac{\partial\, d}{\partial\, E}, \frac{\partial\, d}{\partial\, Q_t}, \frac{\partial\, d}{\partial\, Q_{it}}, \right) ,\tag{7.20}$$

$$C = \begin{pmatrix} \sigma_{ToT}^2 & 0 & 0 & 0 & 0 & 0 \\ 0 & \sigma_A^2 & \text{cov}\,(A, C) & \text{cov}\,(A, E) & 0 & 0 \\ 0 & \text{cov}\,(C, A) & \sigma_C^2 & \text{cov}\,(C, E) & 0 & 0 \\ 0 & \text{cov}\,(E, A) & \text{cov}\,(E, C) & \sigma_E^2 & 0 & 0 \\ 0 & 0 & 0 & 0 & \sigma_{Q_t}^2 & \text{cov}\,(Q_t, Q_{it}) \\ 0 & 0 & 0 & 0 & \text{cov}\,(Q_t, Q_{it}) & \sigma_{Q_{it}}^2 \end{pmatrix} .\tag{7.21}$$

The ToT value is not correlated with any of the other parameters. Therefore, the corresponding entries in the covariance matrix are zero. The parameters of the ToT calibration $(A,\ C,\ E)$ are not correlated with the threshold and in-time threshold values (Q_t, Q_{it}), hence the corresponding entries in the covariance matrix are also zero. The value of σ_{ToT}^2 is set to zero due to the fact, that the ToT values are the result of a simulation. All errors are assumed to be distributed according to a Gaussian distribution.

The errors of the ToT calibration parameters and the errors of the threshold Q_i and in-time threshold Q_{it} are not known. The ATLAS conditions database does not hold information about the errors of these parameters. Therefore, the errors are taken as the standard deviation of the statistical mean value of the parameter distributions for each barrel layer separately.

The statistical covariance between two real-valued variables X and Y is defined by:

$$\text{cov}\,(X, Y) = E\left\{(X - E\left\{X\right\})(Y - E\left\{Y\right\})\right\}\tag{7.22}$$

with $E\left\{X\right\}$ being the expectation value of X. The standard deviations of the ToT calibration and the (in-time) threshold are calculated separately for each of the barrel layers. Despite the fact, that both RDO samples each contain more than $20\,000$ events, only a small number of hits are recorded for the end-caps. For ECC there are $370\,246$ and for ECA $352\,092$ recorded hits for the dataset without timing offset applied. This leads to approximately 160 hits per FE chip in ECC and roughly 150 hits per FE chip in ECA. The error of the LVL1A fit is, for this low statistics, too large, roughly 10 ns, to make a significant statement for the value of t_d.

The values of the errors for the separate barrel layers are shown in Table 7.1. To illustrate the correlation matrix, the correlation coefficients ρ are calculated. The values of the correlation coefficients are shown in Table 7.2.

Barrel Layer	σ_A / ToT	σ_C / e^-	σ_E / e^-	σ_{Q_t} / e^-	$\sigma_{Q_{it}}$ / e^-
b-layer	108	72 493	297	25	188
1	141	91 727	459	34	217
2	127	83 825	382	33	200

Table 7.1: Errors of the calibration parameters and (in-time) threshold calculated separately for each layer of the barrel of the ATLAS pixel detector as the standard deviation of the mean value of the parameter distributions.

Barrel Layer	$\rho(A, E)$	$\rho(A, C)$	$\rho(C, E)$	$\rho(Q_t, Q_{it})$
b-layer	0.75	0.997	0.77	0.17
1	0.88	0.998	0.89	0.11
2	0.81	0.998	0.83	0.17

Table 7.2: Correlation coefficients of the calibration parameters and (in-time) threshold calculated separately for each layer of the barrel of the ATLAS pixel detector.
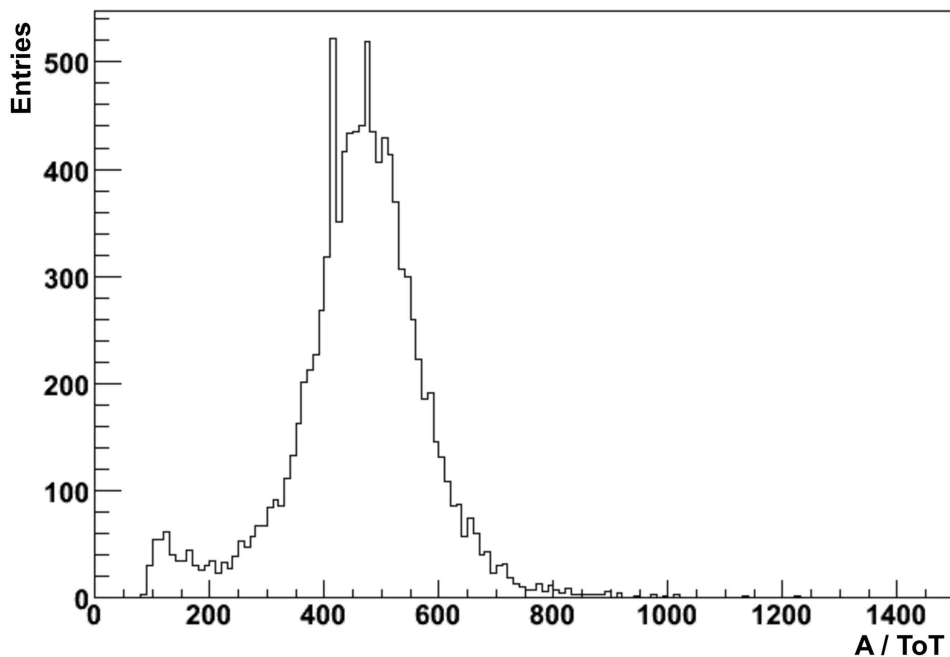
Figure 7.21: ToT calibration parameter A for barrel layer 1 of the ATLAS pixel detector. The default value is $A_d = 413$ ToT, a total of 7 904 entries are shown.

The distribution of the ToT calibration parameter A is shown in Figure 7.21. This distribution was created using the values from the ATLAS conditions database. The bin according to the value $A_d = 413$ ToT shows significantly more hits then the adjacent bins, because this value is the default value for the parameter A. During the production

measurements parameter A was set to this default value, if the fit, from which the parameter is derived, failed [AtA08].

For the other ToT calibration parameters these default values are $E_d = -1727 \ e^-$ and $C_d = 218\,481 \ e^-$. To prevent a statistical bias from these default values, the contents of these bins is manually altered before the error determination. The number of entries n_i, in bin number i containing the number of entries of the default value, was set to:

$$n_i^{man} = \frac{n_{i-1} + n_{i+1}}{2} \ . \tag{7.23}$$

The value of the systematic error $\sigma_{sys}^{\pm}$, derived from (7.17) and (7.18) is approximately $\sigma_{sys} = 1.5$ ns with an asymmetry of roughly $\alpha = 0.1$ ns for $t_{off} = 0$ ns and $\sigma_{sys} = 0.5$ ns with $\alpha = 0.1$, for $t_{off} = 15$ ns.

7.4.6 Results

In Figures 7.22 and 7.23 the calculated values of t_d are shown as a function of the FE chip number of the module on position $\eta_{mod} = -1$, $\phi_{mod} = 1$ in the b-layer of the ATLAS pixel detector. The setting of the timing offset is $t_{off} = 0$ ns in Figure 7.22 and $t_{off} = 15$ ns in Figure 7.23. All data used for the analysis, leading to the values of t_d, are derived on pixel level for normal pixels.

The asymmetries between the high and low errors of the data points are small, but visible. In general the low errors are smaller compared to the high errors. This is caused by the asymmetric shape of the χ^2 distribution, which defines the error σ_{stat}^- and the contribution of systematic error σ_{sys}^-. The contribution of $\sigma_{stat}^{\pm}$ is described in detail in Section 7.4.5. The systematic error is the dominating contribution to the total error of the data points. The contribution of σ_{sys}^- is small, because the simulated delay distribution

$$d^+ (ToT) = d(ToT) + \sigma_d \ , \tag{7.24}$$

which is used for the determination of the lower error σ_{sys}^-, has a wider spread than the distribution of the delay d. This wider spectrum causes lower values of $t_d^{+\sigma_d}$ in order to shift the same number of entries into LVL1A bin one. Therefore, the difference

$$\sigma_{sys}^- = t_d - t^{+\sigma_d} \ , \tag{7.25}$$

is smaller than the value of σ_{sys}^+. The distribution

$$d^- (ToT) = d(ToT) - \sigma_d \ , \tag{7.26}$$

has a smaller spread, which results in larger values of $t_d^{-\sigma_d}$, causing larger values of

$$\sigma_{sys}^+ = t_d^{-\sigma_d} - t_d \ . \tag{7.27}$$

For higher values of t_d, the size of the errors decreases due to the fact, that the differences between the bins one and two of the measured LVL1A distributions with applied timing offset are smaller and thus the error contributions of $\sigma_{stat}^{\pm}$ and $\sigma_{sys}^{\pm}$ are generally smaller.
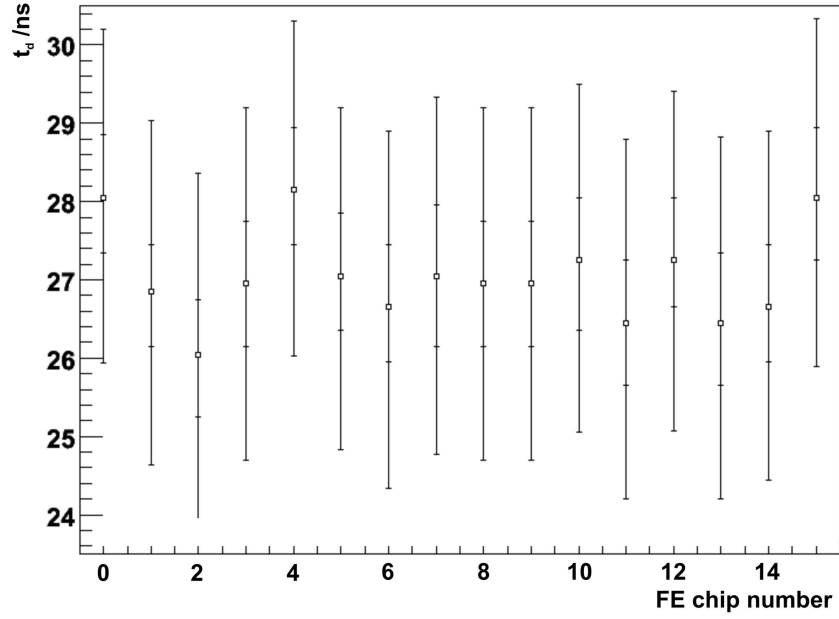
Figure 7.22: The timing t_d for the ATLAS pixel detector without timing offset for the sixteen FE chips of module $\eta_{mod} = -1$, $\phi_{mod} = 1$ and for the b-layer of the ATLAS pixel detector. The inner error bar is the statistical error, the outer error bar is the total error with quadratically summed contributions from $\sigma_{stat}^{\pm}$, $\sigma_{sys}^{\pm}$ and σ_{res}.
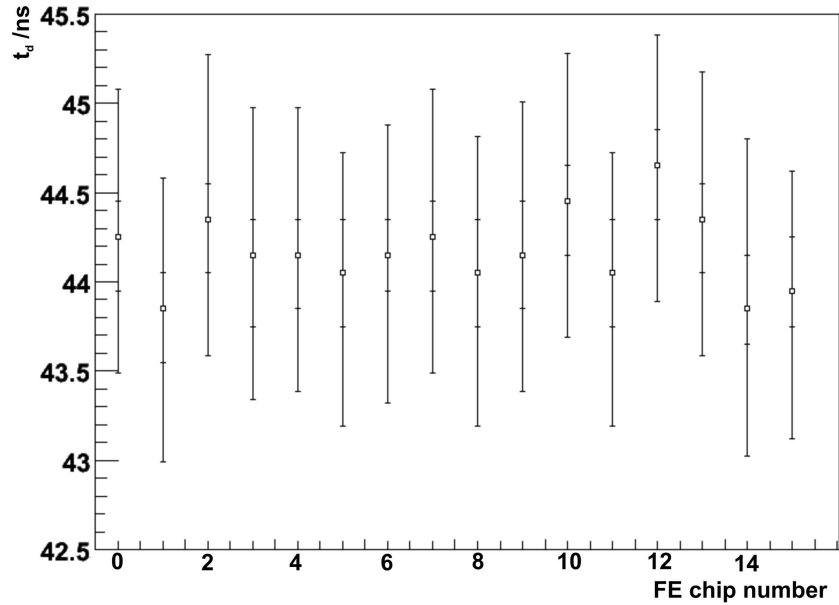
Figure 7.23: The timing t_d for the ATLAS pixel detector with applied timing offset for the sixteen FE chips of module $\eta_{mod} = -1$, $\phi_{mod} = 1$ and for the b-layer of the ATLAS pixel detector. The inner error bar is the statistical error, the outer error bar is the total error with quadratically summed contributions from $\sigma_{stat}^{\pm}$, $\sigma_{sys}^{\pm}$ and σ_{res}.

In order to determine the mean value for the timing $\overline{t_d}$ of one module, a horizontal fit was applied to the values of t_d of each single FE chip. For this horizontal fit only the statistical errors $\sigma_{stat}^{\pm}$ are taken into account, because they depend on the number of hits in the single FE chips and therefore describe the deviation of the single values around their mean. The contributions of the systematic errors and the errors due to the finite resolution of the simulated delay distribution are averaged over the FE chips, separately for the positive and negative error contributions. Tables 7.3 and 7.4 show the results of the averaged LVL1A fits of ten modules.

η_{mod}	ϕ_{mod}	n_{mod}	$\overline{t_d}$ /ns	σ_{hfit} /ns	$\overline{\sigma_{res}}$ /ns	$\overline{\sigma_{sys}}$ /ns
0	7	9834	27.33	±0.14	±0.04	+0.67 −0.67
0	6	10208	27.66	±0.13	±0.04	+0.95 −0.93
0	8	9878	26.61	±0.16	±0.04	+1.20 −1.13
-1	8	7854	27.12	±0.15	±0.04	+1.34 −1.28
-1	4	8734	27.04	±0.17	±0.04	+1.48 −1.40
-1	3	9020	26.77	±0.16	±0.04	+1.62 −1.53
-1	1	8690	26.90	±0.18	±0.04	+1.80 −1.68
-1	0	7898	27.07	±0.19	±0.04	+1.87 −1.76
-2	3	5786	27.02	±0.15	±0.04	+2.04 −1.85
-2	2	5148	27.32	±0.20	±0.04	+2.16 −1.97

Table 7.3: Results of the LVL1A fits for ten pixel modules in the b-layer of the ATLAS pixel detector without applied timing offset of $t_{off} = 0$ ns, with n_{mod} describing the number of selected hits for the corresponding module and σ_{hfit} being the statistical error of the horizontal fit.

The difference Δ between the averaged values of $\overline{t_d}$ represents the reconstructed clock phase between the modules:

$$\Delta \ = \overline{t_d}\,(t_{off} = 15 \text{ ns}) - \overline{t_d}\,(t_{off} = 0 \text{ ns}) \ , \tag{7.28}$$

For the described ten modules the differences Δ are listed in Table 7.5. The errors are added quadratically and separately for the positive and negative error contributions.

η_{mod}	ϕ_{mod}	n_{mod}	$\overline{t_d}$ /ns	σ_{hfit} /ns	$\overline{\sigma_{res}}$ /ns	$\overline{\sigma_{sys}}$ /ns
0	7	10296	44.13	±0.05	±0.04	+0.20 −0.20
0	6	9834	44.09	±0.06	±0.04	+0.29 −0.29
0	8	9746	44.12	±0.06	±0.04	+0.36 −0.37
-1	8	8734	44.12	±0.05	±0.04	+0.41 −0.42
-1	4	9394	44.13	±0.06	±0.04	+0.45 −0.46
-1	3	8932	44.21	±0.06	±0.04	+0.49 −0.50
-1	1	8404	44.14	±0.06	±0.04	+0.54 −0.55
-1	0	7502	44.15	±0.07	±0.04	+0.57 −0.58
-2	3	5588	44.08	±0.08	±0.04	+0.60 −0.62
-2	2	5764	44.08	±0.08	±0.04	+0.63 −0.65

Table 7.4: Results of the LVL1A fits for ten pixel modules in the b-layer of the ATLAS pixel detector with applied timing offset of $t_{off} = 15$ ns, with n_{mod} describing the number of selected hits for the corresponding module and σ_{hfit} being the statistical error of the horizontal fit.

η_{mod}	ϕ_{mod}	Δ /ns	σ_{hfit}^{Δ} /ns	σ_{res}^{Δ} /ns	σ_{sys}^{Δ} /ns
0	7	16.80	±0.15	±0.06	+0.70 −0.70
0	6	16.43	±0.14	±0.06	+0.99 −0.97
0	8	17.51	±0.17	±0.06	+1.25 −1.19
-1	8	17.00	±0.16	±0.06	+1.40 −1.35
-1	4	17.09	±0.18	±0.06	+1.55 −1.47

η_{mod}	ϕ_{mod}	Δ /ns	σ_{hfit}^{Δ} /ns	σ_{res}^{Δ} /ns	σ_{sys}^{Δ} /ns
-1	3	17.44	±0.17	±0.06	$+1.69$ -1.61
-1	1	17.24	±0.19	±0.06	$+1.88$ -1.77
-1	0	17.08	±0.20	±0.06	$+1.95$ -1.85
-2	3	17.06	±0.17	±0.06	$+2.13$ -1.95
-2	2	16.76	±0.22	±0.06	$+2.25$ -2.07

Table 7.5: Reconstructed clock phase Δ for ten modules of the b-layer of the ATLAS pixel detector.

As shown in Table 7.5 the reconstructed clock phase Δ agrees within the error bounds with the simulated timing offset $t_{off} = 15$ ns. The deviation δ between the reconstructed clock phase and the simulated timing offset is given by:

$$\delta_i = \Delta_i - t_{off} . \tag{7.29}$$

The values of Δ_i and the averaged error σ_{Δ_i} is shown in Table 7.6.

η_{mod}	ϕ_{mod}	Δ /ns	δ /ns	σ_{Δ} /ns
0	7	16.80	1.80	0.72
0	6	16.43	1.43	1.01
0	8	17.51	2.51	1.27
-1	8	17.00	2.00	1.41
-1	4	17.09	2.09	1.56
-1	3	17.44	2.44	1.70
-1	1	17.24	2.24	1.89
-1	0	17.08	2.08	1.97
-2	3	17.06	2.06	2.13
-2	2	16.76	1.76	2.26

Table 7.6: Clock phase Δ for ten modules of the b-layer of the ATLAS pixel detector and deviation δ, with averaged error σ_{Δ_i}. Simulated timing offset $t_{off} = 15$ ns.

As shown in Table 7.6 the deviation δ favours positive values. This can be explained with the asymmetric shape of the χ^2 distribution. The value of t_d is underestimated for values of $t_d < 35$ ns, because the left side of the χ^2 distribution is steeper than the right side. This results in smaller values of t_d. For $t_d > 35$ ns the values are overestimated, because the right side of the χ^2 distribution is now steeper than the left side. Therefore, the deviation δ of the reconstructed clock phase to the true clock phase is in general positive.

The systematic error Γ of the LVL1A fit method, for the averaged module timing is estimated using the weighted mean of the deviations δ:

$$\Gamma = \frac{\sum_i \delta_i/\sigma_{\Delta_i}^2}{\sum_i 1/\sigma_{\Delta_i}^2} \ . \tag{7.30}$$

The total error σ_Δ of the reconstructed clock phase Δ is estimated by quadratic summation of the largest error contributions, which are in this case the positive contributions of the asymmetric error, the systematic error σ_{sys}^Δ and the contributions of the statistical error of the horizontal fit σ_{hfit}^Δ and the error due to the finite resolution of the finely-binned simulated delay distribution σ_{res}^Δ.

The timing offset t_{off} used in the simulation has no error. Since the asymmetries of σ_{sys}^Δ are small an averaged symmetric error has been used. An estimator for the dispersion of the deviation is the square root of the weighted variance

$$\sigma_\Gamma^2 = \frac{\sum_i 1/\sigma_{\Delta_i}^2}{\left(\sum_i 1/\sigma_{\Delta_i}^2\right)^2 - \sum_i 1/\sigma_{\Delta_i}^4} \sum_i \frac{(\delta_i - \Gamma)^2}{\sigma_\Delta^2} \ . \tag{7.31}$$

The systematic error for the timing determination for one pixel module for the LVL1A fit method is:

$$\Gamma \ = (1.93 \ \pm 0.13) \ \text{ns} \ . \tag{7.32}$$

8 Conclusions and Outlook

The ATLAS detector is one of the largest particle physics experiments ever constructed. It is located at the Large Hadron Collider at CERN (Geneva). One of its subdetectors is the pixel detector, which provides high precision three dimensional track and vertex measurements for charged particles.

The LHC features a bunch crossing rate of 40 MHz and a design luminosity of 10^{34} cm^{-2} s^{-1}. The amount of data the ATLAS detector produces is too large to be stored without selection, hence a fast trigger system, deciding if a buffered event contains 'interesting' information, is required. The signal, which triggers the readout, is the Level 1 Accept signal. On receipt of this signal, data in a window of a length of up to sixteen LVL1A bins can be read out. Each LVL1A bin has a length of 25 ns. Due to the timewalk effect hit data from one bunch crossing are spread over several consecutive LVL1A bins (are assigned to wrong bunch crossings). In order to minimise this spread, the clocks of the separate modules of the ATLAS pixel detector have to be adjusted such, that most of all hits from a bunch crossing are assigned to one LVL1A bin. This adjustment is referred to as 'timing'.

Effects like different times of flight, cable lengths and computing times cause a phase in the module clock, which results in an extended spread of the LVL1A distribution. Hits, which generate small charges in the pixel sensors, are shifted to higher LVL1A bins and are therefore assigned to the wrong bunch crossing. Once the LHC is fully operational, only one LVL1A bin is read out and the spread of the LVL1A distribution has to be minimised. The clock phase between the modules of the pixel detector can be reconstructed by determination of the time t_d between the beginning of the readout window and the arrival time of hits with large energy deposition in the detector.

This thesis investigated the determination of t_d for the modules of the ATLAS pixel detector from event data, which will be available, once the LHC is fully operational. The studies were carried out on simulated data and simulation was performed using the Athena software framework, which is the common software framework for the ATLAS experiment. Two sets of simulated event data were produced. For the simulation of the second dataset a known clock phase of $t_{off} = 15$ ns was applied. This phase was reconstructed by comparison of the t_d values of two modules from both datasets. The method used for the determination of t_d was the LVL1A fit method. The LVL1A fit method utilises the fit of a finely-binned delay distribution (bin width < 1 ns) to the coarsely binned LVL1A distribution (bin width 25 ns) to determine t_d. The analysis was performed on single FE chips and these results for t_d were averaged to obtain a mean value for each pixel module.

The data extraction and the analysis are technically separated. The extraction of the necessary data was performed using a dedicated algorithm, which was embedded in the event reconstruction of the Athena software framework. The analysis of the data was performed using a stand alone C++ application, which relies on ROOT libraries. The C++ application is based on a macro used in [MK08].

The systematic error Γ for the determination of the clock phase between two modules of the ATLAS pixel detector using the LVL1A fit method was found to be:

$$\Gamma_{\text{simulation}} = (1.93 \pm 0.13) \text{ ns} , \tag{8.1}$$

for simulated input data. Measurements on a hardware test setup at CERN, which are described in [MK08] estimate the systematic error of the LVL1A fit method to

$$\Gamma_{\text{hardware}} = (1.5 \pm 0.8) \text{ ns [MK08]}, \tag{8.2}$$

which is, within the error bounds, comparable to the result of this thesis.

The averaged clock phase $\overline{\Delta}$ between the two simulated datasets was determined to:

$$\overline{\Delta} = (16.97 \pm 1.19) \text{ ns} , \tag{8.3}$$

which agrees with the simulated clock phase of $t_{off} = 15$ ns.

The studies performed in this thesis showed, that the investigated LVL1A fit method can be used to determine the clock phase between two modules of the ATLAS pixel detector with a precision of approximately 2 ns.

Outlook

The LVL1A fit method can only be applied, if the readout window comprises more then one consecutive LVL1A bin. Since the readout window will only contain one LVL1A bin once the LHC operates at maximum luminosity, it will not be possible to determine clock phases during this phase by using the LVL1A fit method. At the first runs during the time of comissioning, the LHC will not feature full luminosity and the maximum bunch crossing rate. It is possible to extend the length of the readout window for these runs. Thus the clock phases of the ATLAS pixel modules may be determined using the data produced during these first calibration runs [AtA08].
Another possibility is to use data from cosmic particles, which cross the ATLAS detector. Data taking for cosmic particles started in September 2008 and will continue until the LHC is ready for the first beam collisions. An additional challenge of the use of data from cosmic particles is, that it is not known, when within the LVL1A bin of 25 ns the particle crossed the detector. Therefore, a trigger jitter of 25 ns has to be applied to the finely-binned simulated delay distribution. The trigger jitter may be reduced by utilising the time measurements of other subdetectors like the TRT. Additional challenges are the low hit occupancy and the low efficiency of the track finding algorithms for small incidence angles of particles. Especially for modules located on the sides of the barrel and in the end-cap it will not be possible to determine the delays, because the hit occupancy will be too low. Dedicated runs of the LHC with larger readout windows are necessary (and foreseen) to determine the timing of the ATLAS pixel detector.

Bibliography

[AL04] ALICE Collaboration, *ALICE: Physics Performance Report*, Volume I, J. Phys. G: Nucl. Part. Phys. 30 (2004) 15171763.

[ALXR] Web Tool for Athena Code referencing, *LXR Cross Referencer*, http://alxr.usatlas.bnl.gov/, for Athena Version 14.2.X, January 2009.

[AR04] A. Rimoldi et al., *The Simulation of the ATLAS Experiment: Present Status and Outlook, ATLAS Internal Note*, ATL-SOFT-2004-004, 2004 and references therein.

[AS07] A. Salzburger et al., *Concepts, Design and Implementation of the ATLAS New Tracking (NEWT)*, ATL-SOFT-PUB-2007-007 , December 2007 and the reference therein.

[AtA08] A. Andreazza, Instituto Nazionale di Fizica Nucleare Milano, private communication.

[ATLC05] ATLAS Computing Group, *ATLAS Computing Technical Design Report*, ATLAS TDR-017, CERN/LHCC 2005-022, June 2005.

[ATL92] ATLAS Collaboration, *ATLAS Letter of Intent for a General Purpose pp Experiment at the Large Hadron Collider at CERN*, CERN/LHCC/92-4, 1992.

[ATL99a] ATLAS Collaboration, *ATLAS Detector and Physics Performance Technical Design Report Vol.I*, CERN/LHCC 99-14, May 1999.

[ATL99b] ATLAS Collaboration, *ATLAS Detector and Physics Performance Technical Design Report Vol.II*, CERN/LHCC 99-15, May 1999.

[ATLEl08] ATLAS Collaboration, *ATLAS pixel detector electronics and sensors*, JINST 3 P07007, July 2008.

[ATLj08] ATLAS Collaboration, *The ATLAS Experiment at the CERN Large Hadron Collider*, JINST 3 S08003 ,August 2008.

[ATLMu07] ATLAS Muon Collaboration, *ATLAS Muon Spectrometer Technical Design Report*, CERN/LHCC 9722, June 1997.

[ATLPix98] ATLAS Collaboratation, *ATLAS Pixel Detector Technical Design Report*, ATLAS TDR 11, CERN/LHCC 98-13, May 1998.

[ATLTrig98] ATLAS Level 1 Trigger Group, *ATLAS Level 1 Trigger Technical Design Report*, ATLAS TDR 12, August 1998.

[EA03] E. Abat et al., *The ATLAS Transition Radiation Tracker (TRT) proportional drift tube: design and performance*, JINST 3 P02013, 2003.

[EB03] E. Barberio, *Studies and optimisation of the transition radiation performance for the ATLAS TRT with an improved detector simulation*, ATL-INDET-2003-013, July 2003.

[RB02] R. Beccherle et al., *MCC: The Module Controller Chip for the ATLAS PixelDetector*, Nucl. Instrum. Methods Phys. Res., A 492 (2002), 117133.

[CA08] C. Amsler et al.,*Review of Particle Physics*; Physics Letters B667, 1 (2008).

[CC08] C. Collard (ed.), *Searches for the Higgs Boson and Extra Dimensions at the LHC*, Proceedings of the first AFI workshop in Innsbruck, ATL-PHYS-CONF-2008-006, Geneva, Jan 2008.

[CG93] e.g. C. Grupen, *Teilchendetektoren*, BI-Wissenschaftsverlag, Mannheim, 1993, and references therein.

[CMS06] The CMS Collaboration, *CMS Technical Design Report*, CERN/LHCC/2006-001 February 2006.

[DD07] D. Dobos, *Commissioning Perspectives for the ATLAS Pixel Detector* (Ph.D. Thesis), CERN-THESIS-2008-022, October 2007.

[Dj05] A. Djouadi, *The Anatomy of ElectroWeak Symmetry Breaking, Tome I: The Higgs boson in the Standard Model*, arXiv:hep-ph/0503172v2, May 2005.

[ERW98] E. Richter-Was et al., *ATLFAST 2.0 a fast simulation package for ATLAS*, ATL-PHYS-98-131, November 1998.

[FH01] F. Hügging, *Der ATLAS Pixelsensor, der state-of-the-art Pixelsensor für teilchenphysikalische Anwendungen mit extrem hohen Strahlungsfeldern (Ph.D. thesis)*, CERN-THESIS-2001-027, June 2001

[FL07] F. de Lorenzi, *Timing Characteristics of the ATLAS Pixel Detector* (Master Thesis), Universita Degli Studi di Milano, 2007.

[GA07] G. Arduini et al., *Alternative Bunch Filling Schemes for the LHC*, CERN LHC Project note 401, March 2007.

[Gr93] C. Grupen, *Teilchendetektoren*, BI-Wissenschaftsverlag, Mannheim, 1993.

[H66] P.W. Higgs, *Spontaneous Symmetry Breakdown without Massless Bosons*, Phys Rev. 145 (1966) 1156.

[JJ05] J.N. Jackson and the ATLAS SCT Collaboration, *The ATLAS semiconductor tracker (SCT)*, Nucl. Instrum. Methods Phys. Res. A 541 (2005) 8995.

[JW08] J. Wotschack, *ATLAS Muon Chamber Construction Parameters for CSC, MDT and RPC Chambers*, ATL-MUON-PUB-2008-006, April 2008.

[KG08] K. Grybel, private communication, December 2008.

[LEP08] CERN Archive CERN-ARCH-LEP-01-001 to 06-017, also: http://library.cern.ch/archives/isad/isalep.html (25th of October 2008).

[LHC04] LHC Collaboration, *LHC Design Report, v 3; The LHC injector chain*; CERN 2004-003-v3, 2004.

[LHC08] http://ab-div.web.cern.ch/ab-div/Publications/LHC-DesignReport.html, (13th of June 2008).

[LHCb03] LHCb Collaboration, *LHCb Technical Design Report*, CERN/LHCC 2003-030, September 2003.

[LHCf06] LHCf Collaboration, *LHCf Technical Design Report*, CERN-LHCC-2006-004, LHCF-TDR-001, February 2006.

[LXR01] `PixelDigitization.cxx`; *http://alxr.usatlas.bnl.gov/ lxr-stb3/ source/atlas/InnerDetector/InDetDigitization/PixelDigitization/ src/PixelDigitization.cxx*, Athena version 14.2.20, (11th of February 2009).

[LXR02] `PixelTimewalkGenerator.cxx`; *http://alxr.usatlas.bnl.gov/ lxr-stb3/source/atlas/InnerDetector/InDetDigitization/PixelDigitization/ src/PixelTimeWalkGenerator.cxx*, Athena version 14.2.20, (11th of February 2009).

[MK08] M. Köhler, *Studies of the Timing Behaviour of the ATLAS Pixel Detector*(Master Thesis), University of Siegen, August 2008.

[Mo99] M. Moll, *Radiation Damage in Silicon Particle Detectors* (Ph.D. Thesis), University of Hamburg, 1999.

[MP08] M. Pontz, *Studies of the ATLAS Pixel Detecor Module Timing with the Athena Framework* (Master Thesis), University of Siegen, August 2008.

[MS05] M. Smizanska University of Lancaster, *PythiaB interface to Pythia6 dedicated to simulation of beauty events*, March 2005, and references therein.

[Per90] e.g. Donald H. Perkins, *Hochenergiephysik*, Addison-Wesley Publishing Company Inc 1990, and the references therein.

[RB04] R. Barlow, *Asymmetric Errors*, arXiv:physics/0401042v1, January 2004.

[SB99] e.g. S. Brandt, *Data Analysis: Statistical and Computational Methods for Scientists and Engineers*, third ed., Springer, New York 1999.

[TF06]   T. Flick, *Studies on the Optical Readout for the ATLAS Pixel Detector. Systematical Studies on the Functions of the Back of Crate Card and the Timing of the Pixel Detector* (Ph.D. thesis), University of Wuppertal, 2006.

[TOT07]   The TOTEM Collaboration, *TOTEM Technical Design Report*, CERN-LHCC-2004-002, TOTEM-TDR-001, January 2007.

[TUZX07] T. Ullrich and Z. Xu, *Treatment of Errors in Efficiency Calculations*, arXiv:physics/0701199v1, January 2007.

[WY06]   W.-M. Yao et al, *Review of Particle Physics*, Journal of Physics G33, 2006.

List of Figures

Index

Acknowledgments

The work is done and its time to thank you, who contributed to this thesis. As always there is not enough space (and memory) left to thank all of you in the appropriate way, so let me apologise if I forgot someone in this place. My undying gratitude goes out to:

Prof. I. Fleck for his willingness to read this thesis as a co-reviewer and for future challenges.

Attilio Andreazza for his continuing support and answers to all my questions related to the Athena software framework.

My superviser Prof. P. Buchholz for his support, advice and the opportunity for an extended stay at CERN.

Iskander Ibragimov for his support during my time at CERN.

Michael Köhler and Michael Pontz, who are the true timing experts.

Kai Grybel, for giving me a quick start in Athena.

Wolfgang Walkowiak and Thorsten Stahl for proofreading of the most important parts of this thesis.

Uwe Fröhlich and Marcus Rammes for their friendship, their professional, personal advice and comments from the bright side of life.

Thomas Bäcker for not complaining about my 'laments'.

My mom and dad for their support in nutrition and all the other good things parents do.

My brilliant sister Eva for being so brilliant and linguistic advice.

My brother Andre for having all the fun that I don't have and intruducing me to the common term 'SNAFU'.

My band colleagues from *DaemOnizeR* and *Virtual-Xperience*, for not asking anything about physics.

Diesen Abschnitt muss ich jetzt in Deutsch schreiben, denn er ist jemand besonderem gewidmet. Einfach zu sagen 'danke' reicht eigentlich nicht aus. Danke Christin für deine Liebe und dein Verständnis.

At this point, the last point actually, I have to thank myself for doing a great job and for being such a nice guy, thank you Hendrik Czirr!

Acknowledgments

Eidesstattliche Erklärung

Hiermit erkläre ich, dass ich die vorliegende Masterarbeit selbstständig verfasst und keine anderen als die angegebenen Quellen und Hilfsmittel benutzt, sowie Zitate und Ergebnisse Anderer kenntlich gemacht habe.

Siegen, den 18.03.09

Hendrik Czirr